MASTER

Creating an array of ultracold Sr-88 atoms for quantum computing via light-assisted collisions

Kappé, Jur

Award date:
2022

TU/e EINDHOVEN UNIVERSITY OF TECHNOLOGY

Department of Applied Physics
Coherence and Quantum Technology Group

Creating an array of ultracold Sr-88 atoms for quantum computing via light-assisted collisions

Master Thesis (45 ETC)

Jur Kappé 1252895

Supervisors:
S. Kokkelmans dr.ir.
M. Mohan MSc.
I. Knottnerus MSc.

Committee Members:
S. Kokkelmans dr.ir.
E. Vredenbregt dr.ir.
H. Huinink dr.ir.

Eindhoven, September 2022

Abstract

Quantum computing and neutral atom cooling have made enormous progress over the last decades. At the Eindhoven University of Technology, the approach to realise a quantum computer with neutral atoms is by using an array of Far-Off Resonance Traps (FORTs). These traps, to which we refer to as an optical tweezer array, will ultimately be loaded with single strontium-88 atoms. To prepare a single atom in a tweezer trap, one illuminates the tweezer trap with laser light that we refer to as the collision laser, to induce light-assisted collisions. The goal is to make the preparation efficiency per tweezer trap as high as possible by enhancing the one-atom loss over the two-atom loss mechanism.

To investigate this theoretically, our study followed two different approaches. The first one is a semi-classical simulation, referred to as "simulation in this thesis". The second one a quantum approach that involves wave function overlap calculations between the particles in the ground state and in the excited state, here referred to as "overlap calculations". For the simulation, the particles are assumed to have a definite position, while moving inside the tweezer trap. When the particles come close to each other, the interaction energy increases, resulting in the blue-detuned collision laser to become resonant with the ground-excited state transition of the strontium-88 atoms. This transition can lead to energy gain as a result of motion in the repulsive excited interaction potential, on the detuning and the Rabi frequency of the collision laser.
For the overlap calculations, the physics of the particles is captured by the relative wave functions of two interacting atoms in the ground and excited state, from which one can obtain the overlap between states in a two-level system within the strontium-88 atom. By calculating the wave function overlap as function of the detuning, the transition rate between the two levels can be calculated as function of the ground-state energy and the detuning. Finally, the two approaches are combined to calculate the trap loss at a temperature of $1\,\mu K$, using a trap loss profile from the simulation and a hypothesized trap loss profile. Using these trap loss profiles, we are able to calculate the trap loss as function of the detuning and to determine the optimum detuning for trap loss.

For Rabi frequencies between $\Omega = 0.25\,\mathrm{MHz}$ and $\Omega = 5\,\mathrm{MHz}$, and for a detuning between $\Delta = 1.76\,\mathrm{MHz}$ and $\Delta = 2.5\,\mathrm{MHz}$, using a trap depth of $120\,\mu K$ with strontium-88 atoms, the optimal regime is found where the particles approach each other in the ground state and gain just enough energy to exploit the differences in energy prior to the collision, which causes the desired one atom trap loss for the maximum trap preparation efficiency. This preparation efficiency is not explicitly calculated due to a lack of accurate information of one-body losses over two-body losses.

Preface

After discussing back and forth for a suitable project, Servaas Kokkelmans and I ultimately came to a conclusion that a combination between an experimental and theoretical subject would be best suited.

This could then be done in cooperation with Ivo Knottnerus, an experimentalist from Amsterdam working on a quantum computer using strontium-88 atoms. A quantum computer using strontium atoms was never built before and it was therefore quite an adventurous project to help with. After a small introduction it became clear that optical tweezer loading wasn't as optimal for strontium as it has been shown to be for rubidium atoms.

To solve this problem, a theoretical background was needed to support the physical processes and to optimize the laser properties and scattering events. This could be done via the help of Madhav Mohan, a theoretical physicist specialized in quantum computing atom manipulation.

These two PhD students, together with the help of Denise Ahmed-Braun, Jasper van der Kraats, Robert de Keijzer, Jasper Postema and Bas van Kampen, it was made possible to learn a lot on quantum computing and the scattering problems related in order to experimentally prepare the qubits in the tweezer traps.

I wanted to give big thanks to the team and the individuals for helping me through difficult problems and tasks, even with the - looking back - easier questions, nobody ever symbolically rolled their eyes rather they were always actively trying to participate into the questions. This is so important for the moral throughout the year and I can not point that out enough. I hope I will see you back in later research to work together and maybe, answer your questions accordingly.

To finish off I also want to thank my parents, who supported me in every way and listened to my metaphoric snooker ball story when talking about these so called atoms. How strange it may seem, as the famous Richard Feynman pointed out

"If you want to master something, teach it." - Richard Feynman

and it really helped, a big thanks to everybody!

Contents

Chapter 1

Introduction

The fundamental basis of quantum computing is built around the fact that information should be physical as Landauer pointed out and should, as a consequence, be stored on a physical system[1]. For us physicists this sounds promising, since manipulating systems is what we have been doing since the beginning of humanity. Over the years, this information has become more and more abstract, until we reached the point of the information being zeros and ones; a binary system. This system can well be manipulated with the well-known classical Turing computer[2]. However, when Richard Feynman in 1982 proposed the idea of a quantum computer, a new information processing era was introduced[3]. This new computer made information processing interesting due to the quantum parallel processing possibilities. This is possible, since a quantum computer makes use of qubits, a quantum two-level system which evolves according to the Schrödinger equation. This multiple quantum state manipulation is possible due to a quantum principle called quantum superposition, which implies that the general quantum state can be constructed as a linear combination of basis states. Together with quantum entanglement, which correlates the phases of different qubits and makes cooperation between qubits possible, this forms the basis of the quantum computer. Computations with different complexity classes could be done as David Deutsch pointed out in 1985. After Peter Shor discovered a famous quantum algorithms in 1994[3], able to factorize large numbers, the interest in quantum computing exploded.

During the same time, people tried to cool down atoms to minuscule temperatures to get better insights of atom properties. In 1975 Hänsch and Schawlow showed, after the invention of narrow linewidth tunable lasers, that light sources could exert a substantial force on atoms, causing them to slow down, making it useful for cooling[4]. A decade later, in 1986, when the Magneto Optical Trap (MOT) was introduced, it became possible to confine atoms to a small region of space using a spatially dependent magnetic field, and to ultimately create an optical molasses. The first experiments were done on Na, since it had the most ideal level structure, but it was only a matter of time when before tunable laser sources, such as the laser diodes and the Ti:sapphire laser, became available, so that other - heavier - neutral atoms, such as strontium-88, could be cooled down to temperatures below the Doppler temperature, typically in the order of micro-kelvin[5].

One way to combine the theoretical advances in the field of quantum information with the advances in experimental atomic physics is through the field of neutral atom quantum computing, that has garnered significant research interest[4]. This neutral atom manipulation is important for high-fidelity quantum computing as it is well isolated from the environment and can be prepared in relatively large systems of hundreds or thousands of particles with different geometries[6], which can ultimately bring light to the fields of cryptography, search problems, simulation of quantum systems, machine learning and many other BQP ("bounded error, quantum, polynomial time") problems[7].

A bottom-up approach to trap atoms, such as atom-by-atom assembly where single atoms are

trapped and individually positioned in desired geometries, can be achieved using optical tweezers[6]. The individual traps are made of dipole traps produced by a digital micromirror device (DMD) or spatial light modulator (SLM) and the qubits can be manipulated by optical fields controlled by acoustic-optical modulators (AOMs) and two-dimentional acousto-optical deflectors (AODs)[7]. Optical tweezers have made remarkable process in the last few years as more than 100 sites can be deterministic filled with single atoms[8][9][10]. This deterministic filling is done in two stages, in the first stage either 0 or 1 atoms are left in each trap caused by light-induced collisions, this can reach efficiencies up to 50% for strontium-88[11]. Then these atoms can be reassembled to create a full tweezer array of single strontium-88 atoms. These single atoms can function as Rydberg qubits with high-fidelity state resolved readout, high-fidelity entangling operations and strong interactions and entanglement between the qubits[10]. However, to reach this stage of computation, new sophisticated methods for single atom preparation have to be developed to increase the atom preparation per tweezer site prior to the reassembling, which will be the topic of this thesis.

The single atom preparation in this thesis will be done for strontium-88. To increase the single atom preparation efficiency we will research the two-body scattering processes caused by a collision laser, this collision laser is detuned relative to a transition in the strontium-88 atoms causing energy to be released per collision. As will be explained in the next section, the highest preparation efficiency can be obtained by maximizing the ratio of one-body losses over two-body losses. This way, the most single strontium-88 atoms will be left on average per dipole trap in the tweezer array.

To investigate this in this thesis, the one-body losses will first be investigated using a semiclassical simulation, where the particles have a definite position in phase space located in a tweezer trap. This tweezer trap is a dipole trap, from which multiple form a tweezer array. In the tweezer array the strontium atoms can be trapped and cooled down. Also, a collision laser can be used over this trap to induce two-body collisions between the atoms. Using matlab code, the collision processes have been simulated within a single dipole trap to investigate the one- over two-body losses.
After the simulation research, the focus of this thesis will shift towards a quantum approach in which the particles behave as waves. In this approach, the overlap wave function between the ground and excited state, together with different trap loss profiles, will determine the rate of loss for different detunings. The trap loss profiles are defined as the energy increase due to collision processes as a function of the detuning of the collision laser. One of the trap loss profile will be taken from the simulation, but also a constant trap loss profile and a hypothesized trap loss profile will be used to investigate how it affects the total strontium atom trap loss.

1.1 One-body loss vs. two-body loss

In order to do proper quantum information processing, it is important to have a collection of qubits that can interact with each other but still have long coherence times. This can be achieved using single trapped neutral atoms at extreme cold temperatures, which allows the atoms to have minimal perturbation with its environment due to little interaction. To prepare a single atom, a Far Off Resonance Trap (FORT) can be used, as they provide conservative potentials for the atoms and they can be dynamically reconfigured while still having long coherence times, as will be explained in section 3.2.2. For rubidium atoms, single atom preparations have reached a 91% loading efficiency using light-assisted collisions[12]. Light-assisted collisions take place if two colliding atoms come near each other in the presence of light that is near-resonant to an atomic transition - this process importantly leads to an increase in the energy of the atoms as the atoms, once excited, can move in the dipole interaction potential and gaining some energy before decaying back to the ground state. One of three possible outcomes will happen in a light assisted collision, as the energy release between the atoms is either: (1) enough for both atoms to escape, (2) only enough for one atom to escape or (3) it is not enough for either of the atoms to escape. These processes can be seen in figure 1.1 given by a), b) and c) respectively. Path a) is called a two-body loss whereas path b) is called a one-body loss. Path c) causes no loss and the same amount of atoms are still left in the trap. [12]
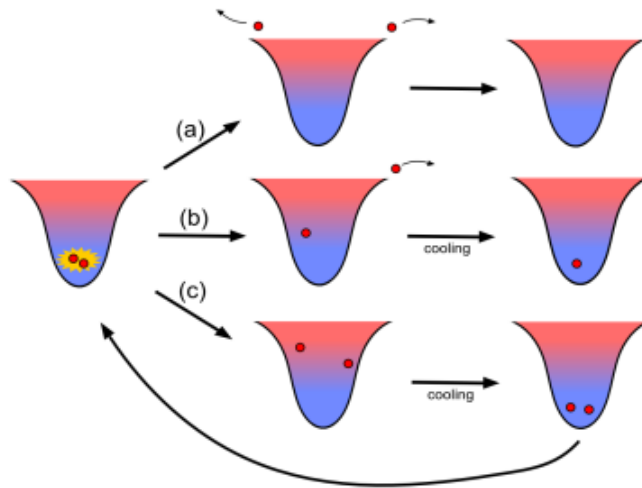
Figure 1.1: The three processes which happen for light-assisted collisions due to an increase in energy. From top to bottom: (a) two-body losses, (b) one-body loss and (c) no loss. From left to right the atoms collide which causes any of the three possible losses before cooling back. Image taken from [12].

The final goal of these light assisted collisions is to kick out atoms of the tweezer trap such that eventually one atom, no more and no less, is left in the trap, starting from an atom number of $\sim 7 - 10$. Naively one can say two-body losses are the most efficient since this would reduce the atom number the quickest and could potentially reach one atom in the trap if the initial atom number inside the trap was an uneven number. However, if the atom preparation started out with an even number of atoms, two-body losses would not do the job, since this leaves the trap with zero atoms. Taking the even and uneven cases equally would ultimately result in an atom preparation efficiency of 50%. To increase atom preparation up to 100%, one should preferably consider only one-body losses, since in this case the trap will definitely be left with only one atom. Once one atom is still in the trap, there is no possibility for the atom to leave the trap on its own, since mostly two-body collisions can effectively induce energy into the system.

Now, when opting for a high loading efficiency, it seems quite obvious that the collisions should result in as many one-body losses as possible. This process can be optimized by tuning laser parameters such as the detuning and the intensity and should be varied in such a way that they optimize the scattering properties of the strontium-88 atoms. A low detuning could mean many excitations but a relatively low energy increase per excitation, whereas a high detuning could mean the few excitations but a high increase per excitation. A low Rabi frequency could also mean too little excitation and a Rabi frequency too high might also be far from optimal. Therefore we will research these properties carefully in the thesis.

If one is able to optimize the one-body losses over two-body losses, many of the tweezer traps are filled and less rearranging is needed afterwards[13]. After the tweezer array is loaded with as many one particle traps as possible one can use fluorescent imaging to record the initial positions of all loaded traps. Then, using an analysis of the image with a cost algorithm[14], a trapping beam can be used which reassembles the atoms to an image fidelity up to 99.3%[13]. However, this rearranging cost some time and having a higher preparation efficiency before the rearranging is therefore highly desirable.

1.2   Thesis outline

In this thesis, a systematic discussion of the problem will be presented in three main parts: The theory in part 1, the description of the simulation in part 2, and ultimately the results in part 3. This will be finished off with a conclusion and discussion.

The theory
For the theory, first the basic principles will be explained regarding light-assisted collisions in section 2.1. This will be done within a semiclassical framework where the particles will be seen as hard sphere atoms with a definite position. Also, no uncertainties are taken into account to make the picture as clear as possible. Then this picture will be applied to rubidium in section 2.2, a proven strategy which shows why light-assisted collisions should work.
Next, a more complete picture of the light-assisted collisions will be explained in section 2.3, in which the quantum nature is taken into account by considering the wave functions of our system. This approach will lead to an wave function overlap between the ground and excited state and consequently to the trap loss formula as a function of the wave function overlap.
Once the two pictures are explained, it is useful to talk about how this wave function overlap can be calculated. Specifically, how the wave functions of the strontium-88 atoms can be calculated considering the short- and long-range of the interaction potential. The short-range ground state wave function will be explained in section 2.4.2 and the excited state wave function in section 2.4.3. The long-range wave function will be explained in section 2.4.4.
After the wavelike nature of the quantum wave function, the focus is shifted to the internal quantum state dynamics caused by the interaction with the laser light. This leads to theory about Rabi oscillations and their off-resonance solutions, optical Bloch equations to include spontaneous emission and their solution and finally the polarizability of the different states, all in section 2.5. The theory part will be finished by explaining the master equation of the trap loss mechanism in section 2.6.
Then the experimental constraints will shortly be explained, starting off with the properties of strontium-88 in section 3.1, followed by the temperature limits in section 3.2.1, since these limits will be important to understand the heating in the simulations. Finally, the theory section will be closed when explaining the tweezer array and the tweezer Trap in section 3.2.2.

The simulation
Hereafter, when the essential theory is clear, the thesis will go into the simulation and how it operates. This will be done in five steps, starting with the simulation hypothesis, initialization and time iteration loop in section 4.1. Then the physical background in which the simulation runs and its effect on the detuning will be explained in section 4.2.1. After that, the dynamics of the internal quantum states of the atoms will be explained in section 4.2.2 followed by the forces and momenta kicks the particles experience in section 4.3.1. The simulation part will conclude by explaining the different energies, which can be calculated from the particles properties as will be done in section 4.3.2.

The results
The results will be presented in two main chapters. First the results of the simulation are shown in chapter 5, since these results are the most intuitive. Here, two experimental parameters will be highlighted, namely the Rabi frequency and the detuning. Varying these two parameters, the atom loss and the change in energy will be observed for one-particle simulation runs and for two-particle simulation runs. Then from these results, the influence of the two-body collisions will be abstracted, which will later form a trap loss profile for the quantum calculations.
In chapter 6, the thesis will go into the quantum calculation results, where first the wave function overlap results will be presented, followed by the trap loss calculations using three different trap loss profiles.

Part I

Theory

Chapter 2

Light-assisted collisions

In order to explain the theoretical part of the collision, we will first look into the semiclassical interpretation in section 2.1 and apply it to an already studied case where high preparation efficiencies have been reached, namely rubidium, in section 2.2. Then a shift to the quantum approach will be made when explaining the two-channel approach and the trap loss formula in section 2.3. To calculate the trap loss formula one will need the wave functions of both the ground state as the excited state as will be calculated in section 2.4. After introducing the wave functions, this thesis will explain the possible quantum states of the particles and how they will change over time under the influence of the laser light. This is theoretically explained and applied for the Rabi oscillation as for the Optical Bloch Equation (OBE) followed by the polarizability and the dressed state model, all in section 2.5. Finally, the master equation will be explained in section 2.6, as this will give insights into the mechanism of the trap losses.

2.1 Semiclassical approach

To understand light assisted collisions, it is useful to first consider the semiclassical formalism, which assumes continuous energies, positions and momenta, without any uncertainties. Another convention used in this approach, is that the atoms do not experience any external forces outside the trap. Also, three-body collisions, as described by Faddeev[15], do not occur frequently because of the relatively large trap and low atom number inside the trap causing low atom densities. It is therefore enough in this thesis to consider two-body collisions where just two atoms meet each other in space with an internuclear separation R.

To understand two-body collisions lets consider two atoms in the ground S state, forming a $|S + S\rangle$ channel together, they will interact in their ground state interaction potential $U_g(R)$ which, in the long-range, is asymptotically given by $U_g(R)_{R \to \infty} \approx -\frac{C_6}{R^6}$ where C_6 is a constant coming from the van der Waals-interaction [16]. This $|S + S\rangle$ interaction channel will feel a negligible interaction at large inter-atomic distances, as can be seen by its R^{-6} dependence, which dies off relatively quickly. This flat asymptotic regime can also be seen in figure 2.1. However, when particles are in this interaction regime at a few hundred Bohr radii, the laser light might excite one of the colliding atoms creating a $|S + P\rangle$ state. This excited state potential $U_e(R)$ has a long-range asymptote given by $U_e(R)_{R \to \infty} \approx \hbar\omega_0 \pm \frac{C_3}{R^3}$, where $\hbar\omega_0$ is the atomic excitation energy and C_3 is a constant arising from the resonant dipole interaction. This dipole interaction can either be attractive or repulsive, hence the $\pm$[16]. Also, since the dipole interaction scales with R^{-3} it is still very relevant at larger internuclear separations as can also be seen in figure 2.1.

In figure 2.1, both potentials, as a function of the interatomic distance are visualized. Depending on blue- or red-detuned laser light, that is to say a positive or negative detuned laser light, and by taking into account the angular momenta, a different $|S + P\rangle$ channel can be excited which will then determine whether the interaction will be repulsive (blue) or attractive (red). This detuning is defined by the equation $\Delta = \omega_L - \omega_0$, where ω_0 represents the natural frequency difference

between the $|S + S\rangle$ and $|S + P\rangle$ channels at large R and ω_L is the laser frequency. For both the blue- and the red-detuned laser light, a Condon point exists for which the laser light is resonant with this repulsive or attractive potential, that is to say there is zero detuning with respect to the transition at that particular R. At the this Condon point, the transition probability is the highest, which causes the highest excitation rate. Also, one could state that at the Condon point $U_e(R_c) - U_g(R_c) = \hbar\omega_L$. Calculating this for the ground and excited channel potentials gives a classical Condon point of

$$R_C = \left(\frac{C_3}{\hbar\Delta}\right)^{1/3}, \tag{2.1}$$

where $\hbar$ is the reduced Planck constant. This Condon point is typically in the order of hundreds of Bohr radii as we will also later see for strontium-88[12].
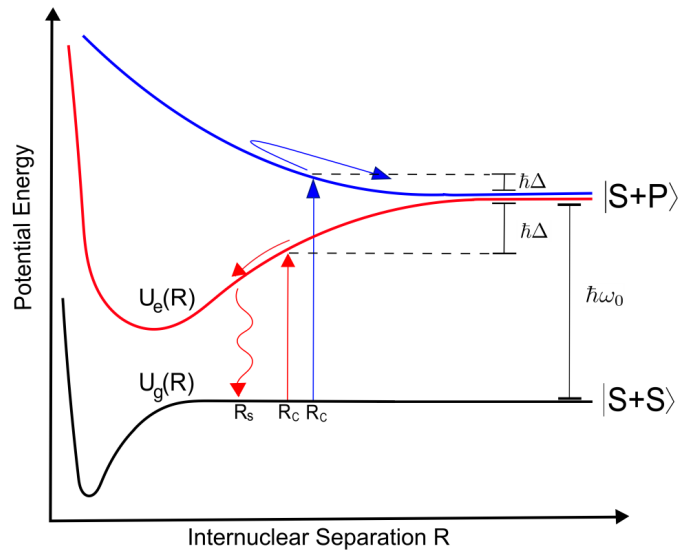
Figure 2.1: Potential landscape for the ground channel $|S + S\rangle$ and the excited state channel $|S + P\rangle$ for both blue and red detuning. The ground state channel is relatively flat because it has only a van der Waals interaction whereas the excited state also has a repulsive (blue) or attractive (red) dipole interaction term. Because of this dipole term the transition can become resonant with the excited state causing an excitation at the Condon point. Figure taken from [12].

2.2 Light-assisted collisions in rubidium

Since light-assisted collisions for the case of rubidium have already been proven to work, leading up to a 90% loading efficiency, it is fairly interesting to look at how this was achieved, and what can be learned from it for the case of strontium. In this experiment the atoms are first pumped to the so called 'S state' $^5S_{1/2}$, $F = 2$ level by a resonant laser light. These atoms are then illuminated by a nearly resonant light laser which can pump the atoms to the 'P state' $^5P_{3/2}$, $F' = 3$. This P state has a linewidth of $\Gamma/2\pi = 6MHz$ and the transition of the S to P state is $\lambda = 2\pi/k = 780\,\text{nm}$.[17]

In the experiment, it is very important to minimize the two-body losses, which happens when the kinetic energy gained by a single atom exceeds the trap depth U of the tweezer trap. This energy gain mechanism is caused by spontaneous emission and due to the cycles of absorbing and stimulated emission of the particles between the S state and P state. The quantum oscillations change the interaction strengths between the particles causing extra energy for the particles as explained in the previous section. For now we only consider the semiclassical example where two particles in the $|S + S\rangle$ channel approach each other without feeling any interaction because of the long flat asymptotic potential landscape. Then, when the particles approach the Condon

point, one of the particles gets excited, causing the atoms to interact via the repulsive potential. Once the particles move away from each other, there has been some gain in energy due to the movement along the excited state potential. The interaction potential, together with spontaneous emission, is causing all the energy fluctuations within the trap. The energy fluctuations are also represented below, as can be seen in figure 2.2. In subfigure A, one-body atom loss is visualized and in subfigure B, two-body atom loss is visualized. The main reason not both atoms left the trap in case A was the uneven energy E_p prior to the collision. To lower the overall energy, laser cooling techniques can be used during the process. This can be useful to keep energy deviations between the particles, while still lower the average energy of the system. This leaves the experimental physicist with several tunable variables which all effect each other as is done in the labs or will be done in our simulation.
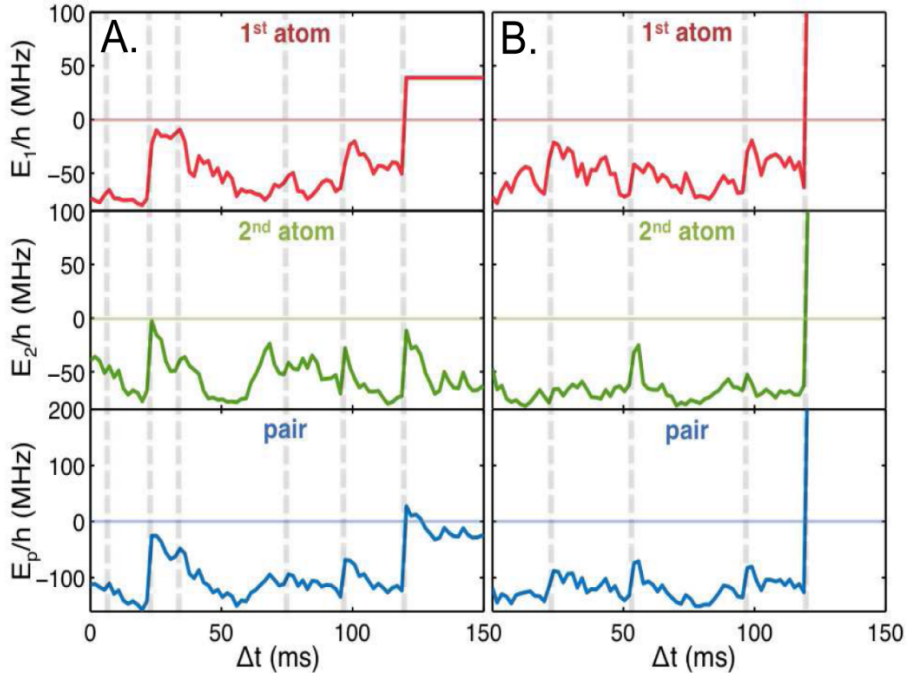
Figure 2.2: Energy fluctuations of the atoms inside a dipole trap in the case of Rubidium-85 as function of time. In the upper and middle plot the energy of the first and second particle can be seen and in the bottom plot the pair energy can be seen. Here figure (A) represents one atom loss whereas for in figure (B) on the right two atom loss is observed. Figure taken from [12].

In order to tune these mechanisms perfectly, one can try and change the parameters of the trap depth U, the intensity I of the laser light, the laser detuning δ with respect to the $S \rightarrow P$ transition and the cooling power.

2.3 Two channel approach and trap loss formula

Now that the semiclassical picture is clear, it is important to take a look to the quantum approach to this problem. For this formalism we will follow the thesis from Jasper van der Kraats [18]. Since we assume the collision takes place at $t = 0$, it is important to know how the states, also referred to as wave packet, move towards $t = 0$ (from either $\pm\infty$), and when the two particles start to feel an interaction potential. One expects that the orbit of the free state $|\phi(E, t)\rangle$ evolves into the orbit of the scattering state $|\Psi(E, t)\rangle$, which obeys the time dependent schrödinger equation.

In other words,

$$\lim_{t \to -\infty} e^{-\frac{i}{\hbar}Ht}|\psi(E)\rangle = e^{-\frac{i}{\hbar}H^c t}|\varphi_{\text{in}}(E)\rangle,$$

$$\lim_{t \to \infty} e^{-\frac{i}{\hbar}Ht}|\psi(E)\rangle = e^{-\frac{i}{\hbar}H^c t}|\varphi_{\text{out}}(E)\rangle \tag{2.2}$$

where $|\phi_{in}(E,t)\rangle$ represents the state that evolves into a scattering state and $|\phi_{out}(E,t)\rangle$ evolves out of a scattering state. Also, H represents the Hamiltonian of the scattering state and H_c represents the Hamiltonian of the free state. Using these asymptotic limits, it naturally follows that the Møller wave operator $\Omega_\pm$ can be states as

$$\Omega_\pm = \lim_{t \to \mp\infty} e^{\frac{i}{\hbar}Ht} e^{-\frac{i}{\hbar}H^c t}. \tag{2.3}$$

The Møller operators can be used to connect the in- and out-asymptotic wave functions to their respective scattering states as

$$\left|\psi^{(+)}(E)\right\rangle = \Omega_+ |\varphi_{\text{in}}(E)\rangle \quad \text{and} \quad \left|\psi^{(-)}(E)\right\rangle = \Omega_- |\varphi_{\text{out}}(E)\rangle. \tag{2.4}$$

Now, using these asymptotic solutions as incoming and outgoing states, a two-channel approach is necessary, following the treatment as discussed in [19], to describe the $|S + S\rangle$ and $|S + P\rangle$ channels. The Hamiltonian of a two-channel model with open channel subspace $\mathcal{P}$, representing the $|S + S\rangle$ channel, and another open channel subspace $\mathcal{Q}$, representing the $|S + P\rangle$ channel can be written as

$$H_{2\text{ch}} = \begin{pmatrix} H_{\text{PP}} & H_{\text{PQ}} \\ H_{\text{QP}} & H_{\text{QQ}} \end{pmatrix}. \tag{2.5}$$

Here, the off-diagonal matrix elements represent the coupling matrix strengths and the on-diagonal matrix elements represent the open channel Hamiltonians. An open channel is obtained if the energy of the particle is higher than the asymptotic interaction potential, which is the case as the particles always bounce off the repulsive interaction potential without entering the inner regime, which we saw earlier in section 2.1. In this framework, one can define the two component wave function $\Psi(r, E)$ as

$$\Psi(r, E) = \phi(r, E)|\mathcal{Q}\rangle + \psi(r, E)|\mathcal{P}\rangle, \tag{2.6}$$

consisting of $\phi(r, E)$ and $\psi(r, E)$ which are the distance-dependent components of the total wave function in the two channels. The two component wave function $\Psi(r, E)$ of the two-channel system is energy normalized, such that

$$\int_0^\infty \Psi^+(E)^* \Psi^+(E') \, dr = \delta(E - E'), \tag{2.7}$$

for $\mathcal{P}$, and

$$\int_0^\infty \Psi^-(E)^* \Psi^-(E') \, dr = \delta(E - E'), \tag{2.8}$$

for $\mathcal{Q}$. In the presence of an oscillating electric field $\vec{E}_{laser}$, an additional contribution of H_{mod} to the total Hamiltonian can be added, where

$$H_{mod} = -\vec{d} \cdot \vec{E}_{laser}, \tag{2.9}$$

with dipole moment $\vec{d}$. In the dressed state picture, one can identify an initial state $|\alpha, N\rangle$ and a final state $|\alpha', N+1\rangle$ of the transition in the strontium-88 atom, where α and α' represent the internal state of the two-atom system and where N and $N + 1$ indicate the number of quanta in the drive field. The Hamiltonian H_D in the dressed state picture, as has been done in Denise

Ahmed-Braun her paper [19], can then be written down as

$$
H_{\mathrm{D}} \rightarrow
\begin{pmatrix}
\ddots & & & \\
& [H_{2\mathrm{ch}}]_N & E_{laser}\begin{bmatrix} d_{\mathrm{p}} & 0 \\ 0 & d_{\mathrm{Q}} \end{bmatrix} & \\
& E_{laser}\begin{bmatrix} d_{\mathrm{p}} & 0 \\ 0 & d_{\mathrm{Q}} \end{bmatrix} & [H_{2\mathrm{ch}}]_N + \begin{bmatrix} \hbar\omega & 0 \\ 0 & \hbar\omega \end{bmatrix} & \\
& & & \ddots
\end{pmatrix}.
\tag{2.10}
$$

Applying this to Fermi's golden rule formula to calculate the transition rate from the initial free state $|\alpha, N\rangle$ to the final state $|\alpha', N+1\rangle$ results in

$$
\begin{aligned}
\gamma &= \frac{2\pi}{\hbar}\left|\langle\alpha, N+1\,|H_{\mathrm{mod}}|\,\alpha', N\rangle\right|^2 \\
&= \frac{2\pi\left(\delta\vec{d}\cdot\vec{E}_{\mathrm{laser}}\right)^2}{\hbar}\left|\int_0^\infty \psi^-(r,E)\,\psi^+(r,E)\right|^2 \mathrm{d}r,
\end{aligned}
\tag{2.11}
$$

which implies linear scaling of the transition rate with the Franck-Condon factor F_{fi}[20] as

$$
F_{fi} = \left|\int_0^\infty \psi^-(r,E)\,\psi^+(r,E)\right|^2.
\tag{2.12}
$$

The fact that the transition rate is linearly proportional with the Franck-Condon overlap could also be obtained semiclassically and has been done in appendix section A.1. This can then be extended to trap loss within the tweezer trap by considering on- and off resonant transitions as[19]

$$
\delta N = A'_N \int_{k_{\min}}^\infty P(T,E)F_{\mathrm{fi}}\left(k_{\mathrm{q}}\right)dk_{\mathrm{q}},
\tag{2.13}
$$

where A'_N is an experimental prefactor and $P(T,E)$ represents the Bose-Einstein distribution function of the ground state particles given as

$$
P(T,E) = \frac{1}{A\exp\{(E-\mu)/k_BT\}-1},
\tag{2.14}
$$

where μ is the chemical potential, T is the temperature and k_B is the Boltzmann constant. When performing the integral over all possible k values one considers all possible excitations. The total trap loss δN can then be calculated as a consequence of the overlap of the wave functions of the ground and excited state. The boundaries of the integral are defined from the lowest possible transitions k-vector k_{min} to the maximum k-vector which is infinity, since even the greatest positive detunings contribute to all possible transitions. The prefactor A'_N is an experimental scaling factor which scales with time but does not depend on the detuning.

However, equation (2.13) assumes that any transition will cause a decrease of the atom number in the trap. But this is not true, since some transitions do not give the maximum amount of energy possible to the system during a collision. Furthermore, this factor should depend on the shape of the trap, since this also influences the trap loss efficiency of an excitation. Keeping this inconvenience in mind, we make A'_N a function of the detuning $A'_N = A'_N(\Delta)$, since semiclassically we have seen that the detuning determines the amount of energy gain[19]. However, this factor cannot be calculated and has to be determined experimentally. In this report this factor will be determined using the simulation.

2.4   Quantum wave functions

In the previous section, three important profiles are introduced, namely the Bose-Einstein distribution profile $P(T,E)$, the Franck Condon profile F_{fi} and the trap dependent atom loss profile

$A'_N(\Delta)$. The Bose-Einstein distribution is a well-known distribution for bosonic particles, such as strontium-88, and does not require too much discussion. The trap dependent profile will be investigated using the simulation and the wave function overlap has to be calculated theoretically, as will be introduced in this section. The resulting wave function can later be seen in the results section 6.1. In this section, first the phase shift will be explained shortly since this is essential to why the short-term interaction can be approximated. After the phase shift discussion, it is convenient to talk about the analytic solutions of the short- and long-range wave functions for both the ground and the excited state.

2.4.1 Phase shifts

Since the phase shifts are so important to estimate the short-range of scattering problems, we will go into some details and show the derivation of how the phase shift can be determined. Many details are left in the appendix, but the general idea is stated here. To do this, let's consider a scattering problem with an infinite wall located at $x = 0$. On this wall, let's impose a plane wave wave function coming from the left as

$$\Psi_i(x) = Ae^{ikx}. \tag{2.15}$$

The reflection of such a plane wave on an infinite wall is maximum and thus the reflected wave function looks as

$$\Psi_r(x) = Be^{-ikx}. \tag{2.16}$$

By conservation of probability one can conclude that $B = -A$, since the wave function has to vanish at the position of the wall. The total wave function would then look like

$$\Psi = A(e^{ikx} - e^{-ikx}). \tag{2.17}$$

Now assume there is a non-zero potential left of the wall resulting in a phase shift δ of the scattered wave function. The new total wave function can then be written down as

$$\Psi = A(e^{ikx} - e^{i(2\delta - kx)}). \tag{2.18}$$

This equation however, does not treat angular momentum as a separate variable. For this, the Rayleigh formula (A.39) can be used, which states that the wave function $\Psi = Ae^{ikz}$ can be expressed for different angular momenta l as

$$\Psi^{(l)} = Ai^l(2l + 1)j_l(kr)P_l(\cos(\theta), \tag{2.19}$$

where j_l is the Bessel function of l-th order and P_l is the spherical harmonic function of degree l. Equation (2.19) can then be approximated for large r as

$$\Psi^{(l)} \approx A\frac{(2l + 1)}{2ikr} \left[e^{ikr} - (-1)^l e^{-ikr}\right] P_l(\cos\theta), \tag{2.20}$$

in which the relation regarding the Hankel function from equation (A.32) has been used yielding

$$j_l(x) = \frac{1}{2}\left[h_l^{(1)}(x) + h_l^{(2)}(x)\right] \approx \frac{1}{2x}\left[(-i)^{l+1}e^{ix} + l^{l+1}e^{-ix}\right], \tag{2.21}$$

which would have been the scattering Schrödinger equation without any potential. If now a potential is introduced, the first term of equation (2.21) picks up a phase shift due to the scattering potential, which yields

$$\Psi^{(l)} \approx A\frac{(2l + 1)}{2ikr}\left[e^{i(kr + 2\delta_l)} - (-1)^l e^{-ikr}\right] P_l(cos\Theta). \tag{2.22}$$

In order to connect this equation to other well-known equations it is useful to first consider the scattering formalism. In this formalism, the Schrödinger equation has been solved in a series of

steps, which in this thesis, has been done in the appendices. Starting with the Lippmann-Schwinger equation in section A.2 resulting in the formula (A.10) as

$$|\psi\rangle = |\phi\rangle + \frac{1}{E - H_0 + i\epsilon} V |\psi\rangle, \tag{2.23}$$

where H_0 is the Hamiltonian in which the two particles are infinitely far apart and do not interact. The eigenfunctions of this Hamiltonian are $|\phi\rangle$ and its eigenvalues are the energies E, $i\epsilon$ is a mathematical necessary to do the integral. Then the Green functions in section A.3 have been used to accurately describe the solution of the Lippmann-Schwinger equation for a point source potential. Finally, in section A.4, the general form of the scattering wave function is presented as

$$\psi(\mathbf{r}) \sim e^{ikz} + f(\theta, \phi) \frac{e^{ikr}}{r}, \tag{2.24}$$

where the first part of the equation is the incoming wave and the second part is the scattered wave with scattering amplitude $f(\theta, \phi)$, where θ and ϕ represent the azimuthal and polar angle respectively. This general form is then used in section A.5 using the partial wave formalism to derive an expression as a function of the partial wave amplitudes (A.36) and reads

$$\psi(r, \theta) = A \left\{ e^{ikz} + k \sum_{\ell=0}^{\infty} i^{\ell+1}(2\ell + 1) a_\ell h_\ell^{(1)}(kr) P_\ell(\cos\theta) \right\}, \tag{2.25}$$

and again, the first part represents the incoming wave and the second part represents the scattered wave. This formula, together with formula (2.22), both describe the same state and the formulas are related to each other with a relation between the phase shifts δ and the partial wave amplitudes a_l in the limit of large r ($r \Rightarrow \infty$) as

$$a_l = \frac{1}{2ik}(e^{2i\delta_l} - 1) = \frac{1}{k} e^{i\delta_l} sin(\delta_l), \tag{2.26}$$

where a_l is the scattering length, describing the short-range interactions, and will later be used for the long-range wave function in an interaction scattering potential[21].

2.4.2 Short-range ground state wave function in a van der Waals potential

In the previous subsection, we discussed the phase shift and the corresponding scattering length which both are a consequence of introducing a non-zero interaction potential. This interaction potential influences the short-range wave function, relative to a perfect infinite wall potential, causing a phase shift to emerge. However, this short-range potential is still important for the total wave function and can sometimes be solved analytically, as we will do in this section, following the discussion in [18]. Starting off with the well-known radial Schrödinger equation

$$-\frac{\hbar^2}{2m} \frac{\partial^2 u(E, r)}{\partial r^2} + \left[V(r) + \frac{\hbar^2}{2\mu} \frac{l(l+1)}{r^2} \right] u(E, r) = E u(E, r), \tag{2.27}$$

where μ is the reduced mass. It is important to note that $u(E, r) \equiv rR(r)$ where $R(r)$ is the radial wave function. To calculate the ground state wave function, only a van der Waals potential $V(r)$ has to be taken into account, defined as $-\frac{C_6}{r^6}$. Furthermore, the centrifugal term can be neglected as $l = 0$, representing only s-wave scattering. This is the case as only extreme low energies have been used and strontium-88 is bosonic [22]. Filling in the potential and rewriting equation (2.27) gives

$$\frac{\partial^2}{\partial r^2} u(E, r) + \frac{2\mu C_6}{\hbar^2} \frac{1}{r^6} u(E, r) = \frac{2\mu}{\hbar^2} E u(E, r). \tag{2.28}$$

This can be rewritten in terms of r_{vdW} and E_{vdW}, which are given as

$$r_{\text{vdW}} = \frac{1}{2} \left(\frac{2\mu C_6}{\hbar^2} \right)^{\frac{1}{4}} \quad \text{and} \quad E_{\text{vdW}} = \frac{\hbar^2}{2\mu r_{\text{vdw}}^2}. \tag{2.29}$$

Filling in these values and introducing the dimensionless variables $x = r/r_{vdW}$ and $\xi = E/E_{vdW}$ gives the dimensionless radial Schrödinger equation as

$$\frac{\partial^2}{\partial x^2} u(\xi, x) + \frac{16}{x^6} u(\xi, x) = \xi u(\xi, x). \tag{2.30}$$

The problem with only using the van der Waals potential become apparent at the short-range where no repulsion is taken into account. This can be approximated using the WKB formalism, as described in appendix A.7.1, in which a turning point divides a forbidden region, where $E < V$, and a classical region, where $E > V$. Also, the energy of the particle is small with respect to height of the interaction and can therefore be neglected. Therefore, a classical momentum can be expressed in known variables for the short-range forbidden region as

$$k(r) = \sqrt{\frac{-2\mu V(r)}{\hbar^2}}. \tag{2.31}$$

For the classical region $r > r_0$, one can estimate the radial wave function until r_0 by patching it across the barrier as

$$u_{\text{wkB}}(r) = \frac{1}{\sqrt{\kappa(\mu)}} \cos \left(\int_{r_0}^r dr(r) - \frac{\pi}{4} \right). \tag{2.32}$$

For $r > r_0$ which is of the order of the van der Waals length r_{vdW} the short-range potential can be neglected again and the radial equation can be calculated using equation (2.30). Again, at zero energy, the solution to this equation is given by a Bessels function of order $1/4$, which becomes explicit by defining $u(x) = \sqrt{x}v(x)$. The most general solutions to the Bessel function are given as

$$u(x) = \sqrt{x} \left[AJ_{\frac{1}{4}} \left(\frac{2}{x^2} \right) + BY_{\frac{1}{4}} \left(\frac{2}{x^2} \right) \right], \tag{2.33}$$

which can then be rewritten in the form

$$u(x) = \sqrt{x} \left[\Gamma \left(\frac{5}{4} \right) J_{\frac{1}{4}} \left(\frac{2}{x^2} \right) - \frac{r_{\text{vdW}}}{a} \Gamma \left(\frac{3}{4} \right) J_{-\frac{1}{4}} \left(\frac{2}{x^2} \right) \right], \tag{2.34}$$

where a is the mean scattering length given by

$$a = \bar{a} \left[1 + \frac{A}{B} \right] \quad \text{with} \quad \bar{a} = \frac{4\pi}{\Gamma \left(\frac{1}{4} \right)^2} r_{\text{vdW}}. \tag{2.35}$$

However, instead of using the rewritten form it is much more convenient to take the general solution from equation (2.33) and to continuously connect it to the long-range wave function using the log derivative method[23].

2.4.3 Short-range wave function in the excited state potential

In the excited state potential, the short-range is relatively easy. Because of the repulsive interaction potential, this regime is classically forbidden for internuclear distances smaller than the Condon point. The potential in the relevant interaction regime goes as $\frac{C_3}{r^3}$ up to $25\,\text{MHz}$ before it goes down at smaller r. However, this short-range regime cannot be reached, since only detunings smaller than the maximum of the potential hill are considered. This ultimately leaves us with the WKB solutions (A.61) from the appendix as

$$\psi(x) \approx \begin{cases} \frac{D'}{\sqrt{|p(x)|}} \exp \left[-\frac{1}{\hbar} \int_x^{x_1} |p(x')|\, dx' \right], & x < x_1 \\ \frac{2D'}{\sqrt{p(x)}} \sin \left[\frac{1}{\hbar} \int_{x_1}^x p(x')\, dx' + \frac{\pi}{4} \right], & x > x_1 \end{cases} \tag{2.36}$$

for the downward slope representing the repulsive potential. x_1 is the Condon point here dividing the classically forbidden and allowed regions, $P(x')$ is the momentum of the particle and D' is a normalization factor. Around the Condon point, Airy functions are solutions of the Schrödinger equation. These Airy functions connect the plane wave solution, with the constant k, on the right side, as will be discussed in next section 2.4.4, together with the decaying wave function on the left side[21].

The same solutions for this excited state potential could be achieved using propagation methods, as has also been done to confirm the results. One way of doing this is using the SC-model where SC stands for Single Channel. In this numeric calculation, the script first calculates a propagator Q_i connecting two adjacent grid points as

$$u_{i-1} = Q_i u_i. \tag{2.37}$$

Then, given an initial condition for the wave function, for example in the asymptotic limit, it can work out the ratios backwards. This is quite useful in case two initial conditions are needed for the problem[12].

However, in this case also an easier approach could be considered, namely the finite difference method as described in appendix A.6. Using this method, the next element can be calculated by discretizing the Schrödinger equation. This leaves the forward difference equation

$$\Psi_n = (\frac{77}{6}\Psi_{n+1} - \frac{107}{6}\Psi_{n+2} + 13\Psi_{n+3} - \frac{61}{12}\Psi_{n+4} + \frac{5}{6}\Psi_{n+5})/(\frac{15}{4} + a^2 k_n^2). \tag{2.38}$$

Where a is the grid size and k_n is the k-vector at grid size n given by

$$k_n = \frac{\sqrt{2\mu(E - V_n)}}{\hbar} \tag{2.39}$$

These equations together calculate the nth grid point as function of later grid points which can be useful when only an initial condition is set from the asymptotic regime as is the case for many scattering problems. The resulting error is up to fourth order accuracy which means that the error is decreased by a factor of 10^{-4} as the grid size decreases by a factor.

2.4.4 Wave function in the asymptotic limit

Now that the short-range wave function and the wave function in the intermediate regime have been explained for both the ground and the excited interaction channel potential, it is very important to talk about the asymptotic regime of these wave functions. This can then be fitted to the short-range either by using the log derivative method or simply as initial condition for the propagation methods described in section 2.4.3. This asymptotic wave function is nothing more than a plane wave with a phase shift, related to the scattering length, as postulated in equation (2.18). This can then be rewritten in a similar way as has been done for the phase shift in section 2.4.1, yielding

$$u(E, r) \xrightarrow{r \Rightarrow \infty} e^{i\delta_l(E)} \frac{\sin(kr - l\frac{\pi}{2} + \delta_l(E))}{\sqrt{k}} \tag{2.40}$$

Where $k = \sqrt{\frac{2m(E-V)}{\hbar^2}}$ and

$$\lim_{k \to 0} k \cot \delta(k) = -\frac{1}{a} \tag{2.41}$$

defining the phase shift $\delta(k)$ as function of the scattering length a in the low energy limit[18].

2.5 Internal quantum states

In this section, the effects of the detuning and Rabi frequency are theoretically discussed in order to understand the simulation better. This will be done by starting to explain the Rabi oscillations

and its off-resonance solutions to explain absorption and stimulated emission. Then, we will go into the Optical Bloch Equations (OBEs) from which also the solutions are showed, this will be done to implement spontaneous emission into the picture. This section about the internal atom state will be finished with an explanation of the dressed state model and the polarizability to explain the differential Stark shift.

2.5.1 Rabi oscillations

Strontium atoms moving inside the tweezer trap will feel a sinusoidal time dependent electric field from the collision laser. This collision laser with a certain Rabi frequency Ω and detuning δ induces excitations and stimulated emissions in the particles. Depending on the resonance condition, the particles will oscillate in their internal quantum state between the ground state $|\Psi_g\rangle$ and the excited state $|\Psi_e\rangle$. The general solution for this time dependent wave function in superposition is given by[21]

$$\Psi(t) = c_g\Psi_g e^{-iE_g t/\hbar} + c_e\Psi_e e^{-iE_e t/\hbar}. \tag{2.42}$$

where c_g and c_e are the coefficients of the ground and excited state respectively. If one would now consider a sinusoidal time dependent electric field as

$$\hat{H}'(r,t) = V(r)\cos(\omega t), \tag{2.43}$$

and apply this as a perturbation to the original Hamiltonain one can find the rate equation for the coefficients. This has been done in appendix A.8.1 and the solutions are [24]

$$i\dot{c}_g = \frac{\Omega}{2}e^{i\delta t}c_e \quad \text{and} \quad i\dot{c}_e = \frac{\Omega}{2}e^{-i\delta t}c_g, \tag{2.44}$$

where Ω and δ are again the Rabi frequency and the detuning of the collision laser and i is the imaginary number. The solutions of these equations are given as the square of the coefficients $|c_e(t)|^2$ and has been done for the appendix section A.8.2. The probability of being in the excited state $P_e(t)$ is given as[25]

$$P_e(t) = |c_e(t)|^2 = \frac{\Omega^2}{\Omega^2 + \delta^2}\sin^2\left(\frac{\sqrt{\Omega^2 + \delta^2}}{2}t\right). \tag{2.45}$$

Here we see an oscillation amplitude of $\frac{\Omega^2}{\Omega^2 + \delta^2}$ and a oscillation frequency of $\sqrt{\Omega^2 + \delta^2}$. this new oscillation frequency is also defined as the generalised frequency and depends now on the detuning as will also be the case in our simulation. However, these solutions are only for a constant Rabi frequency and detuning whereas the particles in the simulation experience a different relative detuning due to the interaction energy and the differential Stark shift. Therefore we will still refer back to the rate equations for the coefficients (2.44) while also talk about the Rabi oscillation amplitude and generalised frequency to understand the underlying physics.

2.5.2 Optical Bloch equations

Since the Rabi oscillation framework only takes into account excitations and stimulated emission, it is now useful to talk about the optical Bloch equations(OBEs). These OBEs also take into account spontaneous emission by coupling the atom to the vacuum field[26]. The derivation of this coupling leads to four coupled rate equations for the density matrix terms ρ_{gg}, ρ_{ee}, ρ_{ge} and ρ_{eg} which hs been done in appendix A.8.3 and yields

$$\begin{aligned}
\frac{d\rho_{gg}}{dt} &= +\gamma\rho_{ee} + \frac{i}{2}\left(\Omega^*\tilde{\rho}_{eg} - \Omega\tilde{\rho}_{ge}\right) \\
\frac{d\rho_{ee}}{dt} &= -\gamma\rho_{ee} + \frac{i}{2}\left(\Omega\tilde{\rho}_{ge} - \Omega^*\tilde{\rho}_{eg}\right) \\
\frac{d\tilde{\rho}_{ge}}{dt} &= -\left(\frac{\gamma}{2} + i\delta\right)\tilde{\rho}_{ge} + \frac{i}{2}\Omega^*\left(\rho_{ee} - \rho_{gg}\right) \\
\frac{d\tilde{\rho}_{eg}}{dt} &= -\left(\frac{\gamma}{2} - i\delta\right)\tilde{\rho}_{eg} + \frac{i}{2}\Omega\left(\rho_{gg} - \rho_{ee}\right),
\end{aligned} \tag{2.46}$$

where $\tilde{\rho}_{ge} \equiv \rho_{ge}e^{-i\delta t}$ and also $\mathrm{d}\rho_{ee}/\mathrm{d}t = -\mathrm{d}\rho_{gg}/\mathrm{d}t$, which is required in order to conserve the total population number, stated as $\rho_{gg} + \rho_{ee} = 1$. Also, γ is the linewidth defined as $1/\tau$, where τ is the lifetime of the excited state[26].

However, also here the solutions give a more intuitive answer to the problem and interesting properties can be abstracted from it. The derivation of these solutions are given in appendix A.8.4 and yield an expression for the factor ρ_{ee} in the steady state solution as[26]

$$\rho_{ee} = \frac{1}{2}(1-w) = \frac{s}{2(1+s)} = \frac{s_0/2}{1+s_0+(2\delta/\gamma)^2}, \tag{2.47}$$

where s_0 is the on resonance saturation parameter indicating how saturated the transition is for a given laser intensity. δ is again the detuning of the laser and γ is the line width. From the excited state population one can introduce the concepts of the scattering rate and the power broadening linewidth as has been done in the appendixA.8.4. The results can be summarized with the expressions

$$\gamma_p = \gamma\rho_{ee} = \frac{s_0\gamma/2}{1+s_0+(2\delta/\gamma)^2}. \tag{2.48}$$

for the scattering rate, representing the effective scattering of the collision laser onto the strontium-88 atom, and for the power-broadened linewidth

$$\gamma' = \gamma\sqrt{1+s_0}. \tag{2.49}$$

This new line width is a consequence of the intensity of the laser, which is expressed with the on resonance saturation parameter s_0. In figure 2.3 the effects for various saturation parameters are shown. As we can see is the scattering rate of the laser higher for a higher saturation. Because of this power broadening it is still likely to excite atoms with high saturation with large detunings as would otherwise not be very likely. This supports the ranges we will ultimately test in the simulation. However, in the simulation we will compute the rate equations from the Rabi oscillation framework rather than the optical Bloch equations. This has been done as the optical Bloch equations do not give discrete photon decays. Rather, the particles experience decoherence into the mixed states. This problem and the solution for the simulation is carefully explained in section 4.2.2. In short, we will imitate the spontaneous emission processes by a decay curve which determines the probability of decaying rather than having a continuous decay. This probability will then lead to a discreet energy jump resulting in photon decay and a momentum kick for the strontium-88 atom.
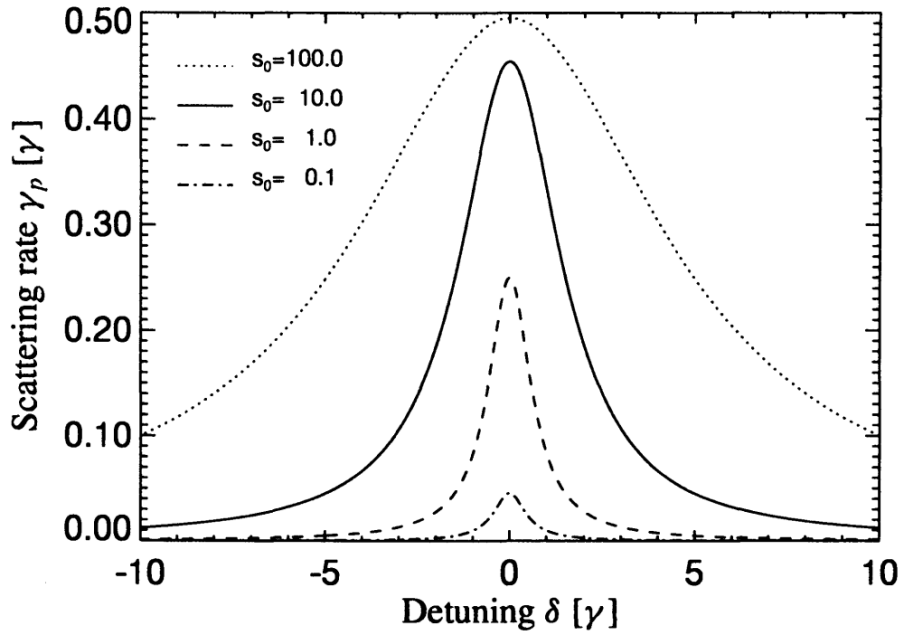
Figure 2.3: Scattering rate γ_p as a function of the detuning δ for different values of the on resonance parameter s_0. Here it can be seen that the scattering rate decreases as the detuning gets bigger or smaller than zero. Also the lines broaden out substantially as $s_0 > 0$ called power broadening. Figure taken from [26].

2.5.3 Differential Stark shift

The last effect of the collision laser on the atoms is caused by the differential Stark shift. This shift determines the spacing between the ground and excited state levels. This energy spacing then influences the effective detuning set by the laser outside the trap. This shift in energy levels can be explained though the dressed state model as has been done in appendix section A.8.5 and can be done using the concept of polarizability as has been done in appendix section A.8.6, but a short summary will be given below.

In the dressed state model, the rotating frame approximation has been added to the ground and excited state coefficients leading to an set of coupled rate equations for the coefficients c_g and c_e. These equations can be put in a matrix form and get diagonalized to get the eigenstates of the system. Doing this leads to two new eigenstates[26]

$$E_{e,g} = \frac{\hbar}{2} \left(-\delta \mp \Omega'\right), \tag{2.50}$$

which are now dependent on the detuning of the laser δ and the generalized Rabi frequency Ω' introduced in section 2.5.1.

In the polarizability framework, the two energy levels are not shifted by the same amount, rather the shifts depend on the polarizability. The polarizability of an atom describes the tendency, when subjected to an electric field, to acquire an electric dipole moment in proportion to that applied field. This polarizability is therefore proportional to the dipole matrix element, while also being inversely proportional to the detuning of the laser. When summing over all possible transitions contributing to the polarizability one can obtain an expression for the total polarizability as has been done in the appendix A.8.6. The differential Stark shift as function of the polarizability of state i can then be calculated from the equation[27]

$$E_{dSs} = h\Delta\nu = -\frac{1}{2}\alpha_i |\mathbf{E}|^2, \tag{2.51}$$

where $|\mathbf{E}|^2$ is the electric field of the trapping laser squared. For the qubits in the trap it is desirable to have an equal differential Stark shift between the two qubit states. These qubit states in a strontium-88 computer are chosen to be $^1S_0$ and $^3P_1$ as will be discussed later in section 3.1. However, given these states, one can look for a lattice wavelength where the differential Stark shift is equal for both states. This wavelength is called the magic wavelength. The differential Stark shift is shown in figure 2.4 for lattice wavelength between $0\,\mu m$ and $4.5\,\mu m$ for both the qubit states. Multiple crossings can be seen representing the magic wavelength. However, a magic wavelength with small slope is preferred and can be found in the region between $0.75\,\mu m$ and $1\,\mu m$[28]. In this region also commercial lasers are available, which makes it ideal in practice[29]. Zooming into this region gives figure 2.5. Here, a value of $815\,nm$ can be estimated to be the magic wavelength. This value is equal to the theoretical value of $815\,nm$[30], which could have been calculated from the derivation in the appendix A.8.6.

The reason why specifically these states have been chosen to define the magic wavelength has to do with the qubit states. These $^1S_0$ and $^3P_0$ qubit states have a particularly long lifetime, which makes them ideal for quantum computing and having the same differential Stark shift per qubit state is convenient for qubit manipulation[31]. However, since the light assisted collision uses the $^1S_0$ and $^3P_1$ states of strontium-88, a difference in differential Stark shift is expected in the simulation as will later be explained in section 4.2.1. This differential Stark shift depends on the position of the atoms in the tweezer trap, as the intensity profile of the trapping laser depends on position, making also the effective detuning depend on the position.
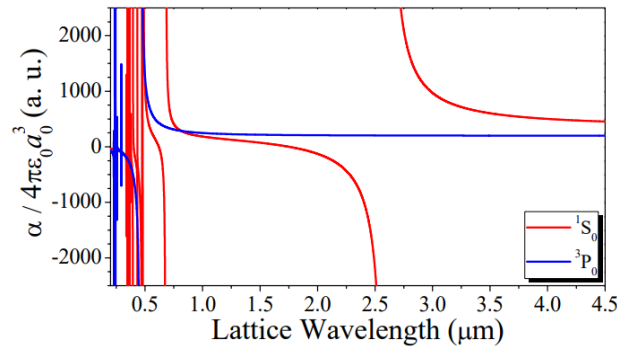
Figure 2.4: Differential Stark shift as a function of the lattice wavelength between $0.5\,\mu m$ and $4.5\,\mu m$ for both the $^1S_0$ state (red) as the $^3P_0$ state (blue). Figure taken from [30].
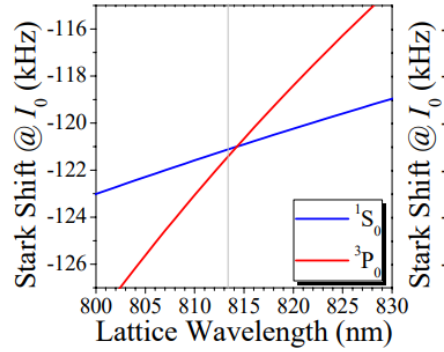
Figure 2.5: Differential Stark shift as a function of the lattice wavelength between $0.8\,\mu m$ and $0.83\,\mu m$ for both the $^1S_0$ state (blue) as the $^3P_0$ state (red). Figure taken from [30].

2.6 Atom trap loss rate master equation

To finish the the theory discussion, the number of strontium-88 atoms in a trap will be described by the rate master equation. Both one-body losses as two-body losses will contribute to the trap loss as described in section 1.1. The probability of a one-body loss to happen during dt is $\gamma N dt p_N(t)$ and for the two-body loss it is $\beta \frac{N(N-1)}{2} dt p_N(t)$, where $\frac{N(N-1)}{2}$ is the amount of 2 atom arrangements given N atoms in total. These processes yield the following equation for the

probability $p_N(t)$ to have N atoms in the dipole trap

$$p_N(t + dt) = p_N(t)(1 - \left[\gamma N + \beta \frac{N(N-1)}{2}\right]dt) \tag{2.52}$$

$$+ p_{N+1}(t)\gamma(N + 1)dt \tag{2.53}$$

$$+ p_{N+2}(t)\beta \frac{(N+2)(N+1)}{2}dt. \tag{2.54}$$

Taking the limit $dt \to 0$ yields the following master equation for the evolution of $p_N(t)$ over time

$$\frac{dp_N}{dt} = \beta(E^2 - 1)\left[\frac{N(N-1)}{2}p_n\right] + \gamma(E - 1)[N_{P_N}]. \tag{2.55}$$

Here, E is called the step operator defined by its effect on an arbitrary function $f(N)$ as

$$E[f(N)] = f(N + 1) \quad \text{and} \quad E^{-1}[f(N)] = f(N - 1). \tag{2.56}$$

If then the average number of atoms in the trap is defined as $\langle N \rangle = \sum_{N=0}^{\infty} N_{p_N}$, also the master equation for this property can be derived using equation (2.55)

$$\frac{d\langle N \rangle}{dt} = -\gamma\langle N \rangle - \beta\langle N \rangle(\langle N \rangle - 1) - \beta\Delta N^2, \tag{2.57}$$

with ΔN^2 the variance of the atom number in the trap. This equation can be solved for the sub poissonian assumption ($\beta\Delta N^2 = 0$) by integrating over time and rearranging it for $\langle N \rangle$ yielding

$$\langle N(t) \rangle = \frac{e^{(\beta-\gamma)t}}{\frac{\beta}{\beta-\gamma}(e^{(\beta-\gamma)t} - 1) + \frac{1}{N_0}}, \tag{2.58}$$

with N_0 the initial atom number. Determining the factors β and γ would determine the one-body over two-body losses[32]. However the main conclusion that we draw is that the population decays exponentially when the initial number of atoms is large. The exponential decay factor will be explored as a function of the detuning in the quantum calculations.

Chapter 3

Experimental constraints

To get a better overview of the strontium-88 atoms at play in order to manipulate them with the collision laser, it is important to go into detail of some key properties, such as the relevant electron shells and the level scheme, the interaction potentials and other relevant constants of strontium-88 such as the scattering length and the mass of the atom. These properties have a direct effect on the interaction between the atoms and should therefore be well understood to optimize the scattering processes. This will be done in section 3.1. After the atomic properties, this paper will go into the temperature limits, that can be reached with different cooling techniques as will be done in section 3.2. These temperature limits are reached in preparation of the collision processes but give an intuitive answer to why the atoms heat up during the simulation. After explaining the temperature limits, the optical tweezer array followed by the individual tweezer traps will be explained in section 3.2.2.

3.1 Strontium-88

Strontium-88 has 38 protons, 50 neutrons and 38 electrons, two of which are in the valence shell, which makes strontium-88 an alkaline earth atom with an electronic level structure ideal for laser manipulation and for the realisation of quantum devices. strontium-88 has no nuclear spin, since all spins inside the nucleus cancel each other. Since it also has an even number of neutrons Strontium-88 is an bosonic isotope, which simplifies the electronic energy spectrum greatly. This also makes it very insensitive to stray magnetic fields, as it is not affected by the magnetic field of the nucleus[33]. In figure 3.2, the electronic level structure of strontium can be seen. We choose the $(5s5s)$ $^1S_0$ state together with the $(5s5p)$ $^3P_0$ state to form the qubit states of the strontium atom, as was introduced for the magic wavelength in section A.8.6. These states are connected by a 698 nm transition with a relatively small linewidth, compared to other transitions in strontium-88, causing the transition rate between the states to be low. As a consequence this $^3P_0$ state is long lived and ideal for quantum computing due to its long coherence time. The states relevant for light-assisted collisions are the $(5s5s)$ $^1S_0$ and $(5s5p)$ $^3P_1$ states, which are connected by a transition of 689 nm and a linewidth of 7.4 kHz[33].
The S and P states form a $|S + P\rangle$ channel in which the interaction potentials are given by

$$V(R) = \frac{C_3}{R^3} - \frac{C_6}{R^6} \tag{3.1}$$

Where for the S state $C_3 = 0$, since there is no dipole interaction and $C_6 = 3103\,E_\mathrm{h}a_0{}^6$, where E_h is the Hartree energy and a_0 is the Bohr radius. For the P state there are two interaction potentials. Namely $C_3 = -0.015\,E_\mathrm{h}a_0{}^3$ and $C_6 = 3513.8\,E_\mathrm{h}a_0{}^6$ for the $|S + P\rangle$, $m_J = 0$ channel and $C_3 = 0.0075\,E_\mathrm{h}a_0{}^3$ and $C_6 = 3773.85\,E_\mathrm{h}a_0{}^6$ for the $|S + P\rangle$, $|m_J| = 1$ channel[34]. These excited state potentials are respectively called the $0u$ and $1u$ potentials and are both plotted in figure 3.1. Here one can see the $0u$ potential is attractive and the $1u$ potential is repulsive for

particles coming closer to each other from the asymptotic regime.

The repulsive excited state potential $1u$ will be used for the light assisted collisions, since this repulsive potential makes it easier to tune the energy gain per collisions. This is the case as particles will mostly interact in the regime outside of the Condon point, particles will therefore not come close to each other creating oscillatory bonds between the particles[35]. The $1u$ potential creates a potential barrier of 25 MHz at approximately $100\,a_0$. This barrier prevents particles from going below internuclear distances of the Condon point. Therefore, particles will not interact in the short-range besides any tunneling effects decreasing the complexity of the scattering processes. In order to excite particles properly from the $|S + S\rangle$ state to the $|S + P\rangle$ state the quantum number $|m_J|$ has to be changed by +1. To do this a $\sigma+$ laser can be used.
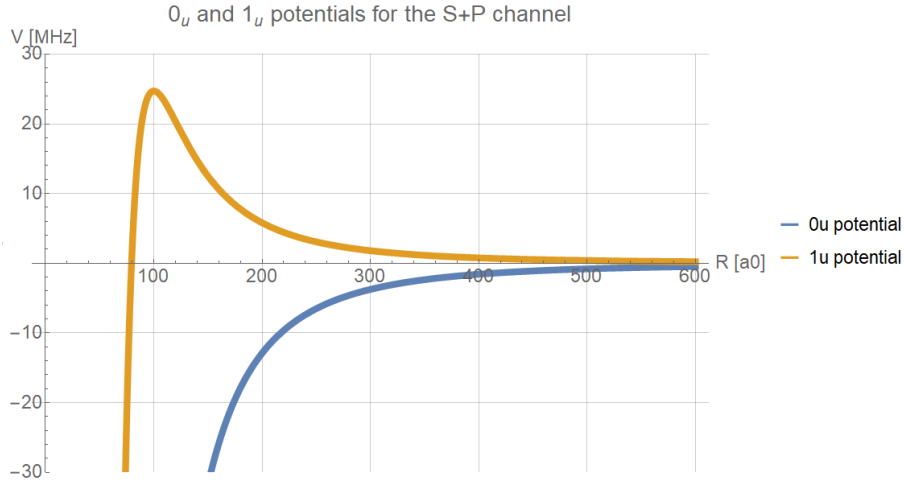
Figure 3.1: Both the $0u$ and $1u$ potential for the excited state channel. In the asymptotic regime both potential go to zero in the plot. The repulsive $1u$ potential which is of interest shows a maximum 25 MHz around approximately $100\,a_0$.

Another property of strontium-88 of interest is its scattering length, since this is necessary to calculate the wave functions. In a paper from Simon Stellmer and Florian Schreck, the scattering lengths of 4 papers were compared, and the average was taken to be $a = -2\,a_0$[36]. The mass of strontium-88 is 87.91 u[37]. The last physical property of importance for this thesis is the lifetime of the excited 1u potential of strontium-88. Inside the tweezer trap, the lifetime is estimated to be 21.5 s[38], this value could also have been calculated using Einstein's rate coefficients defined in section A.9.

Figure 3.2: Electronic level structure of atomic strontium. Here on the left side the $s = 0$ states and on the right side the $s = 1$ states are categorized. The atomic transitions are given by the arrows between the energy levels with the corresponding line widths of the transitions. The $^1S_0 - {}^1P_1$ transition is important for the blue MOT, whereas the $^1S_0 - {}^3P_1$ narrow transition is important for the 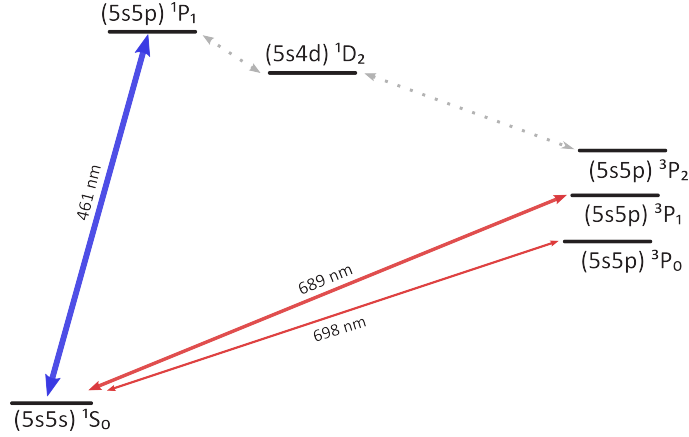red MOT. This relation between the linewidth and the cooling temperature will be further explained in section 3.2. The qubit states are $^1S_0$ and $^3P_0$ and the states used for light-assisted collisions are $^1S_0$ and $^3P_1$[33].

3.2 Temperature limits and tweezer trap

Apart from the internal structure of strontium-88, also the effects of the environment on the strontium-88 atom will be explained. This will be done in combination with explaining the Doppler and recoil temperature limits in section 3.2.1, as this information will be used for the interpretation of the simulation results. Moreover, the trapping laser will be explained together with the tweezer array in section 3.2.2. Here, the polarizability and the intensity profile are the main focus as both these values will influence the internal state of the strontium-88 atoms by the differential Stark shift, explained in the theory section 2.5.

3.2.1 Temperature limits

To consider the temperature limits let us consider the forces from the trap on the atom first. First, a Magneto Optical Trap (MOT) is used to cool the atoms before the tweezer trap is used. The MOT consists of six circular polarized laser beams. The technique relies on an atom absorbing and then re-emitting a photon, thereby losing momentum. To do this in a coordinated manner, a spatially-varying magnetic field is created to trap the cold atoms. Usually, an anti-Helmholtz configuration is used, which consists of two counter propagating coils on the z-axis, such that magnetic field between the coils is zero and varies linearly with position.

This magnetic field is important because it creates a spatially-varying Zeeman shift. This Zeeman shift then allows either σ^+ polarized right from the right or σ^- polarized light from the left to exert a scattering force on the $m_J = +1$ and $m_J = -1$ states respectively. This will result in a net force towards zero as

$$F = F_- + F_+ = \frac{\hbar k \gamma s_0}{2} \left\{ \frac{1}{1 + s_0 + (2\frac{\delta - \omega_z}{\gamma})^2} - \frac{1}{1 + s_0 + (2\frac{\delta + \omega_z}{\gamma})^2} \right\}, \tag{3.2}$$

where $\hbar k$ is the momentum of the photon, γ is the linewidth of the transition, s_0 is the saturation parameter and ω_z is the atomic transition frequency including the Zeeman and Doppler shift given as $\omega_z = k_z v - g\mu_0 dBz$[20].

Now that forces of the MOT are explained, one can derive temperature limits related to the traps.

The cooling process is limited by the randomness of the momentum kicks from either the lasers or the momentum kicks due to spontaneous emission of the atom, which depends on the transition rate $\Gamma = 1/\tau$ and the discrete size of each momentum kick. This limit is known as the Doppler limit which is given by

$$k_B T_D = \hbar \Gamma / 2. \tag{3.3}$$

Γ is the transition linewidth at Full Width Half Maximum (FWHM) in rad/s[20].

Another cooling process, which cools the atoms below the Doppler limit, is called Sisyphus cooling[11]. Using a 813.4 nm tweezer wavelength one can create an potential a potential landscape due to the differential Stark shift as can be seen in figure 3.3. In this potential landscape, one can selectively excite atoms, when they are at the lowest energy point of the ground state. After the excitation, the atom will roll up in the excited state before decaying back to the ground state, as can also be seen in the figure. For Sisyphus cooling to work, three criteria have to be fulfilled. First, the excited state has to be more confined than the ground state as this will lower the energy if the atoms moves in the excite potential relative to the ground potential. Second, one must selectively excite atoms to the excited state from the bottom of the potential, and third, the atom should have sufficient time to move from the center of the trap before decaying back to the ground state. If all these three criteria are met, one can reduce the energy of the atom per scattered photon. This process can then be optimized by increasing the confinement of the excited state relative to the ground state, as this would make the excited state steeper than the ground state. The selectivity of the laser can be explained by the quantum numbers $m_J = 0$ and $|m_J| = 1$ of the $^1S_0$ and $^3P_1$ states respectively. Using this method repeatedly allows experimentalist to cool below the Doppler limit, creating another limit called the recoil limit. This lower temperature limit is given by

$$k_B T_R = E_k = \frac{h^2}{\lambda^2 M}, \tag{3.4}$$

where M is the atomic mass and λ the cooling wavelength[20]. This limit is calculated given the energy shift the atoms experience when absorbing a single atom. These temperature limits are important for the calculations, since the collision laser also yields photon scattering on the atoms heating up the atoms, which were originally cooled down to the Recoil limit.[30].
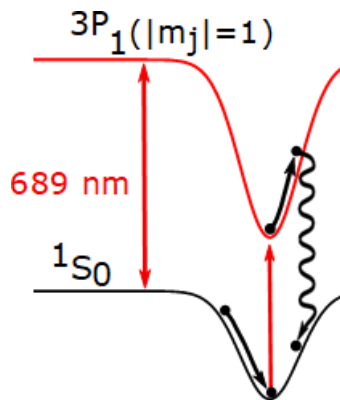
Figure 3.3: Sisyphus cooling using an excitation laser. The energy landscape is created due to the 813.4 nm tweezer laser. As can be seen is the tweezer potential deeper for the excited state ($^3P_1$) compared to the ground state ($^1S_0$). To cool the atom, it should preferably excite near the bottom of the potential, after which it rolls up the steeper excited state before decaying back to the ground state. This will as a consequence lead to a reduction in energy per scattered photon. Figure taken from [11].

3.2.2 Tweezer array

Now the temperature limits are discussed in the previous section we will now take a look at the tweezer array consisting of tweezer traps created by a 813.4 nm laser. These tweezer traps are arranged in an rectangular lattice, which can be either filled or partly filled, as can be seen in figure 3.4. The preparation efficiency, which we try to maximize, can be calculated by dividing the amount of filled traps by the total amount of traps. To simplify the problem, every tweezer trap is considered a distinguishable subsystem, which is easily divisible. This can be done, since the distance between the traps is 8 μm, which is large compared to the effective range of the trap, which is in the order of 1 μm in the ρ direction. It is therefore reasonable to only consider one tweezer trap, as will be explained in this section further on.

Figure 3.4: Filled tweezer array consisting consisting of individual tweezer traps in a rectangular lattice (left). A partly filled tweezer array from which the preparation efficiency can be calculated (right).[11]
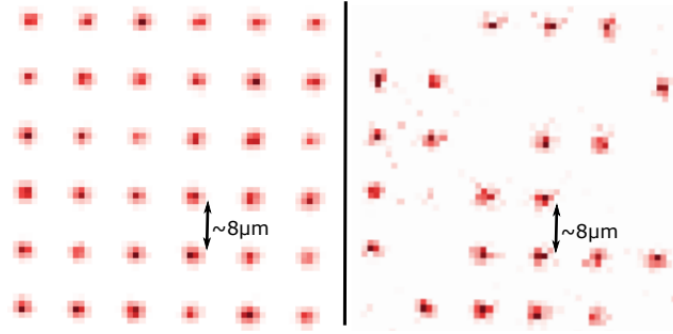
In free space, free from an electric field, atoms in their ground state have no dipole moment. However, when a static electric field is introduced using a laser, it will induce a dipole moment inside the atom to reduce its potential energy. From this we can conclude that the atoms will be attracted to regions with higher intensity therefore minimizing the dipole energy of the atom. This effect is called the differential Stark shift. The differential Stark shift uses, rather than a static field, an oscillating electromagnetic field. Either this frequency is below the atomic resonance frequency, which would make the dipole moment in phase with the electric field and the atoms are drawn to the regions of the highest intensity or the laser frequency can also be too high for the atomic resonant frequency, causing the dipole moment of the atom to be out of phase and to oppose regions of high electric field resulting in the atoms to go down the intensity gradient of the laser[39]. For this Strontium experiment the trapped solution is chosen in which the atom is trapped at high intensities. This intensity profile is a Gaussian intensity profile, causing the atoms to move towards the center [40].

To get an expression for the tweezer trap, an electric field $\vec{E}$ has to be introduced which causes a polarization $\vec{p}$ on the trapped atoms as $\vec{p} = \alpha\vec{E}$, where $\alpha(\omega)$ is the complex polarizability of the atom. In this derivation[20], the polarization has the same frequency ω as the electric field. This gives respectively, in complex notation, $\vec{E}(r,t) = \hat{e}E(r)\exp(-i\omega t) + c \cdot c$ and $\vec{p}(r,t) = \hat{e}p(r)\exp(-i\omega t) + c \cdot c$. Given these expressions, the interaction potential can be defined as

$$U_{\text{dip}} = -\frac{1}{2}\langle\vec{p}\cdot\vec{E}\rangle = -\frac{1}{2\epsilon_0 c}\text{Re}(\alpha)I, \tag{3.5}$$

where I is the intensity of the laser ($I = 2\epsilon_0 c\left|\vec{E}\right|^2$), ϵ_0 is the electric constant and c is the speed of light in a vacuum. The scattering rate in the oscillator Lorentz model is given by

$$\Gamma_{\text{sc}}(\vec{r}) = \frac{P_{\text{abs}}}{\hbar\omega} = \frac{1}{\hbar\epsilon_0 c}\text{Im}(\alpha)I(\vec{r}), \tag{3.6}$$

where P_{abs} is the energy absorbed by the atom per time unit and is re-emitted as dipole radiation as $P_{\text{abs}} = \langle \vec{p} \cdot \vec{E} \rangle = \frac{\omega}{\epsilon_0 c} Im(\alpha)I$ where $\hbar\omega$ is the photon energy. Since all the constants are known and the intensity profile can be chosen, the polarizability should first be calculated using the Lorentz model. The model treats the electron, with mass m and charge e classically and is bounded to the core with an oscillation frequency ω_0, representing the optical transition frequency. In this Lorentz model the equation of motion for the electron is $\ddot{x} + \Gamma_\omega \dot{x} + \omega_0^2 x = -\frac{eE(t)}{m}$. From this differential equation, one can calculate the polarizability to be

$$\alpha = 6\pi\epsilon_0 m c^3 \frac{\Gamma/\omega_0^2}{\omega_0^2 - \omega^2 - i\omega^3/\omega_0^2\Gamma}, \tag{3.7}$$

where Γ is the on-resonant damping rate $\Gamma = (\omega_0/\omega)^2\Gamma_\omega$. This equation can now be inserted into the dipole potential (equation (3.5)) and the scattering rate (equation (3.6)) giving respectively

$$U_{\text{dpp}}(r) = -\frac{3\pi c^2}{2\omega_0^3} \left(\frac{\Gamma}{\omega_0 - \omega} + \frac{\Gamma}{\omega_0 + \omega} \right) I(r) \tag{3.8}$$

$$\Gamma_{\text{sc}}(r) = \frac{3\pi c^2}{2\hbar\omega_0^3} \left(\frac{\omega}{\omega_0} \right)^3 \left(\frac{\Gamma}{\omega_0 - \omega} + \frac{\Gamma}{\omega_0 + \omega} \right)^2 I(r), \tag{3.9}$$

where two terms are within the brackets, which can be reduced to one, considering most laser frequencies are sufficiently close to the transition frequency such that the detuning $\Delta = \omega - \omega_0$ fulfills the inequality $|\Delta| \ll \omega_0$ which makes the first term blow up. This approximation does not always hold up as is also not the case for our setup. However, this does give simplified conclusions, which still hold up by approximation. Filling the detuning into the equation, simplifies the equation for the optical potential and the scattering rate as

$$U_{\text{dpp}}(r) = \frac{3\pi c^2}{2\omega_0^3} \frac{\Gamma}{\Delta} I(r) \tag{3.10}$$

$$\Gamma_{textsc}(r) = \frac{3\pi c^2}{2\hbar\omega_0^3} \left(\frac{\Gamma}{\Delta} \right)^2 I(r). \tag{3.11}$$

From this derivation, two important conclusions can drawn, namely:

- The dipole strength is proportional to Δ^{-1} and the scattering rate is proportional to Δ^{-2}.

- For negative detunings (red) the atoms tend to go towards regions of high field intensity and for positive detunings (blue) the atoms will stay away from regions of high intensity.

In the experiment, a focused beam trap is used. This focused beam provides a three dimensional confinement for the atoms and can be made using only one laser. This laser beam shines a Gaussian intensity profile beam with power P along the z-axis with an intensity profile

$$I(\rho, z) = \frac{2P}{\pi w^2(z)} \exp\left(-2\frac{\rho^2}{w^2(z)} \right), \tag{3.12}$$

where ρ is the radial coordinate and $w(z)$ is the beam waist defined as $1/e^2$ of the maximum intensity. This beam waist is equal to w_0 at $z = 0$ but diverges as it moves away from the origin along the z-axis as

$$w(z) = w_0 \sqrt{1 + \left(\frac{z}{z_R} \right)^2}. \tag{3.13}$$

Here z_R is the Rayleigh length, which depends on the wavelength of the trapping laser as $z_R = \pi w_0^2/\lambda$[20]. This intensity profile (3.12), will later be used in the simulation. As now both the internal structure, the temperature limits and the the tweezer array are explained it will be important to model this into the simulation. This will be done in the following chapter, where the simulation is explained.

Part II

Simulation

Chapter 4

Simulation outline

In this simulation outline I will explain how the simulation works and what assumptions are made. In section 4.1, I introduce the hypothesis, the initialisation and the time iteration loop. Then in section 4.2 I will explain the dipole trap, the differential Stark shift and how it is implemented into the simulation. This section concludes by explaining the relative detuning and its effect on the spontaneous emission processes. In section 4.3, the forces are explained and in section 4.3.2 the resulting changes in energy will be explained.

4.1 Hypothesis, initialisation and time iteration loop

We will start the simulation outline with the hypothesis and a discussion of the initialisation and the time iteration. The hypothesis will try to predict some results based on the theory explained earlier. The initialisation part will show how the particles are set up and what assumptions are made in the beginning of the simulation and the time iteration loop part will explain how the time iteration takes place and what variables are calculated per time iteration.

4.1.1 Hypothesis

The goal of the simulation of this thesis, is to know what the energy gain as a function of the detuning is, also known as the trap loss profile $A'_N(\Delta)$, as was introduced in section 2.3. This can be done by changing the detuning for discrete values and by looking at the energy gain per unit time. This trap loss profile, combined with the wave function overlap and the Bose-Einstein distribution function following (2.13) then gives the trap loss profile as a function of the detuning[19]. This detuning of the collision laser relative to the transition frequency between the $^1S_0$ and $^3P_1$ state is hypothesized to be small compared to the depth of the tweezer trap, since this would give the highest scattering rate, but not too small, since having a low detuning also means there is little to no energy gain from the scattering processes, as explained in section 2.2. To distinguish between two-body and one-body losses, the simulations can be of importance, since the overlap calculations can only predict the trap loss. In this simulation the trap loss is expected to have a good ratio of one-body over two-body losses for low detunings, meaning in the order of the trap depth 2.3 MHz as we will see in section 3.2.2, as this would induce just enough energy per scattering event to exploit the variance in energy prior to any scattering process.
Another experimental variable of importance in the simulation, is the effect of the Rabi frequency. This Rabi frequency will have a huge influence on the amplitude of the Rabi oscillation, defined as $\frac{\Omega^2}{\Omega^2+\Delta^2}$ (A.82). Beforehand, a low Rabi frequency is expected to be better, since this would decrease the amplitude of the Rabi oscillation according to equation (A.83). This low amplitude would ensure most colliding atoms are in the S state most of the time prior to the collision, recreating the semiclassical picture of light induced collisions. However, a small Rabi frequency, might not be the most ideal scenario as it might not excite colliding atoms at all. For a large

Rabi frequency, this excitation would happen during the collision, but this excitation might also happen outside of the scattering processes due to linewidth broadening, as we saw in equation (2.49), creating too many spontaneous emission processes causing unwanted heating.

Finally, the cooling mechanism can be of importance, since it can bring down the average energy while maintaining the variance in the energy and thus in the different energies between particles prior to the collision as described in the statistical discussion in section 2.2. All these factors described above are dependent on each other, which makes it hard to find an analytical solution, and makes the use of a simulation required. In the next sections, the simulation will be outlined on how it works. The code itself is listed in section B.5.

4.1.2 Initialisation

The simulation starts by defining time in the usual way from $t = 0$ to t_{end}. Here a t_{end} is chosen to be a thousand times the lifetime of the $^3P_1$ state in order to eliminate too much fluctuations of the emission processes while also keeping the computational time of the simulation low enough. Then a time spacing has been chosen, typically in the order of $\sim 10 \times 10^{-8}$ s such that it is of the same order as the space divided by the velocity such that particles properly feel each other and have time to smoothly accelerate.

After the time is set up, we set the number of particles, N, in a 6-dimensional phase space of size N by 6, where the first three dimensions represent the position components and the remaining three dimensions represent the momentum components. The position initialisation for the particles are chosen randomly, since we found it did not have much influence on the simulation for later timescales, the distribution of the particles are therefore chosen out of a Gaussian probability distribution with σ one tenth the width of the smallest confinement[41], which is $0.1 \,\mu$m. This will become clear in section 4.2.1. A Gaussian curve is mathematically allowed since the movements of the particles behave as Brownian motion.

The velocity set up is somewhat more difficult, since it has to obey the Maxwell-Boltzmann velocity (V_{dist}) distribution for a temperature of $1 \,\mu$K [42]. This can be done statistically using a rejection method; [43]. Explained shortly, random values will be chosen in the plane set by

$$\text{ylim} = [0, \max(V_{\text{dist}})] \quad \text{and} \quad \text{xlim} = [a, b], \tag{4.1}$$

where a and b should be chosen sufficiently to the left and right respectively such that the Boltzmann curve is clearly visibly in this range. The random values in this plane will be accepted if it lies below the Boltzmann curve and will be rejected if the random numbers are outside the Boltzman curve. The accepted values are then assigned to the particles' momenta in this phase space, keeping in mind that the Boltzmann curve represents the total velocity magnitude whereas we are only interested in the three spatial components separately one should divide the total magnitude by $\sqrt{3}$. This has been done using the code given in code B.4.

The third variable which has to be initialised is the internal quantum state. The initial state of the particles should lie on the Bloch sphere as this would correctly represent a two-level system [44]. To have the particles somewhere on the Bloch sphere, the coefficients c_g and c_e are given by

$$c_g(\theta) = \cos(\theta/2) \tag{4.2}$$

$$c_e(\theta, \phi) = e^{i\phi} \cdot \sin(\theta/2), \tag{4.3}$$

where $\phi = [0, 2\pi]$ represents the azimuthal angle and $\Theta = [0, \pi]$ represents the polar angle on the Bloch sphere. In the simulation, $\Theta = 0.01$ rad is chosen, since most particles are far away from each other, meaning that they are most likely in the ground state for a large detuning.

4.1.3 Time iteration

After the initialisation, the simulation starts to run in a *for-loop*. The simulation uses a leap frog iteration scheme [45], which operates according to

$$v_{i+1/2} = v_i + a_i \frac{\Delta t}{2}$$
$$x_{i+1} = x_i + v_{i+1/2}\Delta t$$
$$v_{i+1} = v_{i+1/2} + a_{i+1}\frac{\Delta t}{2} + v_{\text{sp. em.}},$$

where before the third step, the acceleration a_{i+1} has been calculated from the forces, as will be explained in section 4.3.1. Also, the momentum kick $v_{\text{sp. em.}}$ caused by spontaneous emission is calculated before the third step, since this induces an extra term to the original velocity. After the leap frog scheme, the effective detunings and the effective decay rates are calculated, as we will see in section 4.2.1 and 4.2.2 respectively, and the time gets updated at the end of the loop. First there is a check whether or not the particles have left the trap. This is done for threshold values of $\rho > 1\,\mu\text{m}$ or $z > 10\,\mu\text{m}$, where ρ and z represents the radial distance to the z-axis and the height in a cylindrical coordinate system respectively. Using these thresholds, one can identify the particles which left the trap.

Then the kinetic, potential and interaction energy are calculated, in order to calculate the effective detuning, which will be explained further in section 4.2.1. This effective detuning is necessary to update the internal state of all the individual particles and is done directly after calculating the interaction energies. Since these quantum states are of much smaller timescales than the timescales of the particle movements, new sub-iterations are done per normal time iteration to update the internal state of the particles fast enough. To finish the iteration loop, the decay rate has to be calculated, which will be explained in section 4.2.2.

4.2 Dynamic quantum states

Now that the initialisation of the simulation is explained, a better description of the quantum states is needed as will be done in this section, the quantum states of the particles depend on the tweezer trap creating a differential Stark shift, the detuning set by the laser and the Rabi frequency as will all be treated in this section. To do this, the concepts of the effective detuning and the effective decay rate will be introduced.

4.2.1 Effect of the tweezer trap

In this section, the implementation and the applications of the tweezer trap will be explained. This explanation will be done for the different internal quantum states with their respective polarizabilities. This difference in polarizability creates a differential Stark shift, which has an effect on the detuning. To account for the different detuning felt by the particles a concept of the *effective detuning* will be explained in this section.

Tweezer trap

When simulating a physical system, the first thing to consider is the background of the simulation, the stage where the particles will eventually interact with each other. The physical background is defined by the MOT and the tweezer traps. However, not every term is as important. The first thing we can neglect is the MOT as the forces it asserts on the particles during light-assisted collisions are small compared to the forces of the tweezer trap[11]. Also, since the tweezer trap consists of an array of lasers which individually create a local minimum in the potential landscape, it is possible to reduce the problem to a single laser trap[11]. With all these approximations, the

background of the physical stage are given by a single tweezer trap.

This trap can then be described in mathematical terms to extract the forces from it. First the intensity of the light as a function of space is given by equation (3.12) as [26]

$$I_{\text{Gaussian}}(\rho, P, w_0) = \frac{2P}{\pi w_0^2} \exp\left(-\frac{2\rho^2}{w_0^2}\right). \tag{4.4}$$

The resulting potentials, caused by the differential Stark shift, are given in the ρ-direction as

$$U_\rho(\rho, P, w_0) \propto -\eta_0 \alpha I_{\text{Gaussian}}(\rho, P, w_0), \tag{4.5}$$

and in the z-direction as

$$U_z(z, P, w_0) \propto -\eta_0 \alpha \frac{2P}{\pi \beta w_0^2} + mgz, \tag{4.6}$$

Where the constant β is given by $\beta = 1 + \left(\frac{\lambda z}{\pi w_0^2}\right)^2$ and where the gravitation is in the z-direction. The waist w_0 is given in equation (3.13). In both the expressions, the conversion factor is left out in the thesis, since only the shape is important to understand the underlying physics. To calculate the depth of the tweezer trap, one uses a polarization α of $286 \, \text{Cm}^2\text{V}^{-1}$ for the $^1S_0$ state and $353.9 \, \text{Cm}^2\text{V}^{-1}$ for the $^3P_1 \, |m_j| = 1$ state, which corresponds to the polarizabilities at 813nm (the magic wavelength of the $^1S_0$ and $^3P_0$ state)[30]. The profile of the tweezer trap can be seen in figure 4.1. Here, a minimum trap depth of $120 \, \mu\text{K}$ can be seen for the $^1S_0$ state and a minimum trap depth of $159 \, \mu\text{K}$ for the $^3P_1$ state. This corresponds to a trap depth of $16.8 \, \text{Mrad/s}$ and $20.7 \, \text{Mrad/s}$ respectively or $2.6 \, \text{MHz}$ and $3.3 \, \text{MHz}$. From these values the differential Stark shift magnitude can easily be calculated, as has also been done in figure 4.1 in the last row. Note that the scaling between the ρ- and z-direction is different. Where the effective range in the ρ direction is approximately $1 \, \mu\text{m}$, the effective range in the z-direction is approximately $10 \, \mu\text{m}$ long. This will as a consequence lead to more diffusion along the z-direction as the ρ-direction is more confined.
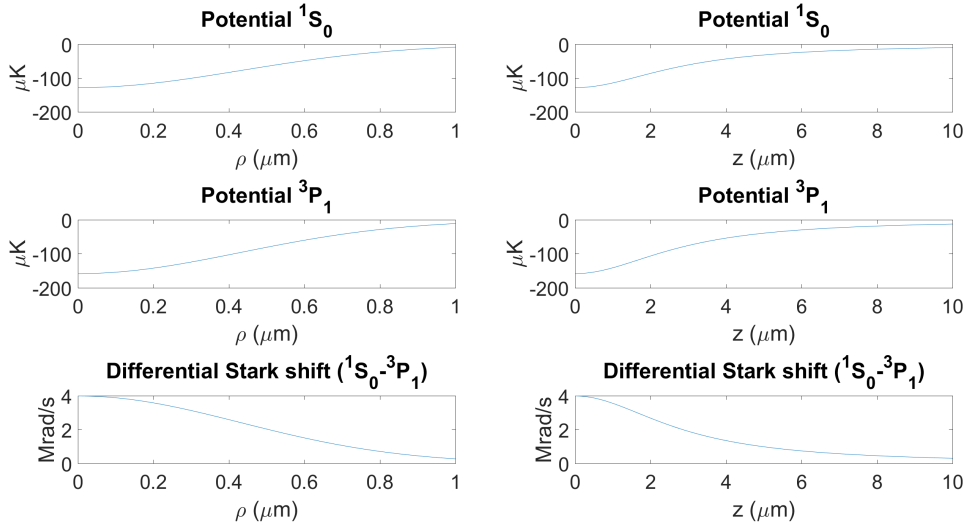
Figure 4.1: Trap depth in both the radial direction (left column) and along the z-axis (right column) for the $^1S_0$ (first row) and $^3P_1$ states (middle row) and the resulting differential Stark shift between the states (last row).

Effective detuning

Now that the background of the simulation has been explained, it is important to see what effect it has on the internal state of the particles. To do this, this thesis defines the effective detuning as

the detuning in the frame of reference of the particles. Since the particles are constantly moving inside the trap, all the particles experience different detunings because of the position dependent differential Stark shift as it depends on the laser profile (3.12).

Another effect on the effective detuning is the Doppler shift, but that turned out not to be relevant. The Doppler shift for a given source frequency Ω_s , in this case of the collision laser, determines the observed frequency in the frame of reference of the observer Ω_0, in this case of the particles and is given by[46]

$$\Omega_0(v) = \sqrt{\frac{1-v}{1+v}}\Omega_s, \tag{4.7}$$

where v is the relative velocity between the source and the individual particles. Since the laser is standing still, this would simply imply that v is the parallel velocity component of the particles relative to the collision laser. Filling in a relatively high velocity at $T = 1\,\mu K$ of $0.01\,\text{m/s}$ gives a change in measured frequency of just 2%. This small change for high velocities will therefore be neglected, resulting in no Doppler shift in the simulation.

The starting point for the effective detuning is the fixed detuning by the laser, which is defined as $\Delta = \omega_l - \omega_0$, the difference between the laser light and the transition frequency of the ground and excited state of the atom. Furthermore, the differential Stark shift will increase the effective detuning with values of $4\,\text{Mrad/s}$ or more, since the polarizability of the P state is bigger than the polarizability of the S state, resulting in the inequality $0 \leq E_{^1S_0} - E_{^3P_1} \leq 4\,\text{Mrad/s}$, as can also be seen in figure 4.1. This effect gives the following formula for the effective detuning as

$$\Delta' = \Delta + \Delta E_{\text{dSs}}, \tag{4.8}$$

where Δ is the detuning set by the laser and E_{dSs} is the energy shift caused by the differential Stark shift. However, at the center of the trap, a maximum differential Stark shift of $4\,\text{Mrad/s}$ is felt on the effective detuning. Therefore, it does not make sense to consider detunings Δ higher than $4\,\text{Mrad/s}$ below the potential barrier of the excited repulsive $1u$ state, which has been introduced in figure 3.1, since this would allow the incoming scattering wave function to enter the short-range interaction making the approximations, of not entering the inner regime as explained in 3.1, not valid anymore.

To get an estimation of the detuning, it should approximately be $V_{\text{trap depth}} \leq \Delta \leq 2V_{\text{trap depth}}$, since the focus of this paper is one-body losses and not two-body losses. If one would translate this to the specific trap depths of the S potential it can be found that the detuning should be $V_{^1S_0} \leq \Delta \leq 2V_{^1S_0}$. Here the $^1S_0$ potential is taken, since it is the lowest potential and therefore the easiest to escape. Also, in case an excited particle tends to leave the trap, it may emit a photon within a small time scale compared to the time it will lose energy, resulting the atom to be found in the ground state again therefore still leaving the trap in the $^1S_0$ potential. In numbers, this inequality above would translate to $16.8\,\text{Mrad/s} \leq \Delta \leq 33.6\,\text{Mrad/s}$ or $2.7\,\text{MHz} \leq \delta \leq 5.3\,\text{MHz}$. In the rest of the thesis I will refer to the detuning as δ as the units will be given in MHz.

Also during the simulation, the particles will feel the interaction energy contributing to the effective detuning. This is ultimately the reason why colliding particles become resonant with each other and excite and why the effective detuning in equation (4.8) can become zero. Classically and without the differential Stark shift, this would happen at the Condon point, see section 2.1. In the simulation it is a bit more complex as the differential Stark shift is involved. Also, the excitations do not specifically have to happen at the Condon point, it can also excite close to the Condon point, since also with a detuning, Rabi oscillations take place as we saw in section 2.5.1.

4.2.2 Quantum states

Now the tweezer trap and its effect on the detuning have been explained, it is of interest how the particles responds to this as a consequence. This will be done by discussing the order of Rabi frequency, the resulting Rabi oscillations and a method to implement spontaneous emission to the Rabi oscillations.

Rabi frequency

To talk about the Rabi frequency, it is useful to first get the order of magnitude right. To check this, the equation of the Rabi frequency $\Omega = \vec{d} \cdot \vec{E}/\hbar$ where d is the electric dipole moment can be used. The total Rabi frequency can also be rewritten as[47]

$$\Omega = \sqrt{\frac{4P}{\epsilon_0 c_0^2}} \frac{\langle n, l, j, m_j | \, r_q \, | n', l', j', m_j' \rangle}{\hbar}, \tag{4.9}$$

where the relation of a Gaussian intensity beam with a width w_0 and power P have been used[27]. This power is connected to the electric field intensity as

$$\frac{2P}{\pi w_o^2} = \frac{1}{2} c \epsilon_0 \left| \vec{E} \right|^2. \tag{4.10}$$

Filling in these values in the *alkali-Rydberg calculator* (ARC), see code B.1, with the correct quantum numbers $\langle n, l, j, m_j | = \langle 5, 0, 0, 0 |$ and $\left| n', l', j', m_j' \right\rangle = | 5, 1, 1, 1 \rangle$ for the S and P states respectively, gives a Rabi frequency of 54.61 MHz, which is calculated using a waist of 50 μm and a laser power of 20 μW. This Rabi frequency is, however, in the highly saturated regime, see 2.5.2. It is therefore also interesting to consider lower Rabi frequencies, as will be done in the results. The power can be changed by orders of magnitude leading to huge variations in the Rabi frequency.

Rabi oscillation

To use Rabi oscillation, explained in section 2.5.1, in the simulation, a finite difference method has been used. To show how this works, let's consider the following quantum system wave function $|\Psi\rangle$

$$|\Psi\rangle = c_1 |\Psi_g\rangle + c_2 |\Psi_e\rangle, \tag{4.11}$$

where c_1 and c_2 represent the coefficients for the particle to be found in the ground state ($|\Psi_g\rangle$) or in the excited state ($|\Psi_e\rangle$) respectively if multiplied with its complex conjugate. These coefficients will evolve under a detuned laser light as (equation (2.44))

$$\dot{c_1} = i \frac{\Omega}{2} e^{i\delta t} c_2, \tag{4.12}$$

$$\dot{c_2} = i \frac{\Omega}{2} e^{-i\delta t} c_1. \tag{4.13}$$

To iterate this in the simulation, the forward Euler, the backward Euler and the semi explicit Euler scheme have been tried. Of those three, the semi explicit Euler was the most stable of the three. Using the semi explicit Euler scheme, where the first equation is iterated forwards and the other is iterated backwards, these equations would then become [48]

$$\frac{c_1(t_{i+1}) - c_1(t_i)}{dt} = -i \frac{\Omega}{2} e^{i\delta t} c_2(t_i), \tag{4.14}$$

$$\frac{c_2(t_{i+1}) - c_2(t_i)}{dt} = -i \frac{\Omega}{2} e^{-i\delta(t+dt)} c_1(t_{i+1}). \tag{4.15}$$

Rewriting this as a function of $c_1(t_{i+1})$ and $c_2(t_{i+1})$ would ultimately result in equations

$$c_1(t_{i+1}) = -i \frac{\Omega}{2} e^{i\delta t} c_2(t_i)(dt) + c_1(t_i), \tag{4.16}$$

$$c_2(t_{i+1}) = -i \frac{\Omega}{2} e^{-i\delta(t+dt)} c_1(t_{i+1})(dt) + c_2(t_i), \tag{4.17}$$

which are the equations to calculate c_1 and c_2 for the next time step $t + dt$. These formulas are dependent on the time step dt, the detuning δ and the Rabi frequency Ω.

In figure 4.2 different Rabi oscillations of $\Omega = 54\,\text{MHz}$. In this figure, three distinctions have been made between different detunings. From the top to the bottom, detunings of $\delta = 0\,\text{MHz}$, $54\,\text{MHz}$, $540\,\text{MHz}$ have been used. The blue line is the probability of being in the excited state whereas the red line is the probability of being in the ground state. The probability of being in either in the ground or excited state stays one as probabilities should always add up to one. Also, the amplitude of the oscillations, explained in section 2.5.1, can be seen and how it changes with different detunings. The higher the detuning the lower the oscillations amplitude, ultimately not affecting the quantum states in the limit for $\delta \rightarrow \infty$. This can also be seen in equation (A.82). These plots have been made using code B.2 using the Runge Kutta method[49].
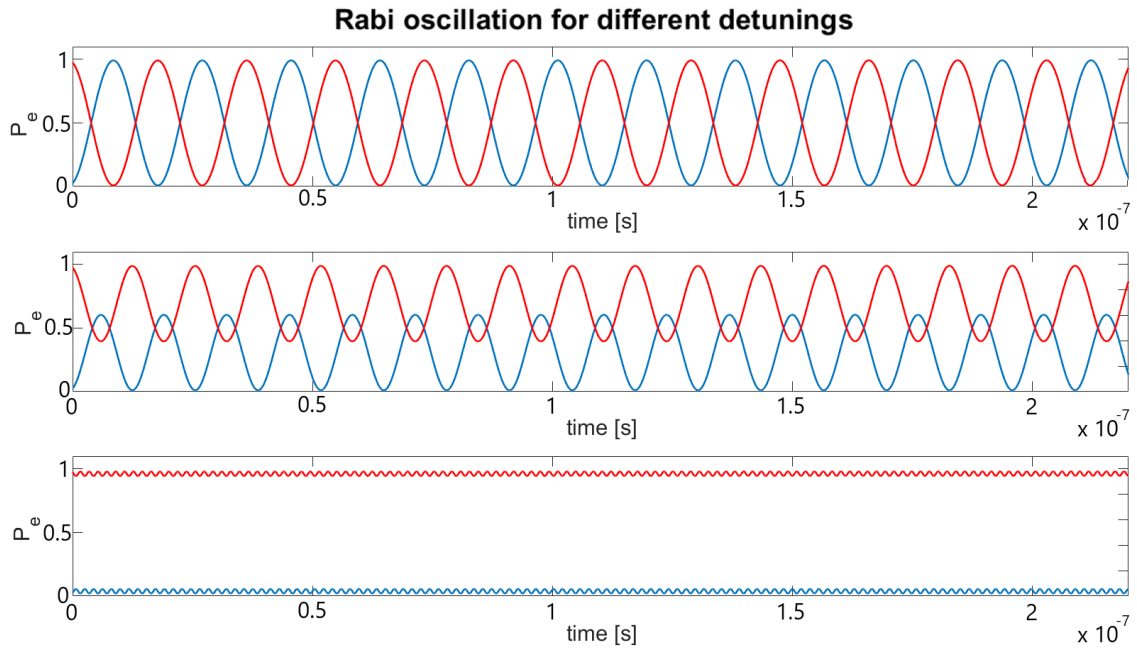
Figure 4.2: Rabi Oscillations for $\Omega = 54\,\text{MHz}$ with $\delta = 0\,\text{MHz}, 54\,\text{MHz}, 540\,\text{MHz}$. Here the blue line is the probability of measuring the particle in the excited state $|c_e|^2$ and the red line is the probability of measuring the particle in the ground state $|c_g|^2$. The higher the detuning the lower the oscillation amplitude.

In figure 4.3 the Rabi oscillation are shown as used in the simulation. here, only the probability of being in the excited state has been plotted to make the figure more clear. The plot has been made for 10 individual particles with zero detuning, resulting in maximum Rabi oscillations between 0 and 1. The main difference between figure 4.2 and 4.3 is the higher Rabi frequency used, which was too fast to be stable in the iteration loop as used in figure 4.2. To solve this, the use of sub-time steps within each normal time iteration was required, which divides each time step in smaller time steps using another for-loop.
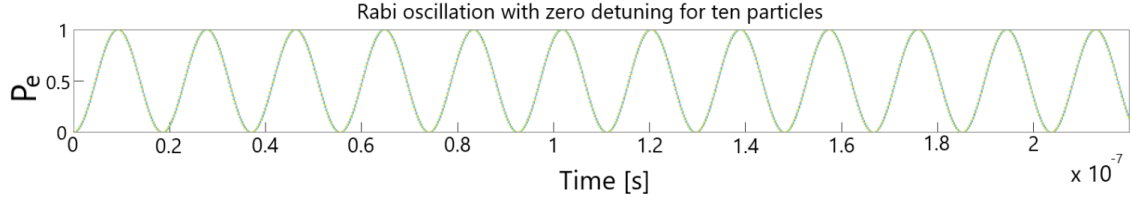
Figure 4.3: Rabi Oscillations for N=10 all in the ground state with zero detuning. The Rabi frequency is here in the order of 300 MHz

Optical Bloch equations and spontaneous emission

Now, we have seen that the normal Rabi oscillations are correctly implemented into the code, it is useful to look at solutions of the optical Bloch equations, since we know that the Rabi oscillation framework does not include spontaneous emission, since there is no coupling to the vacuum field. The Optical Bloch Equations are [23]

$$\frac{\mathrm{d}\rho_{gg}}{\mathrm{d}t} = +\gamma\rho_{ee} + \frac{i}{2}\left(\Omega^*\tilde{\rho}_{eg} - \Omega\tilde{\rho}_{ge}\right) \tag{4.18}$$

$$\frac{\mathrm{d}\rho_{ee}}{\mathrm{d}t} = -\gamma\rho_{ee} + \frac{i}{2}\left(\Omega\tilde{\rho}_{ge} - \Omega^*\tilde{\rho}_{eg}\right) \tag{4.19}$$

$$\frac{\mathrm{d}\tilde{\rho}_{ge}}{\mathrm{d}t} = -\left(\frac{\gamma}{2} + i\delta\right)\tilde{\rho}_{ge} + \frac{i}{2}\Omega^*\left(\rho_{ee} - \rho_{gg}\right) \tag{4.20}$$

$$\frac{\mathrm{d}\tilde{\rho}_{eg}}{\mathrm{d}t} = -\left(\frac{\gamma}{2} - i\delta\right)\tilde{\rho}_{eg} + \frac{i}{2}\Omega\left(\rho_{gg} - \rho_{ee}\right), \tag{4.21}$$

where ρ_{gg}, ρ_{ge}, ρ_{eg} and ρ_{ee} represent the density matrix elements, γ is the linewidth of the transition and Ω^* is the generalised Rabi frequency. In figures 4.4a and 4.4b, the solutions of these equations can be seen for $\gamma = 1/\tau$. The code uses another convention for the linewidth, namely $\gamma_{OBE} = 2 \cdot \gamma_{code}$ as the linewidth was only taken from the center. This resulted in that fact that the γ in the code had to be calculated using the relation $\gamma_{code} = 1/(2\tau)$, where $\tau = 21.5\,\mu s$ is the lifetime of the excited $^3P_1$ strontium-88 state.

The two figures below are shown to visualize the full quantum dynamic picture for both a Rabi frequency of zero and for a Rabi frequency of 2π MHz, plotted against the time from zero to the lifetime τ. And indeed, as should always be the case for zero Rabi frequency, the probability of the ρ_{ee} dropped off with a factor of $\frac{1}{e} \approx 0.367$ within the lifetime. This result is clearly visible for the $\Omega = 0$ case in the left figure. For $\Omega \neq 0$ in the right picture, it is slightly more complicated, since now mixed states are introduced causing decoherence in the system into these mixed states. For this the solutions of the OBE from section A.8.4 can be taken in the steady case as this is the solution for $t \to \infty$. Here the value of the population difference w (equation (A.94)) is somewhere between 0 and 0.5, depending on the saturation parameter and thus the intensity of the laser.
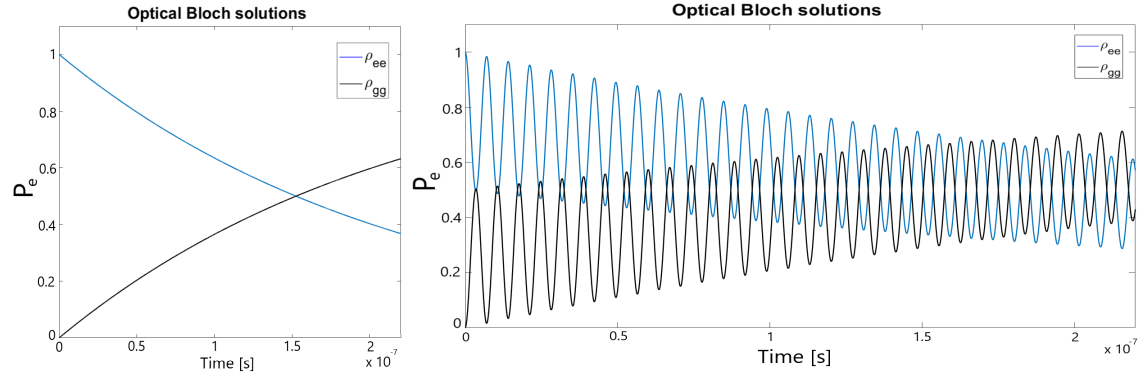
(a) Optical Bloch plot for $\Omega = 0$. A clear drop of the excited wave function can be seen by a factor of $1/e$ at the lifetime of $21.5\,\mu s$.

(b) Optical Bloch plot for $\Omega = 1\,\mathrm{MHz}$ and $\delta = 0.5\,\mathrm{MHz}$.

Figure 4.4: Solutions of the OBE where the blue line represents the ρ_{ee} state of the density matrix and the black line shows the ρ_{gg} state of the density matrix. Only the on-diagonal elements of the wave function density matrix are visualized. (Left) No Rabi frequency, here only the exponential decay can be seen. (Right) A Rabi frequency of $\Omega = 1\,\mathrm{MHz}$ causing the states to oscillate and to decay at the same time, while also having decoherence into the mixed off-diagonal states.

To implement spontaneous emission into the code, it was of no advantage to implement the Optical Bloch Equations, since these continuous oscillations could never produce a discrete decay into the ground state, ultimately emitting a photon with discrete energies.

Therefore, another approach was found in which the decay curve is calculated independently from the Rabi oscillations, keeping track of the chance of decaying. Let's first look how an ensemble of particles starting in the excited state would decay. Here the convention $\Gamma = 1/\tau$ is used. The rate equation for spontaneous emission is given as[21]

$$\frac{dN_e(t)}{dt} = -\Gamma \cdot N_e(t). \tag{4.22}$$

In a discrete semi-explicit scheme this will become

$$\frac{N_e(t_{i+1}) - N_e(t_i)}{dt} = -\Gamma \cdot N_e(t_{i+1}), \tag{4.23}$$

which would lead to an expression for the next time step as

$$N_e(t_{i+1}) = \frac{N(t_i)}{1 + \Gamma \cdot dt}, \tag{4.24}$$

from which a decay loss per time step $dN_e(t_i)$ defined as

$$dN_e(t_i) = N_e(t_{i-1}) - N_e(t_i). \tag{4.25}$$

However, during the simulation, the particles are not always in the excited state. Most of the time they are in the ground state, which would mean there is no chance of decaying. Therefore, when implementing this framework into the iteration scheme we choose an effective decay rate that is defined as $\tilde{\Gamma} \equiv \Gamma \cdot |c_e|^2$. This simply means that the decay rate scales with the probability of being in the excited state. This can also be seen from Fermi's golden rule, which states that the decay rate from an initial to a final state is given by[50]

$$\Gamma_{e \to g} = \frac{2\pi}{\hbar} |\langle g| H |e\rangle|^2 \rho(E_f). \tag{4.26}$$

Where the Hamiltonian consists of the dipole operator and the ρ is the density of states at the Fermi level. Let's for example take the superposition state $|\Psi\rangle = c_g |g\rangle + c_e |e\rangle$, substituting this superposition state into Fermi's golden rule yields

$$\Gamma_{i\rightarrow f} = \frac{2\pi}{\hbar} |\langle g| H |(c_g |g\rangle + c_e |e\rangle)\rangle|^2 \rho(E_f) \tag{4.27}$$

$$= \frac{2\pi\rho(E_f)}{\hbar} (|c_g|^2 \langle g| H |g\rangle + |c_e|^2 \langle g| H |e\rangle). \tag{4.28}$$

Here $\langle g| H |g\rangle = 0$, since the dipole operator changes the quantum number causing the inner product to be orthogonal. Which leaves the equation left as

$$\tilde{\Gamma}_{i\rightarrow f} = \frac{2\pi}{\hbar} |c_e|^2 \langle g| H |e\rangle = |c_e|^2 \Gamma_{i\rightarrow f}, \tag{4.29}$$

supporting the claim earlier for an effective decay rate, since it depend on the state of the particle. Also, since every particle experiences another detuning, it is not useful anymore to talk about an ensemble rather than a probability of decaying for a single particle. Vice versa, this step would seem quite obvious because if every particle would individually obey a probability distribution of a decay plot this would transform to the famous decay plot as in figure 4.4a.
Implementing both the effective decay rate as going to a probability transforms equation (4.24) into

$$P_{\text{decay}}(t_{i+1}) = \frac{P(t_i)}{1 + \Gamma |c_e|^2 dt}, \tag{4.30}$$

and a probabilistic loss per time step as

$$P_{\text{decay}}(t_i) = P_{\text{decay}}(t_{i-1}) - P_{\text{decay}}(t_i). \tag{4.31}$$

The probabilistic decay equation could now be implemented into the code resulting in individual decay rates for each particle and has also been plotted in figure 4.5. For this plot every particle starts off in the excited state and stays in the excited state to show the individual decay curves. After some time, some particles have decayed and start again at the bottom. Notice that the slope of the decay curve is of most importance, since this determines the chance of decaying, see equation (4.31).
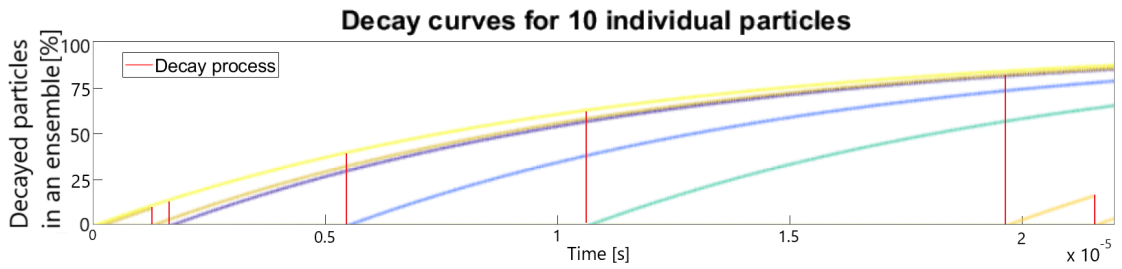
Figure 4.5: Decay curve for 10 particles, which are always in the excited state, meaning that the decay curve has a constant decay coefficient. Every particles has its own decay curve, given by a single color, following the ensemble decay rate. The rate of decay of the imaginary ensemble determines the probability of decaying back to the ground state for a single particle. During the 22 µs of the plot six decay events took place. Namely the orange particle, given by the orange line, at $t = 2\,\mu s$, $t = 20\,\mu s$ and $t = 21\,\mu s$. The purple particle also at $t = 2\,\mu s$. The blue particle at $t = 5\,\mu s$ and the green particle at $t = 11\,\mu s$, which are visualized in red.

Using the effective decay rate gives the correct decay curve for particles in the excited state, as can have been seen in figure 4.5. Particles in the ground state should have a flat decay curve, following equation (4.30), and particles in a superposition state should follows a decay curve between these

two extremes. This effective decay rate gives the right amount of decay events during the time given the lifetime of strontium-88. This has all been done without implementing the density matrix formalism, which makes it computationally more feasible as only c_1 and c_2 now have to be computed.

Up until now we discussed the effective detuning due to the tweezer trap and how to implement spontaneous decay using the effective decay rate, now the energy is of importance as will be done in the next section.

4.3 Equations of motion and energy

Now that the initialisation and the internal quantum states are explained one can look at the dynamics of the particles and the energies. First, all the forces will be explained together with spontaneous emission momenta kicks, later the energies will be explained. These represent the interaction energy, the potential energy, the kinetic energy and other concepts such as the differential Stark shift and temperature.

4.3.1 Equation of motion

The dynamics of the particles are handled by the equations of motions, originated from the forces at play. This includes the interaction forces, the trap forces and other events such as spontaneous emission as will be discussed in this section. The forces are also a consequence of the internal state, which is explained above.

Interaction force

The interaction forces causes the effective detuning to become resonant with the collision laser causing particle to excite to the excited state. This will add energy into the system because of the movement in the $U_{1u}(r)$ excited interaction potential. This happens if one particle in the $^1S_0$ state and another in the $^3P_1$. This potential is given as[34]

$$U_{1u}(R) = C_3/R^3 \quad \text{where} \quad C_3 = 0.0075\, E_{\mathrm{h}} a_0{}^3. \tag{4.32}$$

Here, R is again the internuclear distance and can be calculated as

$$R^2 = dx^2 + dy^2 + dz^2, \tag{4.33}$$

dx, dy and dz represent the distance between the particles in the $x-$, $y-$ and z-direction. The internuclear distance is a square matrix of size N, representing the distance between all the particles.

To calculate the force due to the interaction potential one should remember that the derivative of the potential is minus the force. This will result in

$$\vec{F}(R) = -\frac{dU_{1u}(R)}{dR} = -0.0225\, E_{\mathrm{h}} a_0{}^3 \vec{R}/R^4. \tag{4.34}$$

Doing this for all three directions in Cartesian coordinates yields

$$F_x(x,y,z) = -\frac{\partial U_{1u}(R)}{\partial x} = -\frac{\partial U_{1u}(R)}{\partial R}\frac{\partial R}{\partial x} = -0.0225\, E_{\mathrm{h}} a_0{}^3 \cdot \frac{dx}{R^4}, \tag{4.35}$$

$$F_y(x,y,z) = -\frac{\partial U_{1u}(R)}{\partial y} = -\frac{\partial U_{1u}(R)}{\partial R}\frac{\partial R}{\partial y} = -0.0225\, E_{\mathrm{h}} a_0{}^3 \cdot \frac{dy}{R^4}, \tag{4.36}$$

$$F_z(x,y,z) = -\frac{\partial U_{1u}(R)}{\partial z} = -\frac{\partial U_{1u}(R)}{\partial R}\frac{\partial R}{\partial z} = -0.0225\, E_{\mathrm{h}} a_0{}^3 \cdot \frac{dz}{R^4}, \tag{4.37}$$

where the chain rule was used to differentiate to the respective Cartesian coordinate. Notice how all these three force matrices are anti-symmetric since the dx, dy and dz-matrices were also anti-symmetric. This should be correct, since both particles feel each other with the same strength but with opposite sign.

But remember not all the particles interact at the same time, only when one is in the excited P state and the other particle in the ground S state. To take this into account, all the forces F_{ij} get multiplied with a factor SP_{ij} which is defined as element in the ith column and jth row of matrix

$$\vec{SP} = \vec{PS} = \vec{c}_g \vec{c^*}_g \otimes \vec{c}_e \vec{c^*}_e + \vec{c}_e \vec{c^*}_e \otimes \vec{c}_g \vec{c^*}_g, \tag{4.38}$$

where $\vec{c}_e$ and $\vec{c}_g$ represent the coefficients of the ground ($|\Psi_g\rangle$) and excited state ($|\Psi_e\rangle$) for every particle. This SP matrix represent the interaction strength between the particles, since the particles only feel each other when one is in the ground state and the other is in the excited state, or vise versa. These two options give the two terms in equation (4.38). Notice how the outer product creates a matrix and since this equation is written as $AB' + A'B$, this expression is a symmetric matrix, this makes sense, since both particles feel each other with the same strength. To make this matrix even better one should get rid of all the diagonal elements of the matrix, since a particle does not feel an interaction force with itself.

Finally, when the elements from equation (4.35) and (4.38), representing the force matrix and the interaction strength matrix, are multiplied, the real force is calculated. To calculate the force of one particle, the contributions of all other particles should be summed. Most of these interaction terms will however be almost equal to zero due to the distance between them. This indicates why three-body scattering rarely happens, confirming the scattering formalism used in section 6.1.1.

Trap forces

Another force at play is the force from the tweezer trap which keeps the particles together and make the particles oscillate inside the trap if there weren't any other forces at play. To calculate the trap forces, which depend on the internal state of the particle, it is first useful to consider the extremes of the problem: One in which a particle is fully in the $^1S_0$ state and one where a particle is fully in the $^3P_1$ state. They would feel another potential and therefore another force. Also a distinction between the ρ-direction and the z-direction has to be made, since the profiles of these traps differ in each direction. We use cylindrical coordinates with $\rho = x^2 + y^2$. The potentials are already given in equations (4.5) and (4.6) and the corresponding force for a particle in the $^1S_0$ and $^3P_1$ state can be calculated as

$$\vec{F}_{\rho,^1S_0}(\rho, z) = -(U_\rho(\rho + h, z) - U_\rho(\rho, z))/h, \tag{4.39}$$

$$\vec{F}_{z,^1S_0}(\rho, z) = -(U_\rho(\rho, z + h) - U_\rho(\rho, z))/h, \tag{4.40}$$

Here, the chain rule can be used to convert the radial force into the x and y force by multiplying F_ρ by x/ρ and y/ρ respectively. Only a different polarization has to be used for the states as was described earlier in section 3.1.

To now get the actual force, since particles are in a superposition, the particles have some weighting factor to which they feel the potential. This can be done using the $\vec{S}$ and $\vec{P}$ vectors, which tells us how big the probability is that a particle can be found in a quantum state given as

$$\vec{S}(\vec{c}_g) = \vec{c}_g \vec{c^*}_g, \tag{4.41}$$

$$\vec{P}(\vec{c}_e) = \vec{c}_e \vec{c^*}_e. \tag{4.42}$$

Again $\vec{c}_g$ and $\vec{c}_e$ are the coefficients vectors corresponding to the ground and excited state of length N. The corresponding strength particle i in superposition would feel due to the tweezer trap in the ρ and z directions respectively are

$$F_{i,r}(r, z) = F_{i,r,^1S_0}(r, z)S_i + F_{i,r,^3P_1}(r, z)P_i, \tag{4.43}$$

$$F_{i,z}(r, z) = F_{i,z,^1S_0}(r, z)S_i + F_{i,z,^3P_1}(r, z)P_i, \tag{4.44}$$

and the acceleration the particle would feel as a consequence is given by $a_i = F_i/m$.

Spontaneous emission

In contrast to the stimulated emission and absorption, spontaneous emission has a net influence on the motion of the particles. This process has already been described in section 4.2.2 and causes the excited atoms to decay to the ground state, emitting a photon in the process. This photon, with a kinetic energy $\frac{(\hbar\omega_0)^2}{2mc^2}$ and momentum $\frac{\hbar\omega_0}{c}$, causes the particle to move in opposite direction by the laws of energy and momentum conservation. The momentum kick the particle would experience as a consequence is

$$p_{\text{kick}} = mv = \frac{\hbar\omega_0}{c}, \tag{4.45}$$

following momentum conservation. This could also have been derived from the energy conservation equation, which states

$$\frac{(\hbar\omega_0)^2}{2mc^2} = \frac{1}{2}mv^2. \tag{4.46}$$

This is all fine in the discrete picture when the particle is definitely in the excited state, but again, the particle could also decay from a superposition state which would not obey energy conservation. This is because the energy the photon would have, corresponding to the transition frequency, is equal to the whole transition energy. This energy, when the particle is in the superposition state, does not have this energy and thus there is a difference in energy. To solve this in the simulation, the momentum kick might either happen or not, such that energy conservation takes place. To calculate this, particles that decayed from an almost excited state, say $|c_e|^2 = 0.9$, also have a 90% chance of gaining a momentum kick. Whether the momentum kick took place or not, the internal state of the particle is set back to the ground state as should be the case to conserve energy. This has been done to conserve the discrete momenta kicks, while still having the particles in a superposition state.

4.3.2 Energy

This part of the simulation is relatively straightforward since the calculations are just a consequence of the simulation itself and is merely used to visualize the things going on in the simulations. Different energy contributions will be explained and various distinctions can be made to visualize the dynamics better. This section will go into the total interaction energy, the total kinetic energy, the total potential energy, the temperature and the energy of individual particles. In this section the differential Stark shift will be defined, since this is a consequence of the difference between the potential energies between the S and P state.

Total interaction energy

This interaction energy contribution is very important to see in order monitor the particles potential energy during the interaction. This interaction energy is given by equation (4.32). If all the contributions of all the particles are added up, it should still be divided by two, since otherwise it would count the same potential energy twice; the potential particle one feels from particle two and vice versa. Since this interaction potential is also state dependent, the potential gets multiplied by the elements of the SP matrix from equation (4.38). Since the particles don't feel any force from the $|S + S\rangle$ channel as the particles would already be excited to the $|S + P\rangle$ channel, the $|S + S\rangle$ channel energy, coming from the short-range van der Waals interaction, is also not taken into account for the interaction energy.

Total potential energy and differential Stark shift

To get the full picture of all the conservative forces into play, also the trap forces should be taken into account. This is done by summing up the different contributions of the S state trapping

potential and the P state trapping potential in the following fashion

$$U_{pot}(r,z) = \vec{U}_{r,^1S_0}(r,z) \cdot \vec{S} + \vec{U}_{z,^3P_1}(r,z) \cdot \vec{P}, \tag{4.47}$$

where again the $\vec{S}$ and $\vec{P}$ vectors are used from equation (4.41) to take into account the internal state of the particles. The individual components of this sum give the potential trap energy for individual particles, indicating whether or not they would leave the trap. The inner product, however, gives insights into the total potential of the trap. The total potential energy consists of the total interaction energy and the total potential trap energy.

The differential Stark shift is calculated as the differences of the potential trap energies as

$$\Delta E_{dSs} = \Delta E_{dSs,r} + \Delta E_{\text{dSs},z} \tag{4.48}$$
$$= (U_{r,^1S_0}(r,z) - U_{r,^3P_1}(r,z))/\hbar + (U_{z,^1S_0}(r,z) - U_{z,^3P_1}(r,z))/\hbar, \tag{4.49}$$

where $\hbar$ is the reduced Planck constant, which gives the outcome in units of rad/s and produced figure 4.1.

Total kinetic energy and temperature

The kinetic energy of the system can be calculated using the expression $E_k = \frac{1}{2}mv^2$, where m is the mass of the strontium-88 atoms and v is the velocities of the atoms. The kinetic energy contributions of the atoms can be summed to know the total contribution of the kinetic energy. This is important, since the total contribution of the kinetic energy together with the total potential energy of the system, described in the section above, should add up to a constant; the total energy of the system, which should stay constant without the influence of any collision laser.

It is also useful to look at the temperature. Usually this property can be calculated using the relation $E = k_B T$, but since this relationship is ill defined at small particle numbers, therefore it is better to use the molecular description of the temperature given by[51]

$$T = \frac{mv_{RMS}^2}{3R}, \tag{4.50}$$

where $v_{\text{RMS}} = \sqrt{\frac{1}{N}\left(\sum_{i=1}^{N} v_i\right)}$ representing the velocity Root Mean Square of all the particles normalized by the number of particles, R is the gas constant given by 8.3144598 and m is the molar mass of strontium-88 and is measured at $0.0879\,\text{kg/mol}$.

Part III

Results

Chapter 5

Simulation results

In the first part we have explained the scattering theory, the internal state of the particles and laser properties. In the second part the simulation was explained and how it operates. In this chapter I will first show some initial results to give an intuitive picture, later this picture will be expanded towards a bigger picture in which the trap loss profile that we are mostly interested in is explained. This trap loss profile is the energy gain due to two-body collisions as a function of the detuning and can be found in the theory in equation (2.13). This trap loss profile can then be used to calculate the trap loss as will be done in section 6. However, another goal of this section will be to explain the filling factor of the tweezer array, which can be calculated when knowing the one- over two-body losses[13].

In order to enhance the filling factor of the tweezer array for strontium-88 atoms, various simulations have been done within a semiclassical framework. In these simulation, two-body collisions in individual tweezer traps have been investigated. The individual tweezer traps can then be expanded to the bigger tweezer array picture as every tweezer trap is the same. By doing the simulation enough one can calculate the filling factor.

The simulation result will furthermore give insights into of the dynamics of the particles and the internal state of the particles. This last factor is mainly determined by the detuning felt by the particle and the strength of the interaction. This detuning δ, is the detuning set by the collision laser as explained in section 4.2.1. The strength of the coupling between the ground and excited state is determined by the Rabi frequency Ω. As a consequence of the effective detuning and the Rabi frequency, one can investigate the dynamics of the particles. The forces in the simulation are determined by spontaneous emission processes, the tweezer potential and the interaction potential, as explained in section 4.3.1. Since excitations to the excited state interaction potential can cause extra energy into the system during a collision, particles can increase in energy, thereby leaving the trap.

5.1   Goal of the simulation

To understand the dynamics at play of the two-body collision between strontium-88 atoms in order to calculate the ratio of one- over two-body losses and to determine the trap loss profile, the semiclassical simulation will be used. This time-dependent simulation makes it easy to interpret, which then makes it easier to set up a quantum framework. To investigate the interaction, several ranges of the Rabi frequency Ω and the detuning δ will be varied in order to answer the two main questions. Namely:

1. What combination of the detuning and the Rabi frequency leads to the highest ratio of one-body losses over two-body losses?

2. What is the energy release per collision as a function of the detuning?

The first question would give immediate insights into the preparation efficiency of the tweezer array, and is the main goal of this thesis paper. However, since this would only give the answer semiclassically, we are also interested in the trap loss as function of the detuning, which we call the trap loss profile. To answer this, the second question is important, because if one knows what the energy increase is per collision semiclassically, one can combine this to the transition probability quantum mechanically. From that, the relative trap loss can be calculated, giving a better picture of the problem as will be done in chapter 6.1.

In order to answer these questions, various kinds of simulations were performed. The Rabi frequency was varied from 0.01 MHz to 50 MHz and the detuning was varied from 0 MHz to 20 MHz. The end limits of both variables are relatively high. For the Rabi frequency this end limit is defined as 50 MHz, since this would make the transition extremely saturated 2.5.2, causing a lot of heating. Whereas the end limit for the detuning is taken to be 20 MHz, which is approximately seven times the trap depth 4.2.1. Seven times the trap depth might seem high, since this detuning might scale linearly with energy in theory. However, the energy gain during collisions might be far from optimal for large detunings or low Rabi frequencies because these parameters can prevent the particles to effectively reach the excited state. Given the end limits of both parameters, a huge range of variables were tested to see what is optimal in the different regimes.

The simulation section will start with an explanation of the energies and its effect on the internal quantum states using the effective detuning, a concept introduced in section 4.2.1. Then we show the the decay curve of the simulation, which is affected by the internal state. These decay curves are important since they cause spontaneous decay for the particles which will affect the energy.
When all the important parts of the simulation are explained and visualized. The real simulation results are showed starting with an one-particle simulation to see the energy change over time without any multiple body collision. Then, we show the two-particle simulations to see how the energy increases including particle collisions. For both the simulations results, the maximum energy increase and the average energy will be shown and in case one or two particles leave the trap, the energy of the second particle is shown as soon as the first particle leaves the trap.
If both the simulations for one- and two-particles are listed and analyzed, one can calculate the contribution of the two-atom collisions as will be done in section 5.1.4. This energy gain due to the collisions as function for the detuning will then later be used to construct a trap loss profile as function of the detuning. All detunings in this chapter are expressed in MHz and the simulation plots in this chapter have been made using the code B.6.

5.1.1 Energies, internal quantum states and the decay curve

In this section, both the effect of the interaction energy on the internal quantum states as the effect of the internal quantum state on the decay curve will be explained following the discussion in part 4.2.1. Both simulations are performed with 10 particles, where every particle has a different color in the plots. Whenever just one color can be seen per time, it means that the colors overlap and that all the particles are in the same state or follow the same decay curve as will be seen later.

Energies and internal quantum state

To see the interplay between potential and kinetic energy and how it effects the internal state of the particles, it might be useful to see figure 5.1. At 10 µs the potential energy is low, indicating that the particles are below in the trap. Then directly after, when the internuclear distance between the particles becomes less, the interaction energy increases which causes some particles to become resonant with each other, as can be seen in the interaction energy by the small green peak at 11 µs. As a consequence of the interaction energy, the particles get excited to the excited states as can be

seen below in figure 5.1 where a few particles are now in a superposition of the ground state and excited state given by probability of measuring the particle in the excited state P_e. Around 12 µs the particles are out of resonance again, creating a small dip in the total potential energy before going to the outsides of the trap at 15 µs. In this period, the particles are not in resonance with the collision laser, as can also be seen in the out of resonance Rabi oscillations, which oscillate with constant amplitude (A.82). The second time the particles come close and get into resonance with each other is at 21 µs, where again, the Rabi oscillation amplitude and frequency changes according to the theory (A.82). During this whole process, the total energy of the system stays constant as no excited interaction potential or spontaneous emission is taken into account yet, this total energy is visualized by the black line at 1.3×10^{-4} K.
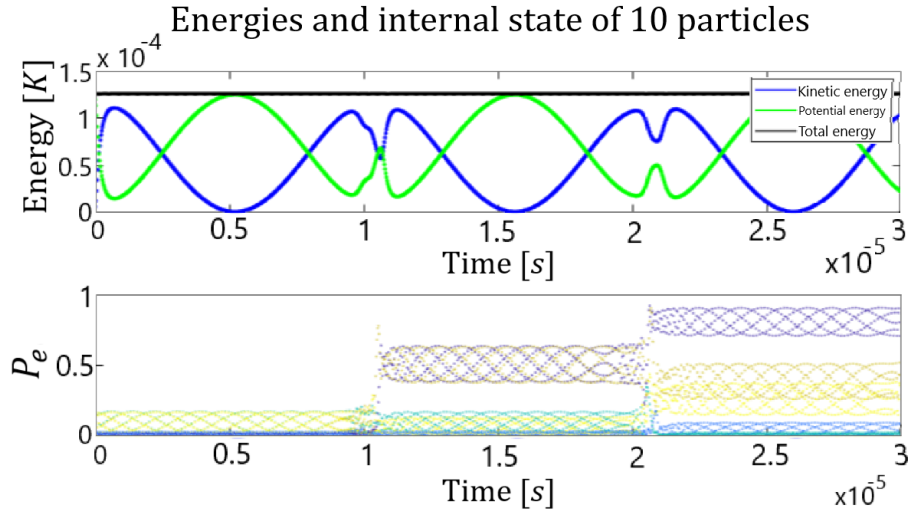
Figure 5.1: Example of energy plots (above) and the probability of measuring the particles in the excited state P_e (below). Without taking into account the differential Stark shift, the excited interaction potential and spontaneous emission processes. Above: the kinetic energy (in blue) and the potential energy (in green) oscillate in anti-parallel fashion while still having a constant energy (in black). At 11 µs and 21 µs the interaction energy increases causing some particles to become resonant. Below: Rabi oscillations of 10 particles starting off in the ground state. At 11 µs and 21 µs some particles get into resonance causing the Rabi oscillation to change in amplitude.

Internal quantum state and decay curve

Now we know how the position of the particles in the trap affects the internal state we will now look at how the internal state affects the decay curve. The decay curve is calculated per particle dependent on its internal state and it represents the amount of decayed particles if it was represented by an ensemble of particles. The change in this decay curve per time step then determines the chance of one particle to decay. If the particle is in the ground state, the effective decay constant is zero and and the curve stays flat whereas if the particle is in the excited state the decay constant is equal to the original decay constant defined as $1/\tau$. This can all be read back in the simulation outline in section 4.2.2.

An example of this decay curve is given in figure 5.2, where the particles start in the excited state and undergo Rabi oscillations with a detuning of zero (independent of its particle position) as can be seen in the upper plot. This will result in an effective decay rate using equation (4.30) the decay curve iterates as $P_{\text{decay}}(t_{i+1}) = \frac{P(t_i)}{1+\tilde{\Gamma}_{i \to f} dt}$, here $\tilde{\Gamma}_{i \to f}$ is defined as the effective decay rate given by 4.29

$$\tilde{\Gamma}_{i \to f} = \frac{2\pi}{\hbar} |c_e|^2 \langle g| H |e \rangle = |c_e|^2 \Gamma_{i \to f}. \tag{5.1}$$

As a consequence, the individual decay curves do not rise as fast on average as was the case in figure 4.5, where the particles stayed in the excited state. This is also expected considering the particles are half as much in the excited state. The chance of decaying per time step is defined as the change of this decay curve per time step $(P_{\text{decay}}(t+1) - P_{\text{decay}}(t))$. If this decay chance is then accepted it means that the particle will decay back to the ground state possible emitting a photon and increasing its kinetic energy, this is the case since energy conservation does have to take place as explained in the section 4.3.1. In this plot $\Omega = 2\pi \, \text{MHz}$ has been used.
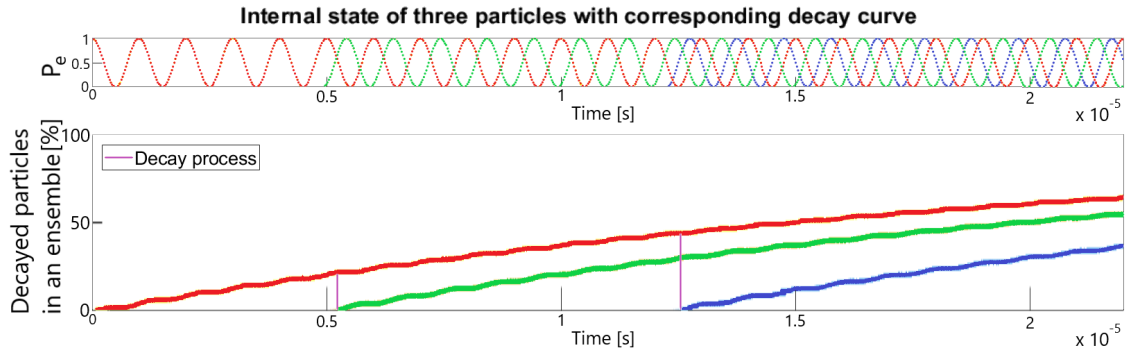

Figure 5.2: Rabi oscillations and decay curve for N=10 for $\Omega = 2\pi \, \text{MHz}$ and $\delta = 0 \, \text{Hz}$. In the upper plot the Rabi oscillations are plotted with on the y-axis the probability of being in the excited state. Every color represents a different particle. Below, the decay curve as a consequence of the effective decay rate is plotted. Here the curve is flat as soon as the particle is in the ground state and back to the original decay rate as the particle is in the excited state. We can see that the green particle and the blue particle decayed at respectively $5 \, \mu s$ and $12 \, s$.

5.1.2 One-particle simulation: How the energy changes without two-body collisions

Now both the effective detuning and the effective decay rate are showed and how they affect and are affected by the kinetic energy, via spontaneous emission, and by the interaction energy respectively, we can now combine everything into one simulation and look at one particle first.

Starting with the one-particle case, not much is expected to happen, since no two-body scattering processes can take place. However, since the simulation starts off at a recoil temperature of $1 \, \mu K$ using Sisyphus cooling, the atoms can warm up to the Doppler limit, depending on discrete velocity steps taken caused by spontaneous emission. This increase in temperature is expected for higher Rabi frequencies and lower detunings since this would cause more transitions and thus more spontaneous emission events leading to the discrete energy steps. To see whether this is the case, the figures 5.3a and 5.3b are shown below for the cases $\Omega = 1 \, \text{MHz}$ $\delta = 0 \, \text{MHz}$ and $\Omega = 1 \, \text{MHz}$, $\delta = 20 \, \text{MHz}$ respectively, such that only the detuning varies. The $\delta = 0 \, \text{MHz}$ simulation is to be found in the excited state more often, resulting in a higher heating rate due to spontaneous emission as can be seen in the energy difference during the whole run in the figures 5.3a and 5.3b. Since the energy increase is only caused by spontaneous emission we can conclude that having a low detuning causes more global heating, which is heating caused not due scattering events but due to spontaneous emission. One could check this by looking at the decay curves and counting the decay events and this is again the most for low detunings. These spontaneous emission events are caused by a lot of excitations which is indeed the case for low detunings following the theory. The simulations take $22 \, \text{ms}$, which is a thousand times the lifetime of the excited $^3P_1$ state of strontium-88. This simulation times ensures that the results are not too much affected by fluctuations, while still having reasonable computation times. Also, the kinetic energy and potential energy that is plotted represents the $0.1 \, \mu s$ average energy. This value is chosen to be larger than the oscillation

time inside the trap such that the oscillations cancel each other making the line flatter and to make the plots more clear.
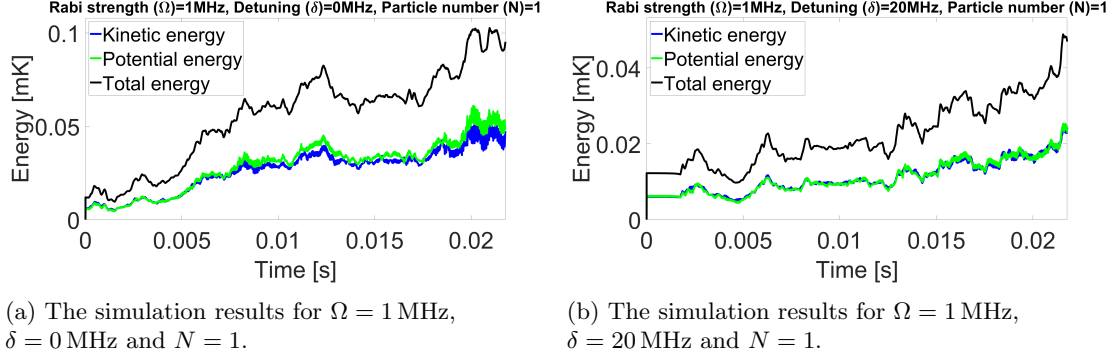

(a) The simulation results for $\Omega = 1\,\mathrm{MHz}$, $\delta = 0\,\mathrm{MHz}$ and $N = 1$.

(b) The simulation results for $\Omega = 1\,\mathrm{MHz}$, $\delta = 20\,\mathrm{MHz}$ and $N = 1$.

Figure 5.3: The energy as a function of time is given from $t = 0$ to $t = 22\,\mathrm{ms}$, in blue the kinetic energy is given, in green the potential energy is given and in black the total energy is given, for a time average of $0.1\,\mu\mathrm{s}$. One can see that for the low detuning (left) more spontaneous emission takes place than for the case of high detuning (right) causing more global heating.

To expand all the results for the one-particles simulations, all the results for all the different ranges of the Rabi frequencies and the detuning, plots 5.4a and 5.4b are shown below. In this first plot on the left, the average energy is shown as function of the detuning for different Rabi frequencies and in the second plot on the right, the maximum energy from the starting temperature during the simulation has been plotted as function of the detuning for different Rabi frequencies. The average energy of the particles is more reliable parameter, since it is the average over time whereas the maximum energy tells us about the energy deviation and the change of particles which might have left the trap. In the cases where the Rabi frequencies is between $0.01\,\mathrm{MHz}$ and $1\,\mathrm{MHz}$ particles did not leave the trap and are therefore plotted. Some of the particles however, left the trap for Rabi frequencies of $5\,\mathrm{MHz}$ and $50\,\mathrm{MHz}$ and are therefore listed below in a table. In tables 5.1 and 5.2 again the average energy and the maximum energy are displayed. However, the runs with particle losses are indicated by " $-$ ". The maximum energy deviation, for the one-body runs whose atom left the trap, are namely $120\,\mu\mathrm{K}$, as this is the trap depth for the S state potential. To still distinguish between the simulations with trap loss, the time it took the particles to leave the trap has been given in table 5.3.

Energy [µK]		Detuning δ				
		0 MHz	5 MHz	10 MHz	15 MHz	20 MHz
Rabi Ω	5 MHz	0.038	-	-	-	0.011
	50 MHz	-	0.061	-	0.018	0.047

Table 5.1: The average energy of the system during the 22 ms for one particle. Here values for the Rabi frequency Ω between $0.01\,\mathrm{MHz}$ and $50\,\mathrm{MHz}$ have been used with detunings δ between $0\,\mathrm{MHz}$ and $20\,\mathrm{MHz}$. '-' means that the particle lost the trap.

Energy [µK]		Detuning δ				
		0 MHz	5 MHz	10 MHz	15 MHz	20 MHz
Rabi Ω	5 MHz	79.89	-	-	-	26.44
	50 MHz	-	93.66	-	65.61	99.80

Table 5.2: The maximum energy deviation in µK. Maximum energy deviation during the 22 ms for one particle. Here values for the Rabi frequency Ω between $0.01\,\mathrm{MHz}$ and $50\,\mathrm{MHz}$ have been used with detunings δ between $0\,\mathrm{MHz}$ and $20\,\mathrm{MHz}$. '-' means that the particle lost the trap.
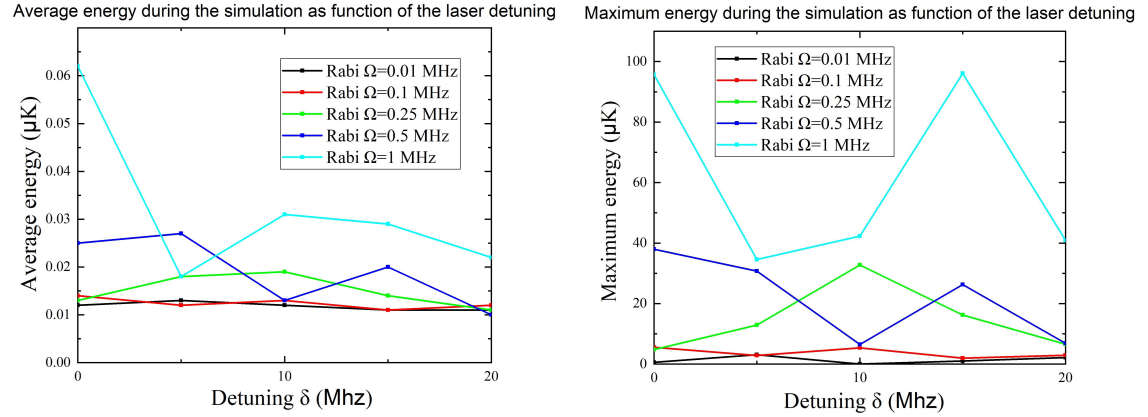
(a) The average energy during the one-particle simulation runs for different Rabi frequencies as a function of the detuning.

(b) The maximum energy during the one-particle simulation runs for different Rabi frequencies as a function of the detuning.

Figure 5.4: The average energy (left) and maximum energy (right) for the one-particle runs as a function of the detuning. Every color represents a Rabi frequency. Only the Rabi frequencies where no particle left the trap are plotted. Those results are listed in the tables.

Duration [ms]		Detuning δ				
		0 MHz	5 MHz	10 MHz	15 MHz	20 MHz
Rabi Ω	5 MHz	-	0.011	0.017	0.017	-
	50 MHz	0.006	-	0.009	-	-

Table 5.3: The duration for the particles to leave the trap during the 22 ms for one particle. Here values for the Rabi frequency Ω between 0.01 MHz and 50 MHz have been used with detunings δ between 0 MHz and 20 MHz. '-' means that particles did not leave the trap.

Summary for the one-particle

In the table 5.3 it can be seen that for Rabi frequencies higher than 5 MHz, the heating is already big enough for particles to leave the trap. For small Rabi frequencies, below 0.25 MHz, the heating is almost zero and no differences per detuning can be found as could be seen in figure 5.4a. In the optimal regime between 0.25 MHz and 5 MHz a maximum heating is found for a detuning between 0 MHz and 10 MHz, as here the energy deviation is much higher than for detunings higher than 10 MHz.

To state it more generally, the coupling between the ground and excited state channel, caused by the Rabi frequency, of the strontium-88 atoms cannot be too large or too small, since this would couple the states too much or too little, causing the particles to heat up too much due to spontaneous emission or get no excitation at all. For the intermediate regime, the detuning can be checked, since here the coupling is in the middle, meaning no other process is dominant. In this regime, the energy increase is the highest for low detuning, since this would imply many spontaneous emission processes. There is no upper bound for the detuning, since no scattering processes are taken into account yet. This will be investigated in the next section.

5.1.3 Two-particle simulation: How two-body collisions changes the trap loss and energy gain

For the case where two particles are in the trap, the interaction energy between particles is not zero anymore and the colliding atoms can come into resonance with the light field. The resonance condition is given by the effective detuning, the detuning felt in the frame of reference of the strontium-88 atoms, being equal to zero, see also equation (4.8). When the particles are resonant, the internal state of the particle, which is mainly in the ground state being far away from each other, can excite to the P state, gaining some extra energy moving in the dipole interaction potential. One can then extrapolate the energy increase for the scattering processes when comparing the one particle simulation runs to the two-particle simulation runs. In this section, three examples have been chosen with different Rabi frequencies and detunings in figure 5.5a, 5.5b and 5.5c, which are the $\Omega = 0.25\,\mathrm{MHz}$, $\delta = 0\,\mathrm{MHz}$, the $\Omega = 1\,\mathrm{MHz}$, $\delta = 5\,\mathrm{MHz}$ and the $\Omega = 1\,\mathrm{MHz}$, $\delta = 10\,\mathrm{MHz}$ simulations respectively. After the individual cases, more general figures and tables are shown visualizing the same emergence properties as in the previous section (the maximum energy deviation, the average energy and the energy of the second particle after the first one left). Rabi frequencies and detunings are chosen in the same regime as in the previous section.

Example 1: Comparing same detuning ($\delta = 5\,\mathrm{MHz}$) and different Rabi frequency ($0.25\,\mathrm{MHz}$ and $1\,\mathrm{MHz}$). Between the first figure (5.5a) and second figure (5.5b), only the Rabi frequency differs by a factor of 4 resulting in less energy gain for the lower Rabi frequency. This is because particles cannot properly excite to the P state resulting in less spontaneous emission and less movement in the repulsive dipole in the $|S + P\rangle$ channel both causing extra energy into the system. This can be checked, since the population of the internal state for both particles is less in the excited state on average for the $\Omega = 0.25\,\mathrm{MHz}$ case compared to the $\Omega = 1\,\mathrm{MHz}$ case.

(a) Simulation results for $\Omega = 0.25\,\mathrm{MHz}$, $\delta = 5\,\mathrm{MHz}$ and $N = 2$.

(b) Simulation results for $\Omega = 1\,\mathrm{MHz}$, $\delta = 5\,\mathrm{MHz}$ and $N = 2$.

(c) Simulation results for $\Omega = 1\,\mathrm{MHz}$, $\delta = 10\,\mathrm{MHz}$ and $N = 2$.
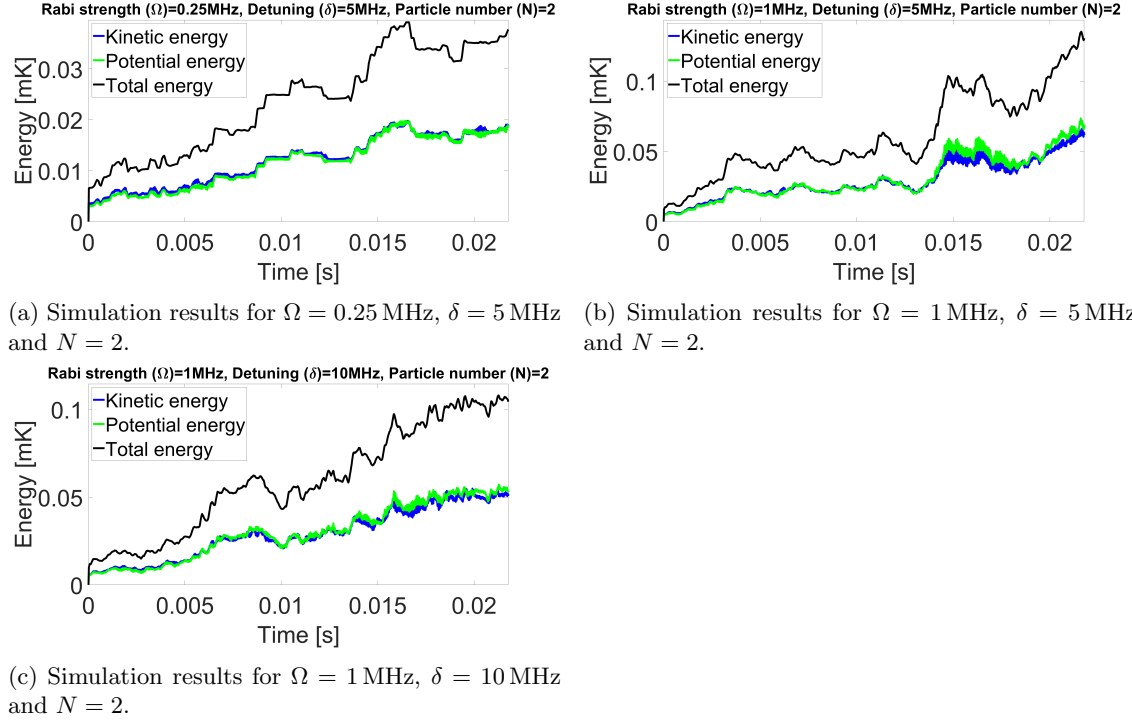
Figure 5.5: The energy as a function of time is given from $t = 0$ to $t = 22\,\mu\mathrm{s}$. In blue the kinetic energy is given, in green the potential energy is given and in black the total energy is given. Figure a) and c) are less optimal because of the lower Rabi frequency or higher detuning respectively, whereas figure b) is the most optimal. The energy is taken to be the $0.1\,\mu\mathrm{s}$ average energy to make the blue and green oscillations lower in amplitude.

Example 2: Comparing same Rabi frequency ($\delta = 1\,\mathrm{MHz}$) and different detuning ($5\,\mathrm{MHz}$ and $10\,\mathrm{MHz}$). Comparing the second figure (5.5b) and third figure (5.5c), only the detuning differs by a factor of 2. Less energy is gained in the case with larger detuning, because the particles are less in the excited state, because the particles are less in resonance with the transition frequency, leading to Rabi oscillations with a smaller amplitude (A.82). Being in the excited state less, means less spontaneous emission, which causes fewer momenta kicks by the photon decay. One can check this by examining the decay curves. Since the decay curves are flatter for the higher detuning, one can conclude fewer spontaneous emission processes have taken place. This could have been compensated by the energy gain during the collisions, since a higher detuning means moving from higher up in the repulsive potential, but this happens not to be the case.
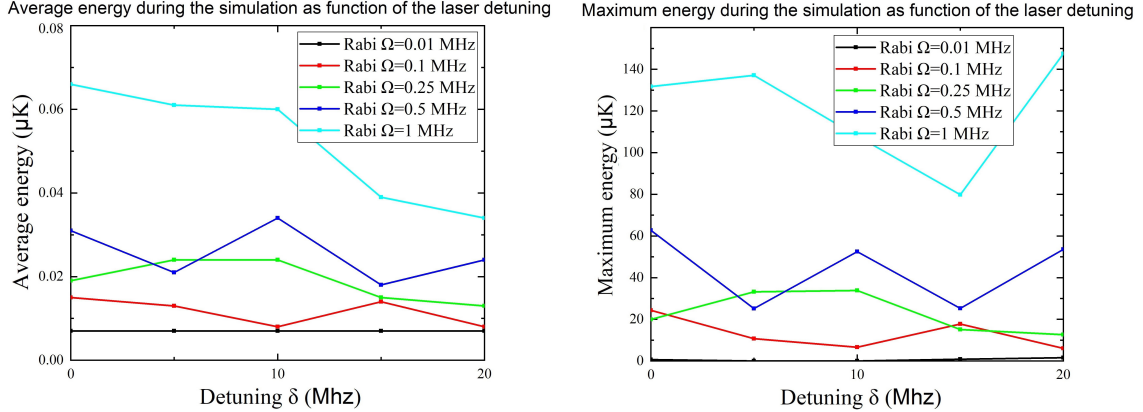
(a) The average energy during the two-particle simulation runs for different Rabi frequencies as a function of the detuning

(b) The maximum energy during the two-particle simulation runs for different Rabi frequencies as a function of the detuning

The results of the maximum energy deviation and the average energy, for all different Rabi frequencies and detunings, are listed in figures 5.6a and 5.6b, and tables 5.4 and 5.5 for the average energy and the maximum energy deviation respectively. Again, the figures are for Rabi frequencies between 0.01 MHz and 1 MHz, since in these simulations no atoms left the trap, wheras with a Rabi frequency of 5 MHz and 50 MHz particles did leave the trap and are therefore listed in the tables. Also, since in the two-particle runs one atom can stay in the trap, the time it took for the first particle to leave the trap are notated in table 5.6, also the energy of the second particle is listed in table 5.7.

Similar to the one-particle runs, both Rabi frequencies too low and too high can be eliminated. For Rabi frequencies too low ($\Omega \leq 0.25$ MHz) this is due to a lack of energy gain from spontaneous emission processes as was already seen from the one-particle runs but also no significant energy gain due to scattering processes between the particles was found. This can be explained by the fact that particles could not properly excite to the P-state, see equation (A.82), and therefore not gain energy when moving along the repulsive dipole potential of the strontium-88 atoms. For Rabi frequencies too high ($\Omega \geq 5$ MHz), again as we have already seen for the one-particle case, atoms heat up too much due to spontaneous emission processes causing global heat into the system. Global heat will not selectively induce one-body collisions and is therefore not desired.

In contrast to the one-particle simulation, there is not as clear of a relation between the detuning and the energy increase as we saw for the one-particle case. This is because for low detuning, the particles heat up, but at the same time induce no effective scattering processes where energy can be gained, whereas for higher detuning ~ 5 MHz, less spontaneous emission takes place, but the energy gain during scattering processes is more effective. This trade-off already gives a bit of insight in how the scattering processes for strontium-88 atoms effect the energy increase. In the next section the effects of spontaneous emission will be eliminated partly in order to make better conclusions about these scattering processes.

Energy [μK]		Detuning δ				
		0 MHz	5 MHz	10 MHz	15 MHz	20 MHz
Rabi Ω	5 MHz	-	-	-	-	-
	50 MHz	211.42	-	233.86	-	233.22

Table 5.4: The largest temperature deviation during the 22 ms for two particles. Here values for the Rabi frequency Ω between 0.01 MHz and 50 MHz have been used with detunings δ between 0 MHz and 20 MHz.'-' means that particles did leave the trap.

Energy [µK]		Detuning δ				
		0 MHz	5 MHz	10 MHz	15 MHz	20 MHz
Rabi Ω	5 MHz	-	-	-	-	-
	50 MHz	0.103	-	0.142	-	0.091

Table 5.5: The average energy of the system during the 22 ms for two-particles. Here values for the Rabi frequency Ω between 0.01 MHz and 50 MHz have been used with detunings δ between 0 MHz and 20 MHz. '-' means that particles did leave the trap.

Duration [ms]		Detuning δ				
		0 MHz	5 MHz	10 MHz	15 MHz	20 MHz
Rabi Ω	5 MHz	0.007	0.008	0.009	0.006	0.007
	50 MHz	-	0.007	-	0.010	-

Table 5.6: The duration for the particles to leave the trap during the 22 ms for two particles. Here values for the Rabi frequency Ω between 0.01 MHz and 50 MHz have been used with detunings δ between 0 MHz and 20 MHz. '-' means that particles did not leave the trap.

| Energy [µK]		Detuning δ				
		0 MHz	5 MHz	10 MHz	15 MHz	20 MHz
Rabi Ω	5 MHz	0.019	0.063	0.009	0.018	0.015
	50 MHz	-	0.071	-	0.029	-

Table 5.7: The energy of the second particle after the first one left the trap at times notated in table 5.6. Here values for the Rabi frequency Ω between 0.01 MHz and 50 MHz have been used with detunings δ between 0 MHz and 20 MHz. '-' means that particles did not leave the trap.

5.1.4 Trap loss profile for different detunings

Now that the one- and two-particle simulations are listed, it is useful to abstract the information which is needed to understand the two-body collisions by eliminating the one-body effects, namely spontaneous emission. To do this, the energy gain for the two-particle simulation will be subtracted by the energy gain for the one-particle simulation, leaving us mainly with the contributions caused by the two-body collisions. In equation form, this yields

$$E_{\text{2-body collisions}} = E_{\text{2-particle}} - E_{\text{1-particle}}, \tag{5.2}$$

where $E_{\text{1-particle}}$ is the average energy for the one particle simulation given by figure 5.4a and table 5.1 and $E_{\text{2-particle}}$ is the average energy for the two particle simulation given by figure 5.6a and table 5.5. This procedure will be done for the average energy as well as for the maximum energy and the results are in figure 5.7a and 5.7b for Rabi frequencies $\Omega \leq 1$ MHz and in tables 5.8 and 5.9 for $\Omega \geq 1$ MHz. Notice that ideally one would multiply the one-body contributions by a factor of two, because when the two bodies are not interacting, two individual one-body processes take place. This, however, did not match very well with the data, since it produced too many negative numbers. This could be explained by particles bouncing off each other both losing energy during the collision.
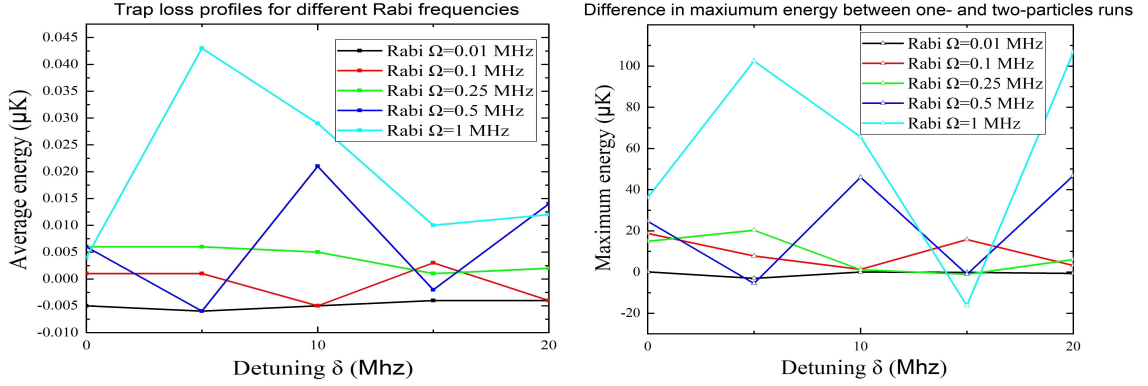
(a) The trap loss profiles for different Rabi frequencies as a function of the detuning. Here the light-blue line represents the trap loss profile which will be used in the next section.

(b) The difference in maximum energy between the two- and one-particle runs for different Rabi frequencies as a function of the detuning.

Energy [µK]		Detuning δ				
		0 MHz	5 MHz	10 MHz	15 MHz	20 MHz
	1 MHz	36.03	102.48	65.66	-16.29	106.62
Rabi Ω	5 MHz	-	-	-	-	-
	50 MHz	-	-	-	-	142.42

Table 5.8: The difference in maximum energy deviation between one- and two-particle simulation runs during the 22 ms. Here values for the Rabi frequency Ω between 1 MHz and 50 MHz have been used with detunings δ between 0 MHz and 20 MHz.

Energy [µK]		Detuning δ				
		0 MHz	5 MHz	10 MHz	15 MHz	20 MHz
	1 MHz	0.004	0.043	0.029	0.010	0.012
Rabi Ω	5 MHz	-	-	-	-	-
	50 MHz	-	-	-	-	0.044

Table 5.9: The difference in average energy between the one- and two-particle simulation runs during the 22 ms. Here values for the Rabi frequency Ω between 1 MHz and 50 MHz have been used with detunings δ between 0 MHz and 20 MHz.

In addition to the discussion in the previous section of the two-particle run, a better conclusion can be drawn now. It is clearly visible, from tables 5.8 and 5.9 about the difference in energy deviation and difference in average energy respectively, that the energy gain is mostly in the 5 MHz to 10 MHz regime, as was expected given the small discussion in section 5.1.3. Also, it is clearly noticeable that for Rabi frequencies that are too low, there is not enough coupling, leading to no effective light induced collision. For Rabi frequencies that are too high, a huge difference in energy between the particles can effectively be created by collisions, but particles also gain energy without collisions in spontaneous emission processes. Also visible, is the ratio between the two δ^2/Ω^2, representing the Rabi oscillation amplitude (A.82). When this ratio is small, particles tend to be more in the ground state prior to a collision and can then more effectively gain energy during the collision, as would be optimal to create a huge energy deviation between the particles, causing more one-body losses to take place. In contrast. If this Rabi oscillation amplitude is big, particles are already more in the excited state prior to the collision causing the scattering events to be less optimal. This relation can be checked in the figures 5.7a and 5.7b, where we see a larger energy increase caused by scattering events for higher detuning when also the Rabi frequency is

increased. This argument can also be turned around, as only higher Rabi frequencies are relevant as soon as the detuning increases.

Some final remarks about the use of these numbers is to give insight into the dynamics at play. Relevant trade-offs have been showed between the spontaneous emission events and photon absorption and emission. Also, a reasonable regime to look in has been found together with an interesting relation between the detuning and the Rabi frequency. Within these regimes one could find the energy increase per detuning and creating a trap loss profile for the quantum calculations, as will be applied in the next section about the quantum nature of the strontium-88 particles within the tweezer trap.

Chapter 6

Wavefunction overlap and trap loss

In this chapter, a quantum approach will be taken into account, since the simulation does not take the wave-like nature of the atoms into account. This approach considers the trap to be an infinite well potential in which the overlap matrix has been calculated between the ground state and excited state wave function. Using this overlap matrix one can calculate the transition probability and thereby calculate the energy gain of the system. However, since this energy gain depends on the detuning, one will get the trap loss as function of the detuning. This trap loss as function of the detuning is called the trap loss profile, and will be considered for three cases, namely a constant trap loss profile, an analytic trap loss profile and a trap loss profile connected to the simulation.

6.1   Wave function overlap

For the trap loss calculations, the trap loss equation (2.13) it is important to calculate the overlap matrix, which tells us something about the excitation probability for the strontium-88 atoms from the ground to the excited state, which will be done in this chapter. This will be done by calculating the wave function of the ground state potential and the excited state potential in order to eventually calculate the overlap matrix. With this overlap matrix, the trap loss can be calculated using the trap loss profile $A'(\Delta)$, also from equation (2.13). This total trap loss corresponds to the master trap loss from section 2.6. All of these calculations have been done using the code B.7.

Ground state wave function
For the ground state wave function, equation (3.1) has been used for the ground state potential with the parameters explained below this equation. Since the potential is only given by a van der Waals potential, it is important to approximate the short-range using the scattering length $a = -2\,a_0$, explained in section 2.4.1, and to connect it to the long-range wave function, explained in section 2.4.4, using the log derivative method[52]. This has been done for the radial wave function multiplied by a factor $k \cdot R$ in figure 6.1, $k(R)$ being the wave vector at an internuclear distance R. Since only sin and cos functions are used here, the amplitude is never higher than one. The trap width is taken such that the ground state wave function at $1\,\mu K$ is zero at the end of the trap as would be the case for an infinite well potential. We also assume that the collision takes place at the center of the trap and that the end of the trap is determined by the effective range, which is explained in section 4.2.1. In the ρ-direction, the effective range is taken to be $0.5\,\mu m$. The trap width corresponding to this effective range is $8813\,a_0$, with the constraint that the wave function should be zero at the boundaries with an integer quantum number. This does not hold for higher energetic states, as can be seen in the pictures. However, wave functions at higher temperatures at far internuclear distances, contribute less to the wave function overlap, as
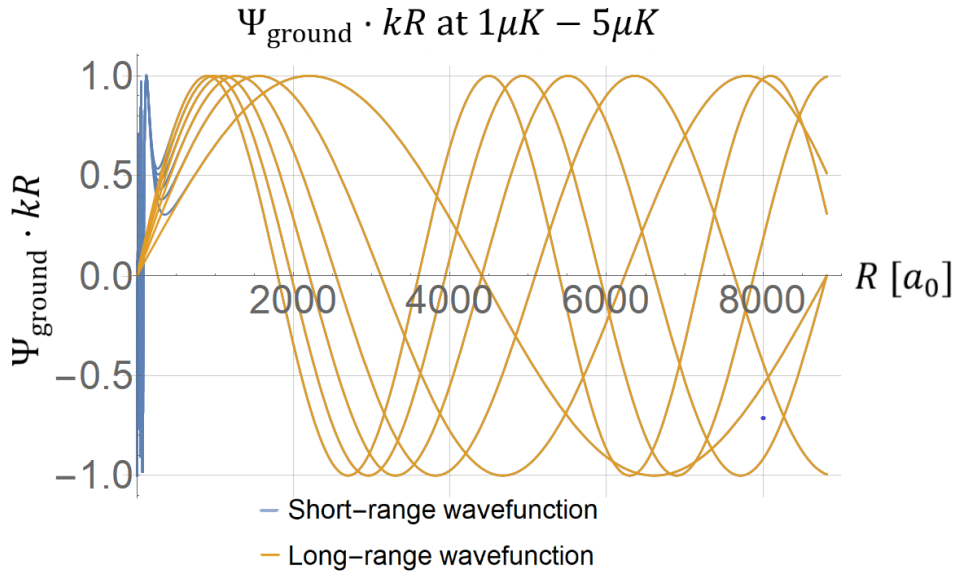
Figure 6.1: Connection short- and long-range wave function for $\Psi_{\text{ground}}(R) \cdot kR$ in a van der Waals potentials for energies of $1\,\mu\text{K}$, $2\,\mu\text{K}$ up to $5\,\mu\text{K}$. Plotted from $R = 0$ to $R = 8813\,a_0$.

will be seen later on. In all the pictures, it is important to keep in mind that the wave function with the highest asymptotic wavelength is the wave function of the lowest energy. For these plots, five different energies have been chosen corresponding to energies of $1\,\mu\text{K}$, $2\,\mu\text{K}$ up to $5\,\mu\text{K}$. In figure 6.2, the actual normalized wave function for these energies have been plotted, which already shows the importance of the short-range regime around the classical Condon point. At larger internuclear distances, the wave function takes on lower values due to the $1/R$ dependence. Finally this ground state wave function for the $|S + S\rangle$ channel has been plotted only in the short-range in figure 6.3. Here, at small R the reflection effects from the nucleus can be seen which interfere destructively at very small R and constructively interfere at bigger R, which corresponds to the solutions explained in section 2.4.2. Around $70\,a_0$, the asymptotic wave function can already be seen, which confirms the choice of connecting the short-range and the long-range at a value of $200\,a_0$.

Excited state wave function

For the excited state scattering wave function, different approaches have been used to calculate the shape in order to confirm the shape, without normalization, which are all stated in section 2.4.3. In figure 6.4, the short- and long-range scattering wave functions multiplied with a factor of kR have been calculated. The wave functions, until the classical Condon point, increase exponentially, as can be seen coming from low R values. Then, around the Condon point, the Airy functions can be seen with a slightly higher amplitude than the sin function in the asymptotic regime, as has been described in sections 2.4.3 and 2.4.4. Also here, the wave function has been calculated for energies of $1\,\mu\text{K}$, $2\,\mu\text{K}$ up to $5\,\mu\text{K}$. In the figure 6.5, the radial wave function has been plotted, in which it drops off for higher R values.

Wave function overlap
Now that the ground and excited state potentials have been calculated, one can calculate the wave function overlap using the equation (2.12)

$$F_{fi} = \left| \int_0^\infty \psi^- (r, E_{\text{e}}) \, \psi^+ (r, E_{\text{g}}) \right|^2 . \tag{6.1}$$
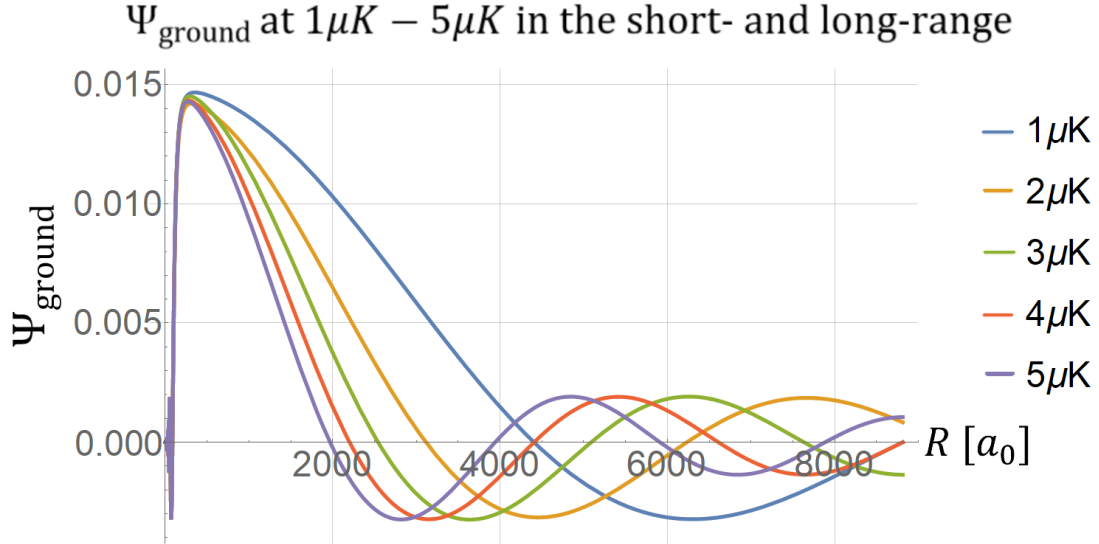
Figure 6.2: Short- and long-range ground state wave function $\Psi_{\text{ground}}(R)$ in a van der Waals potential for energies of $1\,\mu K$, $2\,\mu K$ up to $5\,\mu K$. Plotted from $R = 0$ to $R = 8813\,a_0$.
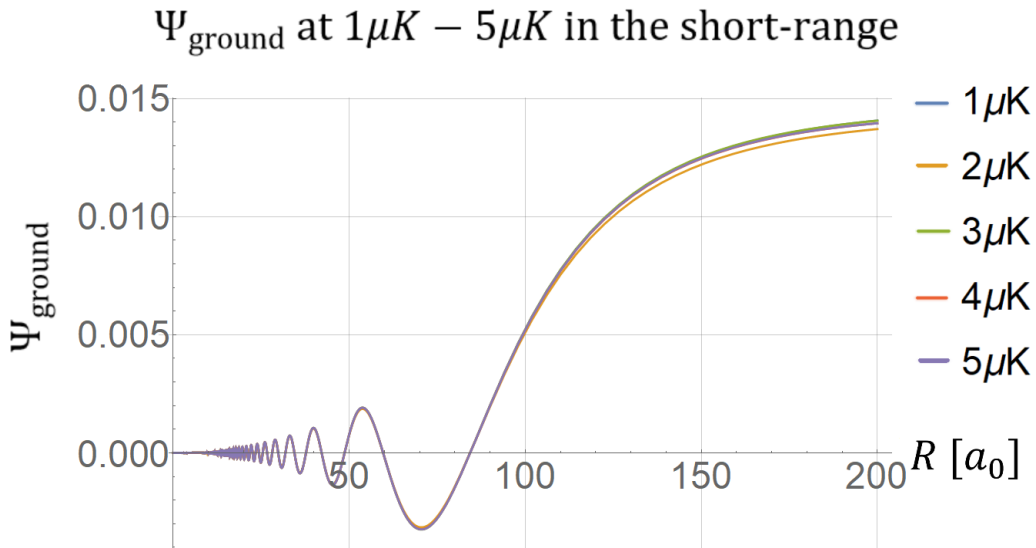
Figure 6.3: Short-range ground state wave function $\Psi_{\text{ground}}(R)$ until $r = 200\,a_0$ for energies of $1\,\mu K$, $2\,\mu K$ up to $5\,\mu K$. Plotted from $R = 0$ to $R = 8813\,a_0$.
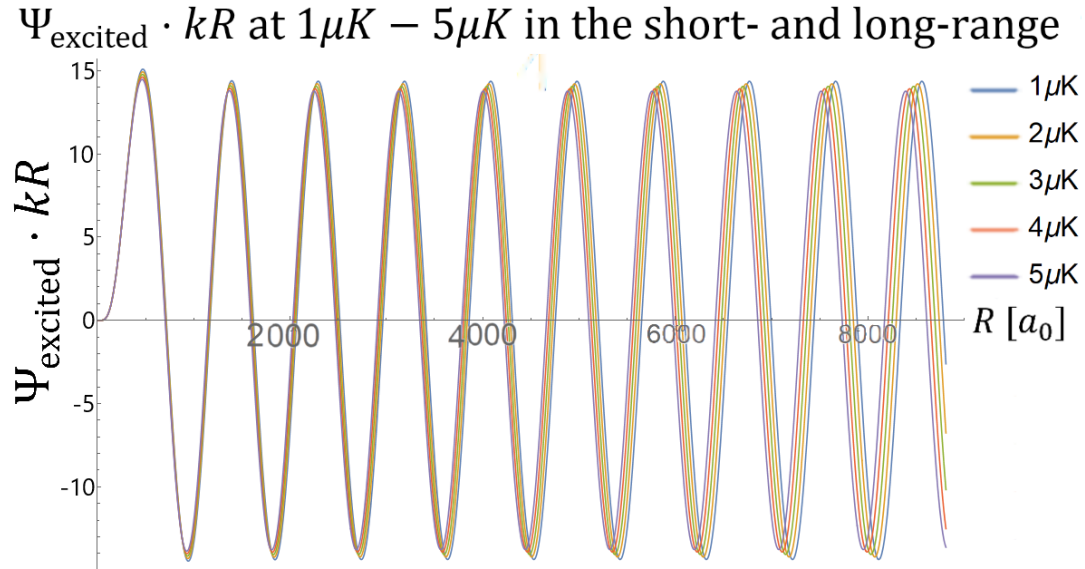
Figure 6.4: Excited state wave function $\Psi_{\text{excited}}(R) \cdot kR$ for the short- and long-range. Plotted from $R = 0$ to $R = 8813\,a_0$ for energies of $1\,\mu\text{K}$, $2\,\mu\text{K}$ up to $5\,\mu\text{K}$..
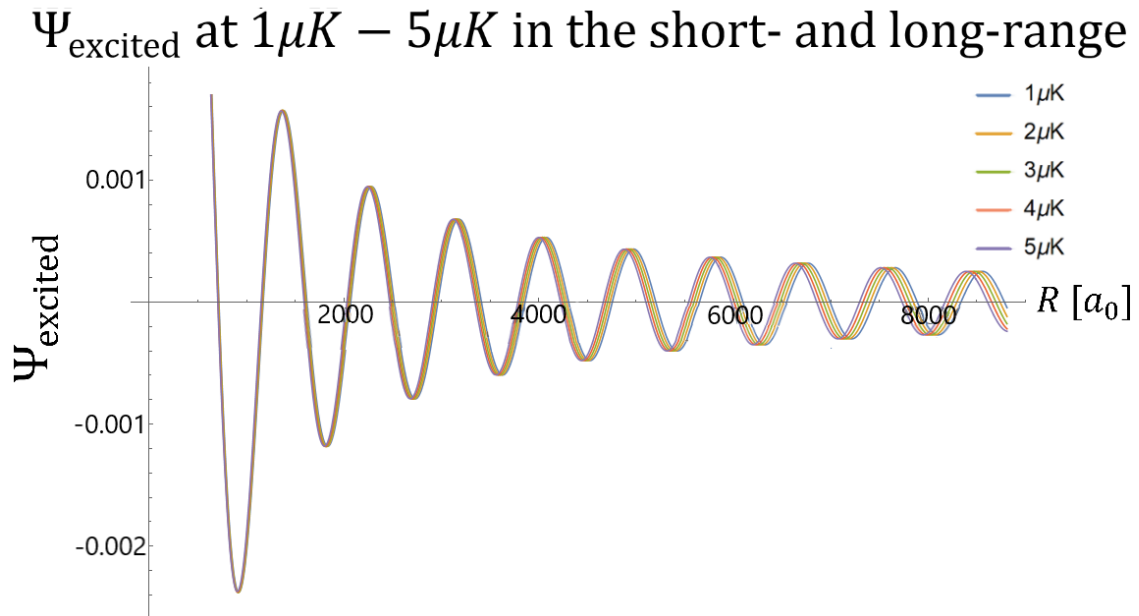
Figure 6.5: Normalized excited state wave function $\Psi_{\text{excited}}(R)$ for the short- and long-range. Plotted from $R = 0$ to $R = 8813\,a_0$ for energies of $1\,\mu\text{K}$, $2\,\mu\text{K}$ up to $5\,\mu\text{K}$..

To do this, first define the excited state energy as a function of the ground state energy and the detuning as

$$E_e(\delta) = E_g + \delta, \tag{6.2}$$

where E_g values are sampled from zero energy all the way up to $10\,\mu K$, the regime where the s-wave approximation is still valid as discussed in section 3.1. The samples are used to calculate the overlap for different ground state energies mimicking the Bose-Einstein distribution function. Later, these samples, representing possible ground state energies, have been interpolated in order to integrate over the whole ground state energy distribution defined by the Bose-Einstein distribution at $1\,\mu K$. When integrating over the possible energies, the Franck Condon integral part of equation (2.13) is given as a function of the detuning, as the energy of the excited state depends on the detuning. This detuning dependent excitations is what we defined as the trap loss.

In figure 6.6, the overlap has been plotted at zero detuning for simplicity. Also, only sample energies of $1\,\mu K$ and $2\,\mu K$ have been used to keep the plot clear. In the plot, the importance of the short-range is clearly visible, which is order of magnitude bigger than the long-range. Here, the yellow curve represents the overlap for energies of $1\,\mu K$ between the ground and excited state and the blue curve represents the overlap for an energy of $2\,\mu K$.
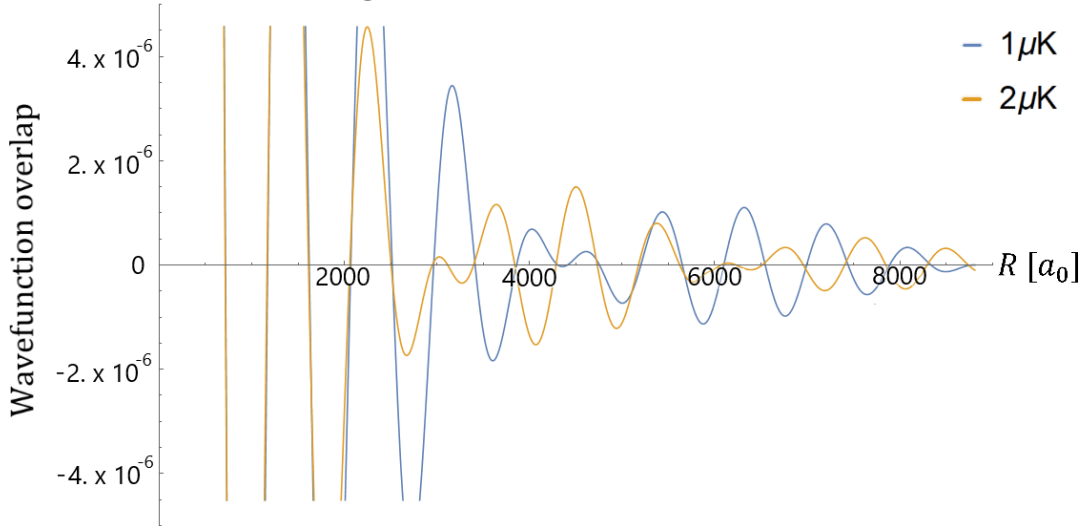
Figure 6.6: Overlap for $1\,\mu K$ represented in yellow and $2\,\mu K$ represented in blue. To get the wave function overlap, one can multiply the overlap by its conjugate and integrate over the space. Plotted from $r = 0$ to $r = 8813\,a_0$.

6.1.1 Trap loss calculations

In the previous result section we discussed the simulation and how it led to the trap loss profile. This trap loss profile was introduced in section 2.3 and is given by the formula (2.13)

$$\delta N = A'_N(\Delta) \int_{k_{\min}}^{\infty} P(T, E) F_{\mathrm{fi}}(k_{\mathrm{q}})\, dk_{\mathrm{q}}. \tag{6.3}$$

Here, $A'_N(\Delta)$ represents the the detuning dependent trap loss profile and the integral over all k-values represent all possible excitations probabilities. With this formula one can calculate the relative trap loss as function of the trap loss profile, the Bose-Einstein distribution and the Frank Condon overlap[20] given as (2.12)

$$F_{fi} = \left| \int_0^{\infty} \psi^-(r, E)\, \psi^+(r, E) \right|^2. \tag{6.4}$$

In this section the trap loss profile will be used to calculate the trap loss. This trap loss will be treated for three different cases in order to see the effects of changing this profile. For the first case, the assumption was made that the trap loss profile is not dependent on the detuning, meaning that every excitation will lead to trap loss for both particles. Then a hypothesized analytic solution will be shown, which is given by a simple polynomial function as a function of the detuning. Finally, the trap loss profile from the simulation will be used from section 5.1.4 to take real experimental measurements into account and to take into account the shape dependence of the tweezer trap together with the differential Stark shift.

Constant trap loss profile
By taking a constant trap loss profile, that is to say that the trap loss is not dependent on the detuning, a very easy result is obtained for the trap loss. In figure 6.7 the results can be seen for this constant trap loss, in which an optimum is found at zero detuning. This makes sense, since at zero detuning, the transition is resonant and most excitation to the excited state takes place. For higher detunings, the transition is more off-resonant, which leads to less trap loss.
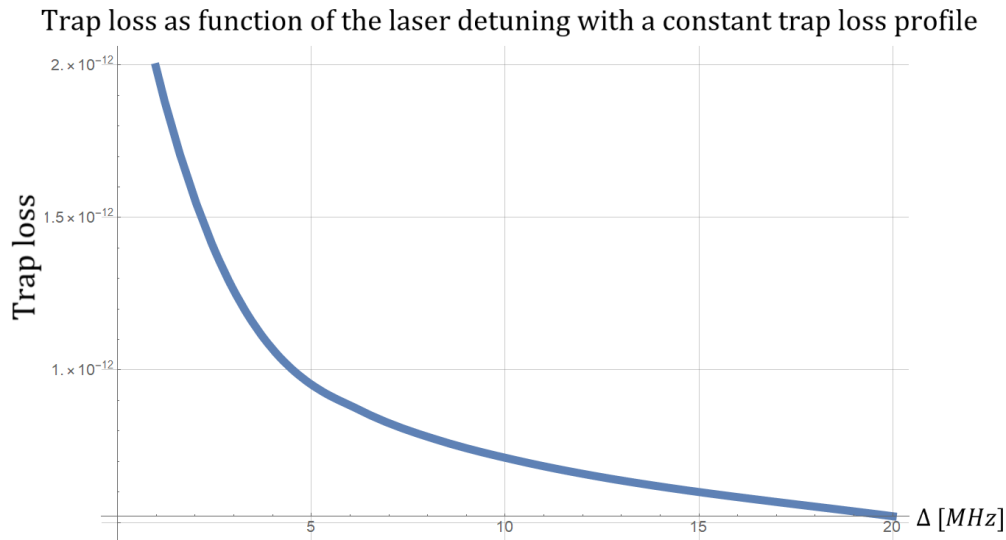
Figure 6.7: Trap losses for a constant trap loss profile plotted for δ between $0\,\mathrm{MHz}$ and $20\,\mathrm{MHz}$. An optimum is found at $\delta = 0$. On the y-axis the relative trap loss is given, meaning that mostly the shape and optimum detuning are interesting rather than the absolute values.

Analytic trap loss profile
In the previous section, it was discussed that the trap loss would be maximal at zero detuning, assuming that every excitation causes trap loss. However, at zero detuning, no extra energy is added to the particles from rolling down the repulsive dipole potential. To correctly calculate the trap loss, some energy gain profile depending on the detuning is needed. For this energy profile, three points can be made which predict the analytic profile, these point have already been discussed in section 4.2.1 and are related to the depth of the tweezer potential for atoms in the S state. At zero detuning, no losses are expected, since there is no energy gain during the collisions. At $\delta = 2.7\,\mathrm{MHz}$, on average 1 atom loss is expected, since both particles would gain half this energy which is just enough for just one particles to leave the trap given that the particles prior to the collision have an energy of half the trap depth on average, which has also been explained in section 4.2.1. To see this better, the statistical interpretation of figure 2.2 can be helpful, where both particles constantly gain and lose energy in a statistical manner. Till the point particles do not leave the trap they are on average around half the trap depth, supporting the claim. At $\delta = 5.3\,\mathrm{MHz}$, two particle losses are expected, since even if both particles started off with zero energy, still both particles get enough energy to be kicked out, causing two-body losses.

From these three linear data points, one can naively assume a linear trap loss profile going from $\delta = 0,$ trap loss $= 0$ to $\delta = 5.3\,\mathrm{MHz},$ trap loss $= 2$ also going through $\delta = 2.7\,\mathrm{MHz},$ trap loss $= 1.$ However, since there is a the statistical difference in energy of the particles before the collision, in combination with the effective cooling of the atoms, already effective one-body losses can be induced at detunings slightly higher than zero. The same argument can be made for detunings below $5.3\,\mathrm{MHz}$ as this will not directly cause two-body losses. The reason for both arguments is that it is very plausible that one of the atoms has a relatively low energy prior to the collision compared to the other, see section 2.2. Also, spontaneous emission of one of the colliding atom can kick the atom back into the trap. From these arguments an analytic trap loss profile has been hypothesized, which looks like

$$\text{trap loss}(\delta) = \frac{1}{5.3^3}(\delta - 5.3)^3 + 1, \tag{6.5}$$

where δ is given in MHz and the trap loss varies from 0 to 2 in the range from $0\,\mathrm{MHz}$ to $5.3\,\mathrm{MHz}.$ The resulting trap loss profile, following equation (2.13) as a function of the detuning, can be seen in figure 6.8. In this picture an optimum is calculated at $\delta = 1.76\,\mathrm{MHz},$ because at lower detunings the energy gain is not optimal and and for high detunings the wave function overlap and the Bose-Einstein distribution function are not optimal anymore.
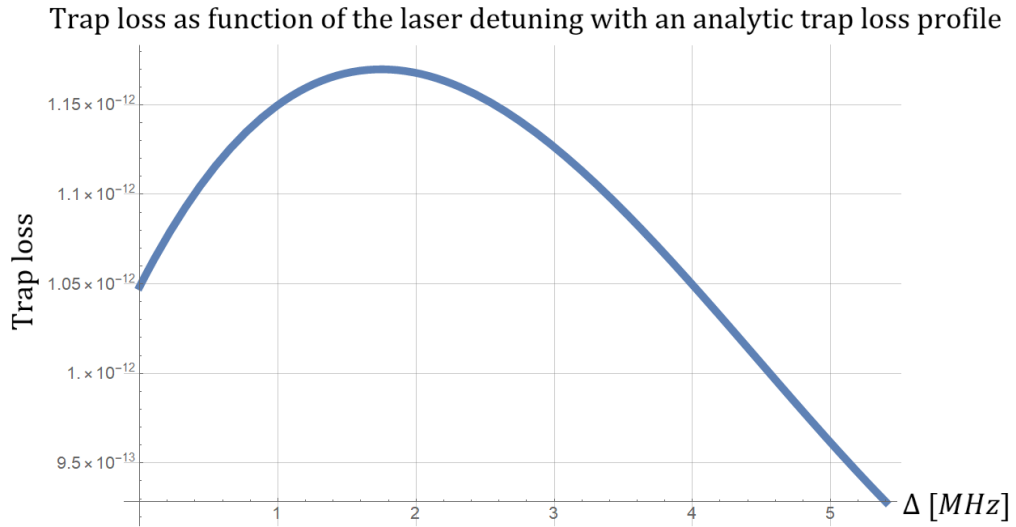
Figure 6.8: Trap losses for a analytic trap loss profile given by equation (6.5) plotted for δ between $0\,\mathrm{MHz}$ and $5.4\,\mathrm{MHz}.$ Here an optimum can be found at $\delta = 1.76\,\mathrm{MHz}.$ On the y-axis the relative trap loss is given, meaning that mostly the shape and optimum detuning are interesting rather than the absolute values.

Simulation trap loss profile

After the constant trap loss profile and the analytic profile, it is interesting to couple the simulation to the quantum calculations using the trap loss profile from the simulation. Here, the trap loss profile as explained in section 5.1.4 will be used. Since Rabi frequencies that are too high give chaotic behavior due to spontaneous emission events and much weaker Rabi frequencies give no opportunity to excite effectively, the optimum Rabi frequency of $1\,\mathrm{MHz}$ has been taken from table 5.9 and the energies corresponding to different detunings are listed in table 6.1.

Energy [μK]		Detuning δ				
		0 MHz	5 MHz	10 MHz	15 MHz	20 MHz
Rabi Ω	1 MHz	0.004 mK	0.043 mK	0.029 mK	0.010 mK	0.012 mK

Table 6.1: The difference of average energy of the one- and two-particle simulation runs during the 22 ms. Here a Rabi frequency of 1 MHz has been used with detunings δ between 0 MHz and 20 MHz. On the *y*-axis the relative trap loss is given, meaning that mostly the shape and optimum detuning are interesting rather than the absolute values.

This energy gain due to two-body collisions can now be used for the trap loss profile in equation (2.13). Multiplying the trap loss profile from the simulation by the wave function overlap and the Boltzmann distribution at 1 μK gives the atom loss as a function of the detuning, as can be seen in figure 6.9, where an optimum atom loss in the trap is predicted at $\delta = 2.5$ MHz. On the y-axis the relative trap loss has been plotted as this calculation does not tell us much about one-body losses over two-body losses. Therefore it is not of highest importance to scale the *y*-axis to experimental data, one might rather find the optimum detuning together with the optimum Rabi frequency and check the tweezer preparation efficiency.

Trap loss as function of the laser detuning with a simulation trap loss profile
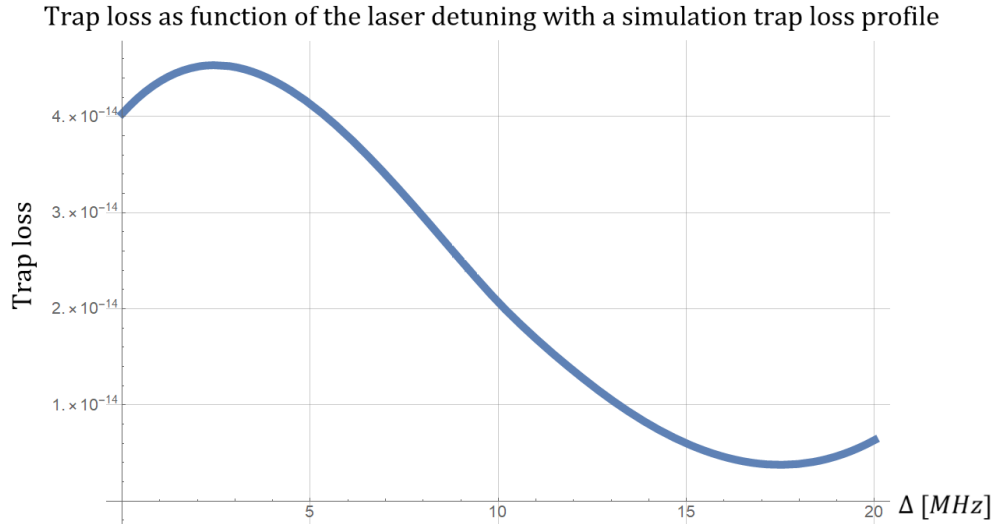
Figure 6.9: Trap losses using the simulation given by equation (6.5) plotted for δ between 0 MHz and 20 MHz. Here an optimum can be found at $\delta = 2.5$ MHz. For higher detunings there is a decline in atom loss all the way up to 17.5 MHz.

This relative trap loss, however, does not tell us much about the preparation efficiency. However, both the optimum detuning from the analytic trap loss as for the experimental trap loss fits the hypothesized one-body losses regime. This is still not enough information to make any significant claims, since the trap loss is a rate of loss, rather than telling us something about the dynamics and the ratio of one-body losses over two-body losses. To say something about this, one might refer back to the simulation results, which indicate that there should be an optimum when minimizing spontaneous emission effects, while still having effective excitation during the collision. This effective excitation can be done for Rabi frequencies around 1 MHz, while still having a low Rabi oscillation amplitude, which was introduced in section 2.5.1 as $\frac{\Omega^2}{\Omega^2+\delta^2}$. Meaning that for a higher frequency also a higher detuning has to be taken in order to keep this amplitude as low as possible.

Chapter 7

Conclusion and discussion

7.1 Conclusion

In this report, we looked at the most efficient way to induce one-body losses using light assisted collisions for strontium-88 atoms. This has been done with the goal to leave one atom per tweezer trap. This one atom could then be used to function as a qubit for quantum computations. When optimizing the one-body losses, a high preparation efficiency can be obtained, which will then make it more convenient to set up an array of interacting qubits[11]. In order to reach this high preparation efficiency we used Sr-88 atoms in a tweezer trap $120 \, \mu K$ deep. The atoms inside this trap would then collide with each other with the use of a collision laser. In this thesis, both a simulation and overlap calculation have been performed, which give insights into the two-body collisions of the particles for various Rabi frequencies and detunings of the collision laser. These two-body collisions will induce atom losses into the system as the energy per collision rises on average.

For the simulation, a trap loss profile, as function of the detuning has been found, which tells us about the energy gain per collision. Then, since the atoms in the simulations were still treated as semi-classical point particles and not enough statistical data could be gathered, only the trap loss profile has been abstracted from the simulation. This trap loss profile was then used as a factor in the quantum calculations.

However, an exact loading preparation efficiency has not been found, as both the simulation and the Franck-Condon calculation fail to calculate exactly the ratio of one-body losses over two-body losses. Rather, it explains the trap loss and the dynamics of the particles. Nevertheless, when discussing the dynamics of the particles already some predictions of one-body losses over two-body losses can be found for Sr-88 atoms in a $120 \, K$ deep tweezer trap. The trap loss tells us about the rate of loss but nothing about the ratio of the loss processes.

A summary of these findings are given below. First the interested regime is highlighted, coming from the simulation, in point one and two. Then, the optimum detuning is given for the quantum calculations, for both the simulation trap loss profile as the analytic trap loss profile, in point three and four. Finally, an important finding between the Rabi frequency and the detuning, which can be exploited using a cooling laser, is given in point five.

1. Rabi frequencies below $0.25 \, MHz$ do not positively contribute to any significant energy gain caused by light-assisted collisions. This is because the particles have no time to undergo half a Rabi oscillation in the time frame of the collision.

2. Rabi frequencies of $5 \, MHz$ or above heat up the atoms in the trap too much, causing no good energy difference prior to the collision. This happens because line broadening causes

all the transitions to be on resonance, causing all particles to heat up. Energy gain caused by collisions is more localized and causes a larger standard deviation of the energy.

3. This leaves us in the regime between $0.25\,\text{MHz}$ and $1\,\text{MHz}$ in which the particles interact on correct time scales and don't heat up too much. Here, $\Omega = 1\,\text{MHz}$ showed the best trap loss profile.

4. For the optimal Rabi frequency of $1\,\text{MHz}$ in the simulation, a maximum trap loss is predicted for $\delta = 2.5\,\text{MHz}$, whereas for the hypothesized analytic trap loss, this optimal detuning is lower, towards $1.76\,\text{MHz}$. The $\delta = 2.5\,\text{MHz}$ optimum is almost in the regime between one and two times the trap depth ($2.7\,\text{MHz}$ and $5.3\,\text{MHz}$). The $1.76\,\text{MHz}$ optimum is further below one time the trap depth. Both indicate that mostly one-body losses are expected, as for a particle with average energy half the trap energy would be just enough to leave the trap.

5. For the higher Rabi frequencies, higher detunings in the order of $10\,\text{MHz}$ are preferred, as indicated by the energy of the second particle once the the first one leaves the trap in table 5.7. This is because the amplitude of the Rabi oscillations (Ω^2/δ^2) should be small before the scattering process to gain optimal energy during the process. Higher Rabi frequencies could be very interesting with the use of cooling lasers resulting in a low average energy and a high localized energy gain between the particles.

7.2 Shortcomings of the simulation and quantum calculations

1. The simulation does not take into account the wave like nature of the particles, which has the consequence that energy can only be gained locally. For the quantum case, this would not be the case, as the collisions would induce a change of the velocity distribution, which is a more global approach.

2. No optical Bloch equations were implemented into the model, which made it harder to simulate the saturation of the two level system. Instead, a different discrete way of implementing the spontaneous emission was found using individual decay curves by sampling from an ensemble average and introducing an effective decay rate. This is useful for the simulation. However, one can also implement the optical Bloch equations and find another way to implement discrete kicks caused by spontaneous decay.

3. The statistics in the results should be built up by sampling multiple times, which makes the entire process computationally expensive (considering each run takes 1-2 days on a strong computer). This made it harder to check the real results.

4. Instead of varying the Rabi frequency of the laser, also the intensity could be varied in order to see more realistic values of the Rabi frequency. This would also be more useful to use for an experimentalist.

5. The quantum calculations do not explain one atom loss over two atom loss without the need of the trap loss profile from either the simulation or the analytic form.

6. The simulation did not take into account the cooling laser. This would have been interesting in order to analyze higher Rabi frequencies and higher detunings. This can be interesting since not all energy is gained optimally for a given detuning.

7. For the trap loss profile from the simulation, the difference in energy is taken between the one and two particle simulations. However, one should ideally multiply the one particle energy gain by 2, because this heating is felt on both particles individually during the two particle simulation. This could not be done, since it would have given negative values. Instead, it is assumed that the relative energy gain is important, since the two particles in the simulation lose energy by colliding into each other from the repulsive dipole potential, which makes formula 5.2 a lot harder.

7.3 Future research

In the future, many interesting features can be added to the model and the simulation. For the simulation, many more variables can be changed, such as the trap depth, the starting number of atoms and a cooling factor, for example. Each of them would give their own insights of how to balance the dynamics of the particles with the internal state of those same particles. Also, the coding itself could be changed if one would introduce the OBE into the simulation and find another way to implement the spontaneous decay kicks. This would lead to a description that is more accurate and more related to the experimental variables such as the intensity and the saturation parameters. One way to make the simulation more interesting is by implementing the full quantum picture, such that wave functions at all time steps are calculated. This would combine Einstein's rate equations to the OBE, and ultimately connect them to the experimental parameters. Finally, one can change the excited state potential to the attractive P state where $m_J = 0$. This has its own advantages and disadvantages, but can be beneficial in some cases.

For the quantum wave functions and the trap loss profile, a lot of interesting research can be done, starting with making the potential of the tweezer trap more realistic and not assuming an infinite well at the boundaries. This would create more possibilities of actual trap loss, since the particles

have a chance of tunneling outside of the tweezer trap.

In the future, this simulation can be used to test all light assisted collisions, and make working in the lab a lot easier. It also presents a way to compute the dynamics of the system in a direct and intuitive way.

Bibliography

[1] R. Landauer, "Information is physical," *Physics Today*, vol. 44, no. 5, pp. 23–29, 1976. 1

[2] J. A. Piotrowski and I. Technology, "Buildin a Model of a Useful Turing Machine," vol. 01221, no. 99, 2000. 1

[3] T. Hey, "Quantum computing: An introduction," *Computing and Control Engineering Journal*, vol. 10, no. 3, pp. 105–112, 1999. 1

[4] H. Perrin, P. Lemonde, F. Pereira dos Santos, V. Josse, B. Laburthe Tolra, F. Chevy, and D. Comparat, "Application of lasers to ultra-cold atoms and molecules," *Comptes Rendus Physique*, vol. 12, no. 4, pp. 417–432, 2011. 1

[5] K. Kowalski, V. Cao Long, K. Dinh Xuan, M. Głódź, B. Nguyen Huy, and J. Szonert, "Magneto-optical Trap: Fundamentals and Realization," *Computational Methods in Science and Technology*, vol. Special Is, no. 02, pp. 115–129, 2010. 1

[6] M. Morgado and S. Whitlock, "Quantum simulation and computing with Rydberg-interacting qubits," *AVS Quantum Science*, vol. 3, no. 2, 2021. 1, 2

[7] A. Montanaro, "Quantum algorithms: An overview," *npj Quantum Information*, vol. 2, no. 1, pp. 1–8, 2016. 1, 2

[8] P. Scholl, M. Schuler, H. J. Williams, A. A. Eberharter, D. Barredo, K. N. Schymik, V. Lienhard, L. P. Henry, T. C. Lang, T. Lahaye, A. M. Läuchli, and A. Browaeys, "Quantum simulation of 2D antiferromagnets with hundreds of Rydberg atoms," *Nature*, vol. 595, no. 7866, pp. 233–238, 2021. 2

[9] S. Ebadi, T. T. Wang, H. Levine, A. Keesling, G. Semeghini, A. Omran, D. Bluvstein, R. Samajdar, H. Pichler, W. W. Ho, S. Choi, S. Sachdev, M. Greiner, V. Vuletić, and M. D. Lukin, "Quantum phases of matter on a 256-atom programmable quantum simulator," *Nature*, vol. 595, no. 7866, pp. 227–232, 2021. 2

[10] I. Cong, H. Levine, A. Keesling, D. Bluvstein, S.-T. Wang, and M. D. Lukin, "Hardware-Efficient, Fault-Tolerant Quantum Computation with Rydberg Atoms," *Physical Review X*, vol. 12, no. 2, p. 21049, 2021. 2

[11] A. Urech, I. H. A. Knottnerus, R. J. C. Spreeuw, and F. Schreck, "Narrow-line imaging of single strontium atoms in shallow optical tweezers," pp. 1–11, 2022. 2, 24, 25, 30, 63

[12] Y. H. Fung, "Near-deterministic preparation of single atoms and Raman sideband cooling," no. May, 2016. 3, 8, 9, 15

[13] D. Barredo, V. Lienhard, T. Lahaye, and A. Browaeys, "An atom-by-atom assembler of defect-free arbitrary 2d atomic arrays," vol. 1, pp. 1–7, 2016. 4, 43

[14] K. N. Schymik, V. Lienhard, D. Barredo, P. Scholl, H. Williams, A. Browaeys, and T. Lahaye, "Enhanced atom-by-atom assembly of arbitrary tweezer arrays," *Physical Review A*, vol. 102, no. 6, pp. 1–10, 2020. 4

[15] I. R. Afnan and A. W. Thomas, "Introduction to two- and three-body scattering theory," *Flinders Univ. of South Australia, Bedford Park. Inst. for Atomic Studies*, vol. 8, no. 7, p. 80, 1976. 7

[16] A. C. Ipsen and K. Splittorff, "The van der Waals interaction in one, two, and three dimensions," *American Journal of Physics*, vol. 83, no. 2, pp. 150–155, 2015. 7

[17] T. Grünzweig, A. Hilliard, M. McGovern, and M. F. Andersen, "Near-deterministic preparation of a single atom in an optical microtrap," *Nature Physics*, vol. 6, no. 12, pp. 951–954, 2010. 8

[18] J. Kraats, "Van der Waals landscape of the effective Efimovian three-body potential from the broad to narrow Feshbach resonance limit," 2021. 9, 13, 15

[19] D. J. Ahmed-Braun, K. G. Jackson, S. Smale, C. J. Dale, B. A. Olsen, S. J. Kokkelmans, P. S. Julienne, and J. H. Thywissen, "Probing open- And closed-channel -wave resonances," *Physical Review Research*, vol. 3, no. 3, pp. 1–21, 2021. 10, 11, 28

[20] M. Schulz, "Tightly confined atoms in optical dipole traps," *Innsbruck*, p. 177, 2002. 11, 23, 24, 25, 26, 59

[21] C. Desgranges and J. Delhommelle, *Introduction to Quantum Mechanics*. 2020. 13, 15, 16, 36, 72, 74, 76, 77, 78, 79, 84, 86

[22] Ohio state university, "M1b. Scattering Theory 1," *Lecture notes*, vol. 1, no. 1, pp. 1–17, 2014. 13

[23] J. J. Sakurai and J. Napolitano, *Sakuraii-Modern Quantum Mechanics*. 2010. 14, 35

[24] O. Benson, "Interaction of Atoms With a Classical Light Field (Quantenoptik Chapter 7)," no. 258, pp. 74–89, 2008. 16, 79

[25] W.Ketterle, "Atom Light," *Spring*, p. 23, 2000. 16, 80

[26] S. L. G. Wieman and C. E., *Advanced Optics Laboratory Laser Cooling and Trapping*, vol. 4. 1993. 16, 17, 18, 31, 80, 81, 82, 83

[27] N. Šibalić, J. D. Pritchard, C. S. Adams, and K. J. Weatherill, "ARC: An open-source library for calculating properties of alkali Rydberg atoms," *Computer Physics Communications*, vol. 220, pp. 319–331, 2017. 18, 33, 84

[28] A. Heinz, A. J. Park, N. Šantić, J. Trautmann, S. G. Porsev, M. S. Safronova, I. Bloch, and S. Blatt, "State-Dependent Optical Lattices for the Strontium Optical Qubit," *Physical Review Letters*, vol. 124, no. 20, pp. 1–7, 2020. 19

[29] Y. Tan, F. Chen, J. R. Vázquez de Aldana, H. Yu, and H. Zhang, "Tri-wavelength laser generation based on neodymium doped disordered crystal waveguide," *Optics Express*, vol. 21, no. 19, p. 22263, 2013. 19

[30] M. M. Boyd, "High Precision Spectroscopy of Strontium in an Optical Lattice: Towards a New Standard for Frequency and Time," *PhD thesis*, p. 245, 2007. 19, 24, 31

[31] J. Yang, X. He, R. Guo, P. Xu, K. Wang, C. Sheng, M. Liu, J. Wang, A. Derevianko, and M. Zhan, "Coherence Preservation of a Single Neutral Atom Qubit Transferred between Magic-Intensity Optical Traps," *Physical Review Letters*, vol. 117, no. 12, pp. 1–6, 2016. 19

[32] J. Weiner, V. S. Bagnato, S. Zilio, and P. S. Julienne, "Experiments and theory in cold and ultracold collisions," *Reviews of Modern Physics*, vol. 71, no. 1, pp. 1–85, 1999. 20

[33] F. Sorrentino, G. Ferrari, N. Poli, R. Drullinger, and G. M. Tino, "Laser cooling and trapping of atomic strontium for ultracold atoms physics, high-precision spectroscopy and quantum sensors," *Modern Physics Letters B*, vol. 20, no. 21, pp. 1287–1320, 2006. 21, 23

[34] S. Kotochigova, "Relativistic electronic structure of the Sr2 molecule," *Journal of Chemical Physics*, vol. 128, no. 2, 2008. 21, 38

[35] O. Onishchenko, *Ultracold atomic gases of strontium : production and narrow-line spectroscopy*. 2020. 22

[36] S. Stellmer, F. Schreck, and T. C. Killian, "Degenerate Quantum Gases of Strontium," pp. 1–80, 2014. 22

[37] S. D. Sheet, S. Carbonate, and E. S. Carbonate, "Safety Data Sheet for Strontium Carbonate, Enriched Strontium Carbonate," pp. 1–9, 2019. 22

[38] J. E. Sansonetti and G. Nave, "Wavelengths, transition probabilities, and energy levels for the spectrum of neutral strontium (SrI)," *Journal of Physical and Chemical Reference Data*, vol. 39, no. 3, 2010. 22

[39] X. Xu, T. H. Loftus, J. L. Hall, A. Gallagher, and J. Ye, "Cooling and trapping of atomic strontium," *Journal of the Optical Society of America B*, vol. 20, no. 5, p. 968, 2003. 25

[40] T. Verboven, "Magneto-Optical Trap Optimization," *Thesis*, 2013. 25

[41] V. M. Initiative and B. Rosenfeld, "Sum of the Terms of a Binomial Distribution.," pp. 1–4, 1800. 29

[42] S. Sahu and M. A. Rama, "Microstates of systems obeying Maxwell-Boltzmann distribution, a limiting case of Quantum Statistics!," *IOSR Journal of Applied Physics*, vol. 6, no. 5, pp. 51–55, 2014. 29

[43] W. Hörmann, "The transformed rejection method for generating Poisson random variables," *Insurance Mathematics and Economics*, vol. 12, no. 1, pp. 39–45, 1993. 29

[44] I. S. Oliveira, T. J. Bonagamba, R. S. Sarthour, J. C. Freitas, and E. R. DeAzevedo, "Fundamentals of Quantum Computation and Quantum Information," *NMR Quantum Information Processing*, pp. 93–136, 2007. 29

[45] A. S. Carasso, "Stabilized Richardson leapfrog scheme in explicit stepwise computation of forward or backward nonlinear parabolic equations," *Inverse Problems in Science and Engineering*, vol. 25, no. 12, pp. 1719–1742, 2017. 30

[46] D. D. Nolte, "The fall and rise of the Doppler effect," *Physics Today*, vol. 73, no. 3, pp. 30–35, 2020. 32

[47] E. J. Robertson, N. Šibalić, R. M. Potvliege, and M. P. Jones, "ARC 3.0: An expanded Python toolbox for atomic physics calculations," *Computer Physics Communications*, vol. 261, p. 107814, 2021. 33, 83

[48] E. Hairer and G. Wanner, "Encyclopedia of Applied and Computational Mathematics," *Encyclopedia of Applied and Computational Mathematics*, no. September, 2015. 33

[49] J. C. Butcher, "Practical rungekutta methods for scientific computation," *ANZIAM Journal*, vol. 50, no. 3, pp. 333–342, 2009. 34

[50] P. A. M. Dirac, "The Quantum Theory of the Emission and Absorption of Radiation," *Special Relativity and Quantum Theory*, pp. 157–179, 1988. 36

[51] T. Radja and Bojana, "Temperature and Molecular Motion," *Uplift Education*, pp. 1–5, 2019. 41

[52] O. A. M. A. H Kara, *Atoms, Molecules and Large Systems*, vol. 7. 2014. 55

[53] P. S. Julienne, "Cold binary atomic collisions in a light field," *Journal of Research of the National Institute of Standards and Technology*, vol. 101, no. 4, pp. 487–503, 1996. 71, 72

[54] G. D. Mahan, "Scattering Theory," *Quantum Mechanics in a Nutshell*, vol. 2, pp. 320–351, 2019. 73

[55] T. Karman, L. M. Janssen, R. Sprenkels, and G. C. Groenenboom, "A renormalized potential-following propagation algorithm for solving the coupled-channels equations," *Journal of Chemical Physics*, vol. 141, no. 6, 2014. 75

Appendix A

Theoretical derivations

A.1 Semi-classical to quantum wave function overlap

Using the semi-classically Condon point described in the section 2.1, one can calculate the overlap at this point. However, it should ultimately be calculated quantum mechanically to give proper insights into the system, accounting for the delocalization of the wave function. The probability of a transition with laser light ω and an energy difference E is proportional to a Frank-Condon overlap matrix element between the ground- and excited state wave functions as

$$P_{ge}(E,\omega) \propto |\langle \Psi_e(R)| \Omega_{eg}(R) |\Psi_g(E,R)\rangle|^2 \tag{A.1}$$

$$\approx |\Omega_{eg}(R_C)|^2 |\langle \Psi_e(R)|\Psi_g(E,R)\rangle|^2, \tag{A.2}$$

where $\Omega_{eg}(R)$ is the optical Rabi matrix element representing the strength of the optical coupling. This so called Frank-Condon factor can be approximated along the Condon point using a reflection approximation and applies over a large range of energies, including the red and blue detuning. The approximation is closely related to the usual stationary phase approximation of line broadening theory. Using this approximation, the Franck-Condon factor is proportional to the ground-state wave function at the Condon point as

$$F_{ge}(E,\Delta) = |\langle \Psi_e(R)|\Psi_g(E,R))\rangle|^2 \tag{A.3}$$

$$= \frac{1}{D_C}|\Psi_g(E,R_C)|^2 \qquad \text{for blue detuning.} \tag{A.4}$$

$$= hv_v \frac{1}{D_C}|\Psi_g(E,R_C)|^2 \qquad \text{for red detuning.} \tag{A.5}$$

Here $D_C = |d(V_e - V_g)/dR|_{R_C}$ is the slope of the difference potential[53].

A.2 Lippmann-Schwinger equation

In order to explain two body scattering collisions on the quantum scale one needs to consider first the time independent Schrodinger's equation:

$$\left[-\frac{\hbar^2}{2\mu}\nabla^2 + V(r)\right]\psi(\mathbf{r}) = E\psi(\mathbf{r}) \tag{A.6}$$

where $\mu = (m_1 m_2)/(m_1 + m_2)$ is the reduced mass of the system. Here, the assumption is made that the interactions between the two particles are translationally invariant, which is the case if and only if the internal Hamiltonian only depends on the internal state of the particles and not on the spatial coordinate. For these kind of systems it is useful to use a center of mass frame in

which $\vec{K} = \vec{k_1} + \vec{k_2}$ can be set to zero. Writing $H_0 = \vec{p}^2/2\mu$ for the non relativistic kinetic energy operator with an eigenstate $|\phi\rangle$ yields

$$H_0|\phi\rangle = E|\phi\rangle, \tag{A.7}$$

where E represents the energy in asymptotic regime. One can write the the total time independent Schrodinger equation in matrix form as

$$(H_0 + V)|\psi\rangle = E|\psi\rangle, \tag{A.8}$$

where V represents the interaction potential. Rearranging this equation gives

$$|\psi\rangle = |\phi\rangle + \frac{1}{E - H_0}V|\psi\rangle, \tag{A.9}$$

where $|\phi\rangle$ are the plane wave solutions added, which would also exist without an interaction potential. Since the inverse quantum operator $(E - H_0)^{-1}$ can be singular, because the eigenvalues of H_0 can be zero, it is useful to introduce an imaginary factor $i\epsilon$ and by taking the limit $\epsilon \to 0^+$. This would then give the Lippman-Schwinger equation as[53]

$$|\psi\rangle = |\phi\rangle + \frac{1}{E - H_0 + i\epsilon}V|\psi\rangle. \tag{A.10}$$

A.3 Green's function

In order to write the Lippmann-Schwinger equation in integral form it is useful to define the Green's operator. This greens operator obeys the equation [21]

$$\left(E + \frac{\hbar^2}{2m}\nabla^2\right)G_0\left(E; \mathbf{r}, \mathbf{r}'\right) = \delta\left(\mathbf{r} - \mathbf{r}'\right). \tag{A.11}$$

This equation can be seen as the solution of the Schrodinger's equation with a source given by the delta function $\delta\left(\mathbf{r} - \mathbf{r}'\right)$. Equation $A.11$ can be rewritten in the Helmholtz equation as

$$\left(\nabla^2 + k^2\right)G_0\left(k; \mathbf{r}, \mathbf{r}'\right) = \frac{2m}{\hbar^2}\delta\left(\mathbf{r} - \mathbf{r}'\right), \tag{A.12}$$

where the famous energy equation

$$E = \frac{\hbar^2 k^2}{2m}, \tag{A.13}$$

has been used to rewrite the Helmholtz equation in terms of the wave vector. Then, by defining the Fourier transform of the Green's function as

$$\tilde{G}_0(k; \mathbf{q}) = \int d^3x e^{-i\mathbf{q}\cdot\mathbf{x}}G_0(k; \mathbf{x}) \quad \Rightarrow \quad G_0(k; \mathbf{x}) = \int \frac{d^3q}{(2\pi)^3}e^{i\mathbf{q}\cdot\mathbf{x}}\tilde{G}_0(k; \mathbf{q}), \tag{A.14}$$

one can rewrite the Helmholtz function in momentum space as

$$\left(-q^2 + k^2\right)\tilde{G}(k; \mathbf{q}) = \frac{2m}{\hbar^2} \quad \Rightarrow \quad \tilde{G}_0(k; \mathbf{q}) = -\frac{2m}{\hbar^2}\frac{1}{q^2 - k^2}, \tag{A.15}$$

which can be inverted back to the position basis using the inverse Fourier transformation, also given by equation (A.14), which results in

$$G_0(k; \mathbf{x}) = -\frac{2m}{\hbar^2}\int \frac{d^3q}{(2\pi)^3}\frac{e^{i\mathbf{q}\cdot\mathbf{x}}}{q^2 - k^2}. \tag{A.16}$$

Since this integral diverges for $q^2 = k^2$, also here an imaginary factor $i\epsilon$ has to be implemented, resulting in

$$G_0^+(k; \mathbf{x}) = -\frac{2m}{\hbar^2} \int \frac{d^3q}{(2\pi)^3} \frac{e^{i\mathbf{q}\cdot\mathbf{x}}}{q^2 - k^2 - i\epsilon}, \tag{A.17}$$

and finally take the limit $\epsilon \to 0^+$. To solve this integral, one should switch to a polar coordinate system to rewrite the equation as

$$
\begin{aligned}
G_0^+(k; \mathbf{x}) &= -\frac{2m}{\hbar^2} \frac{1}{(2\pi)^3} \int_0^{2\pi} d\phi \int_{-1}^{+1} d(\cos\theta) \int_0^\infty dq \frac{q^2 e^{iqx\cos\theta}}{q^2 - k^2 - i\epsilon} \\
&= -\frac{2m}{\hbar^2} \frac{1}{(2\pi)^2} \int_0^\infty dq \frac{q}{ix} \frac{e^{iqx} - e^{-iqx}}{q^2 - k^2 - i\epsilon} \\
&= -\frac{2m}{\hbar^2} \frac{1}{(2\pi)^2} \frac{1}{ix} \int_{-\infty}^\infty dq \frac{q e^{iqx}}{(q - k - i\epsilon)(q + k + i\epsilon)}
\end{aligned}
\tag{A.18}
$$

ultimately leading to the Cauchy's integral formulas. This formula can be solved using a contour integral in the positive x-plane. Since x is positive, this results in an extra factor i^{ikr}, leading to the final answer

$$G_0^+(k; \mathbf{r} - \mathbf{r}') = -\frac{2m}{\hbar^2} \frac{1}{4\pi} \frac{e^{+ik|\mathbf{r}-\mathbf{r}'|}}{|\mathbf{r} - \mathbf{r}'|}. \tag{A.19}$$

For this derivation the imaginary factor $+i\epsilon$ has been chosen rather than $-i\epsilon$. Similarly, G_0^- would have been found as

$$G_0^+(k; \mathbf{r} - \mathbf{r}') = -\frac{2m}{\hbar^2} \frac{1}{4\pi} \frac{e^{-ik|\mathbf{r}-\mathbf{r}'|}}{|\mathbf{r} - \mathbf{r}'|}, \tag{A.20}$$

with the only difference being the sign change in the exponent, representing either in- or outgoing scattering waves. Since scattering waves can only go outwards, our choice for using $-i\epsilon$ seems quite reasonable.

A.4 Integral formulation Lippmann-Schwinger equation and the Born approximation

Taking equation (A.10) and using the Green's operator for the wave function for a delta function potential, one can expand this theorem for an arbitrary potential $V(r')$ where r' represents the position variable over which the potential has to be integrated. If now plane wave solutions for the non interaction Hamiltonian equation are given as [54]

$$\phi(\mathbf{r}) = e^{i\mathbf{k}\cdot\mathbf{r}}, \tag{A.21}$$

the Lippmann-Schwinger equation can formulated as

$$\psi(k; \mathbf{r}) = e^{i\mathbf{k}\cdot\mathbf{r}} - \frac{2m}{\hbar^2} \int d^3r' \frac{e^{+ik|\mathbf{r}-\mathbf{r}'|}}{4\pi |\mathbf{r} - \mathbf{r}'|} V(\mathbf{r}') \psi(k; \mathbf{r}'), \tag{A.22}$$

which has a very natural interpretation . Here, the first term represents the incoming wave with momentum $\hbar\vec{k}$ and second term is the scattered outgoing wave. Since this integral formulation of the Lippmann-Schwinger equation is still implicit, that is to say that the total wave function still depends on the wave function itself for the scattered part, it is useful to introduce the born approximation. For this, it is assumed that $V(r')$ is non-zero only in a finite region, which of course will be approximately be the case for interaction potentials, which decay as $1/r^3$. For large r, which is to say that

$$|\mathbf{r} - \mathbf{r}'| = \sqrt{r^2 - 2\mathbf{r}\cdot\mathbf{r}' + r'^2} \approx r - \frac{\mathbf{r}\cdot\mathbf{r}'}{r}, \tag{A.23}$$

This will then transform the Green's operator, equation (A.11), as

$$G_0^+ \left(k; \mathbf{r} - \mathbf{r}' \right) \approx -\frac{2m}{\hbar^2} \frac{1}{4\pi} \frac{e^{+ikr}}{r} e^{-ik\hat{\mathbf{r}} \cdot \mathbf{r}'}, \tag{A.24}$$

and finally transforming the Lippmann-Schwinger equation as

$$\psi(k; \mathbf{r}) \sim e^{i\mathbf{k} \cdot \mathbf{r}} - \frac{2m}{\hbar^2} \frac{1}{4\pi} \left[\int d^3 r' e^{-ik\hat{\mathbf{r}} \cdot \mathbf{r}'} V\left(\mathbf{r}' \right) \psi\left(k; \mathbf{r}' \right) \right] \frac{e^{ikr}}{r}, \tag{A.25}$$

which has the form of

$$\psi(\mathbf{r}) \sim e^{ikz} + f(\theta, \phi) \frac{e^{ikr}}{r}, \tag{A.26}$$

where $f(\theta, \phi)$ is defined to be the scattering amplitude as

$$f(\theta, \phi) = -\frac{2m}{\hbar^2} \frac{1}{4\pi} \int d^3 r' e^{-ik\hat{r} \cdot \mathbf{r}'} V\left(\mathbf{r}' \right) \psi\left(k; \mathbf{r}' \right). \tag{A.27}$$

As we will see in chapter A.5 the form of equation (A.26) will be used as reference for the derivation in order to calculate the phase shift ultimately.

A.5   Partial wave analysis

In this approach, also the Schrödinger's equation will be solved, now explicitly as a function of the angular momentum l, which is convenient since most scattering problems are solved in a potential only depending on the radial coordinate, leading to spherically symmetric scattering states as solutions. Using this formalism [21], the wave function will be written using the separation of variables technique as

$$\psi(r, \theta, \phi) = R(r) Y_l^m(\theta, \phi) \tag{A.28}$$

with a radial wave function $R(r)$ and an angular part $Y_l^m(\theta, \phi)$ known as the spherical harmonics. Introducing $u(r) = rR(r)$, this leads to the rewritten radial Schrodinger's equation as

$$-\frac{\hbar^2}{2m} \frac{d^2 u}{dr^2} + \left[V(r) + \frac{\hbar^2}{2m} \frac{l(l+1)}{r^2} \right] u = Eu. \tag{A.29}$$

Since for our problem it is only of interest to look for very large r, that is to say for $kr \gg 1$ in the radiation zone, the potential can be set to zero. This has also been done in section A.4 and is very accurate for potentials where $V(r) \sim 1/r^n$ with $n \geq 2$. This approximation is called the finite potential approximation. Without potential the radial Schrödinger equation reads

$$\frac{d^2 u}{dr^2} - \frac{l(l+1)}{r^2} u = -k^2 u, \tag{A.30}$$

where $k = \sqrt{2mE}/\hbar$ is defined as usual. Solutions of this equation are given as a linear combination of spherical Bessel functions as

$$u(r) = Arj_l(kr) + Brn_l(kr). \tag{A.31}$$

However, these functions do not behave as would be optimal for this formalism since neither functions behave as e^{ikr} or e^{-ikr} representing the incoming and outgoing scattering waves. Rather the functions behave as sine or cosine functions. Nevertheless, the spherical Bessel functions can be rewritten, using Euler's identity, to the spherical Hankel functions as

$$h_l^{(1)}(x) \equiv j_l(x) + in_l(x); \quad h_l^{(2)}(x) \equiv j_l(x) - in_l(x), \tag{A.32}$$

which behave as scattering states with a familiar form. In the limit for large r values, the Hankel functions of the first kind scale as e^{ikr}/r and the Hankel functions of the second kind scale as

e^{-ikr}/r.

For outgoing states, we can evidently write the radial wave function solution in the radiation zone as

$$R(r) = C h_l^{(1)}(kr). \tag{A.33}$$

Leading to the total wave function with the same form as has been seen in equation of A.26 for the Bohr approximation formalism as

$$\psi(r, \theta, \phi) = A \left\{ e^{ikz} + \sum_{l,m} C_{l,m} h_l^{(1)}(kr) Y_l^m(\theta, \phi) \right\}. \tag{A.34}$$

Now, as mentioned before, since the potentials are spherically symmetric, the outgoing wave function cannot depend on ϕ. So only terms with $m = 0$ survive. This will simplify the expression for the angular part as

$$Y_l^0(\theta, \phi) = \sqrt{\frac{2l+1}{4\pi}} P_l(\cos \theta), \tag{A.35}$$

where P_l is the l-th Legendre Polynomial. The final wave function can now be written down as

$$\psi(r, \theta) = A \left\{ e^{ikz} + k \sum_{\ell=0}^{\infty} i^{\ell+1} (2\ell + 1) a_\ell h_\ell^{(1)}(kr) P_\ell(\cos \theta) \right\}, \tag{A.36}$$

where the expansion coefficients $C_{l,0}$ are defined as $i^{l+1} k \sqrt{4 * pi (2l + 1)} a_l$, where a_l are called the l-th partial wave amplitude. Since for large r the Hankel function of the first kind goes as $(-i)^{l+1} e^{ikr}/kr$ one could also write the wave function in the same form as has been seen before in the chapter A.4 and confirms the total wave function as

$$\Psi(r, \Theta) \approx A \left\{ e^{ikz} + f(\Theta) \frac{e^{ikr}}{r} \right\}, \tag{A.37}$$

where

$$f(\Theta) = \sum_{l=0}^{\infty} (2l + 1) a_l P_l(cos\Theta). \tag{A.38}$$

Here, two coordinates are used, namely r and z, which normally don't go together very well. For this, the plane wave solutions - the first part of equation (A.37) - can be rewritten using Rayleigh's formula as

$$e^{ikz} = \sum_{l=0}^{\infty} i^l (2l + 1) j_l(kr) P_l(cos\Theta). \tag{A.39}$$

Ultimately leading to the total scattered wave function in the partial wave framework as

$$\psi(r, \theta) = A \sum^{\infty} i^\ell (2\ell + 1) \left[j_\ell(kr) + ik a_\ell h_\ell^{(1)}(kr) \right] P_\ell(\cos \theta). \tag{A.40}$$

A.6 Excited state wave function using finite difference approach

The time independent Schrodinger's equation reads

$$-\frac{\hbar^2}{2\mu} \frac{\partial^2}{\partial r^2} |\Psi\rangle = (E - V) |\Psi\rangle, \tag{A.41}$$

which can be rewritten in a fourth order finite difference scheme as[55]

$$\frac{1}{a^2} \left(\frac{15}{4} \Psi_n - \frac{77}{6} \Psi_{n+1} + \frac{107}{6} \Psi_{n+2} - 13 \Psi_{n+3} + \frac{61}{12} \Psi_{n+4} - \frac{5}{6} \Psi_{n+5} \right) = -\frac{2\mu}{\hbar^2} (E - V_n) \Psi_n = -k_n^2 \Psi_n, \tag{A.42}$$

where $k_n = \frac{\sqrt{2\mu(E-V_n)}}{\hbar}$ and a is the step size for this scheme. The fourth order different scheme implies that the error of each step scales with the step size to the power of four. To calculate the steps backwards, one can rewrite equation (A.42) for Ψ_n as

$$\Psi_n = (\frac{77}{6}\Psi_{n+1} - \frac{107}{6}\Psi_{n+2} + 13\Psi_{n+3} - \frac{61}{12}\Psi_{n+4} + \frac{5}{6}\Psi_{n+5})/(\frac{15}{4} + a^2 k_n^2). \tag{A.43}$$

A.7 Excited state wave function using WKB approximation

In order to patch a wave function through arbitrary potential landscapes one can use the WKB approximation. The approximation will be made during the derivation[21], but in essence the only thing that is important is the change of the amplitude of the wave function over space. That is to say that $A''/A \ll (\phi')^2$ and $A''/A \ll p^2/\hbar^2$. To start the approximation, first the time independent Schrodinger equation has to be rewritten in the following form

$$\frac{d^2\psi}{dx^2} = -\frac{p^2}{\hbar^2}\psi, \tag{A.44}$$

where p is the momentum and can either be real in the classical region ($E > V$) or imaginary in the forbidden regions ($E < V$). Now in general, the wave function has the form

$$\psi(x) = A(x)e^{i\phi(x)}, \tag{A.45}$$

in which both the amplitude $A(x)$ and the phase $\phi(x)$ real. Filling in this assumption back into the rewritten Schrodinger equation (A.44) gives the following equality

$$A'' + 2iA'\phi' + iA\phi'' - A(\phi')^2 = -\frac{p^2}{\hbar^2}A, \tag{A.46}$$

which can then be split into two equations; one for the real part as

$$A'' - A(\phi')^2 = -\frac{p^2}{\hbar^2}A, \quad \text{or} \quad A'' = A\left[(\phi')^2 - \frac{p^2}{\hbar^2}\right], \tag{A.47}$$

and one for the imaginary part as

$$2A'\phi' + A\phi'' = 0, \quad \text{or} \quad \left(A^2\phi'\right)' = 0. \tag{A.48}$$

Solving the equation with the real components cannot be done analytically and therefore the approximation $A''/A \ll (\phi')^2$ and $A''/A^2/\hbar^2$ has to be made. This generally holds for functions far away from turning point, where $E = V$, but breaks down close to the turning points. Continuing with the assumption and dropping the A'' term leaves us for an expression for the wave function amplitude as

$$A^2\phi' = C^2, \quad \text{or} \quad A = \frac{C}{\sqrt{|\phi'|}}, \tag{A.49}$$

where an integration constant is introduced, which has to be solved using boundary conditions. The equation for the imaginary part can be solved analytically as

$$\phi(x) = \pm\frac{1}{\hbar}\int p(x)dx \tag{A.50}$$

representing the phase. By plugging the amplitude (equation (A.49)) and the phase (equation (A.50)) back into the general solution (equation (A.45)), the final result for the WKB formalism is obtained as

$$\psi(x) \approx \frac{C}{\sqrt{p(x)}}e^{\pm\frac{1}{\hbar}\int p(x)dx}. \tag{A.51}$$

A.7.1 WKB near turning point

Since the physics around the turning point is rather important, it is necessary to connect the formulas from the classical region and the forbidden region. This can be done in a framework of an increasing potential slope over space with the turning point (E=V) located at the origin. The solutions to both sides of the turning point are given as[21]

$$
\psi(x) \approx
\begin{cases}
\frac{1}{\sqrt{p(x)}} \left[B e^{\frac{i}{\hbar} \int_x^0 p(x') dx'} + C e^{-\frac{i}{\hbar} \int_x^0 p(x') dx'} \right], & x < 0, \\
\frac{1}{\sqrt{|p(x)|}} D e^{-\frac{1}{\hbar} \int_0^x |p(x')| dx'}, & x > 0.
\end{cases}
\tag{A.52}
$$

Where the wave function in the classical region is represented by an incoming and a reflected wave with amplitudes of respectively B and C and the wave function in the forbidden region is given by an exponential decay as would have been expected. The absolute signs are now added to the WKB solution since $p(x)$ is imaginary.

For the region around the turning point the potential will be linearized, leading to new momenta in this so called patching region as

$$
p(x) \approx \sqrt{2m \left(E - E - V'(0)x \right)}.
\tag{A.53}
$$

The Schrodinger equation in this region is now

$$
-\frac{\hbar^2}{2m} \frac{d^2 \psi_p}{dx^2} + \left(E + V'(0)x \right) \psi_p = E \psi_p,
\tag{A.54}
$$

or

$$
\frac{d^2 \psi_p}{dx^2} = \alpha^3 x \psi_p,
\tag{A.55}
$$

where

$$
\alpha \equiv \left[\frac{2m}{\hbar^2} V'(0) \right]^{1/3}.
\tag{A.56}
$$

This constant α can be absorbed into the equation by defining

$$
z \equiv \alpha x,
\tag{A.57}
$$

such that

$$
\frac{d^2 \psi_p}{dz^2} = z \psi_p.
\tag{A.58}
$$

This is a well known differential equation used in physics which comes up in different fields. The solutions are given by the so called Airy functions and are related to the Bessel's functions order 1/3. The resulting wave function is linear combinations of these linearly independent solutions $Ai(z)$ and $Bi(z)$ as

$$
\psi_p(x) = a \mathrm{Ai}(\alpha x) + b \mathrm{Bi}(\alpha x),
\tag{A.59}
$$

since the second term blows up for high z and this should not be the case for the forbidden region, b can be set to zero and the solution for the patching region is found. One can now connect the formulas from A.52 with the connection formulas on both sides resulting in the formulas

$$
\psi(x) \approx
\begin{cases}
\frac{2D}{\sqrt{p(x)}} \sin\left[\frac{1}{\hbar} \int_x^{x_2} p(x') dx' + \frac{\pi}{4} \right], & x < x_2, \\
\frac{D}{\sqrt{|p(x)|}} \exp\left[-\frac{1}{\hbar} \int_{x_2}^x |p(x')| dx' \right], & x > x_2.
\end{cases}
\tag{A.60}
$$

For a upwards slope, and

$$
\psi(x) \approx
\begin{cases}
\frac{D'}{\sqrt{|p(x)|}} \exp\left[-\frac{1}{\hbar} \int_x^{x_1} |p(x')| dx' \right], & x < x_1, \\
\frac{2D'}{\sqrt{p(x)}} \sin\left[\frac{1}{\hbar} \int_{x_1}^x p(x') dx' + \frac{\pi}{4} \right], & x > x_1,
\end{cases}
\tag{A.61}
$$

for a downwards slope. The normalization constant D can be found by either normalization or by finding a boundary condition for scattering states.

A.8 Internal quantum states

In this section, we shift the focus from wave functions in position space to the internal states and properties of the atoms following the discussion in book [21]. For the derivations the system is assumed to be a two-level system where the ground state is notated as $|\Psi_g\rangle$ with corresponding coefficient c_g and the excited state is notated as $|\Psi_e\rangle$ with corresponding coefficient c_e. The states in this derivation, given with the bra-ket notation, can represent single atom states but can also represent channel states such as $|S + S\rangle$ and $|S + P\rangle$.

A.8.1 Rabi oscillations

Rabi oscillations are a cyclic phenomena in a two-level quantum system in the presence of an oscillatory driving field. To see how the dynamics of these quantum states change, let's consider two states $|\Psi_g\rangle$, and $|\Psi_e\rangle$, which are eigenstates of the unperturbed Hamiltonian $\hat{H}^0$.

$$\hat{H}^0 |\Psi_g\rangle = E_g |\Psi_g\rangle \quad and \quad \hat{H}^0 |\Psi_e\rangle = E_e |\Psi_e\rangle \tag{A.62}$$

Since the eigenstates are orthonormal, the total wave function can be expressed as a linear combination of the two states at $t = 0$ as

$$\Psi(0) = c_g\Psi_g + c_e\Psi_e \tag{A.63}$$

where the prefactors c_g and c_e must obey $|c_g|^2 + |c_e|^2 = 1$.
To this, a time dependent wiggling factor equal to $e^{iE_jt/\hbar}$ is added, which are the solutions to the time dependent part of the Schrödinger equation, where $j = a, b$. This would then give the time dependent wave function

$$\Psi(t) = c_g\Psi_g e^{-iE_gt/\hbar} + c_e\Psi_e e^{-iE_et/\hbar}. \tag{A.64}$$

Now the system will be perturbed with a time dependent Hamiltonian $H'(t)$ to simulate the influence of the laser light. Plugging the time dependent wave function (A.64) into the time dependent Schrodinger's equation,

$$\hat{H}\Psi = i\hbar\frac{\partial\Psi}{\partial t}, \quad \text{where} \quad \hat{H} = \hat{H}^0 + \hat{H}'(t) \tag{A.65}$$

yields

$$c_g(\hat{H}^0\Psi_g)e^{-iE_gt/\hbar} + c_e(\hat{H}^0\Psi_e)e^{-iE_et/\hbar} + c_g(\hat{H}'\Psi_g)e^{-iE_gt/\hbar} + c_e(\hat{H}'\Psi_e)e^{-iE_et/\hbar}$$
$$= i\hbar[\dot{c}_g\Psi_g e^{-iE_gt/\hbar} + \dot{c}_e\Psi_g e^{-iE_et/\hbar} + c_g\Psi_g(-\frac{iE_g}{\hbar})e^{-iE_gt/\hbar} + c_e\Psi_e(-\frac{iE_e}{\hbar})e^{-iE_et/\hbar}]$$

And since the first two terms on the left cancel the last two terms on the right, the remaining equation

$$c_g(\hat{H}'\Psi_g)e^{-iE_gt/\hbar} + c_e(\hat{H}'\Psi_e)e^{-iE_et/\hbar} = i\hbar(\dot{c}_g\Psi_g e^{-iE_gt/\hbar} + \dot{c}_e\Psi_g e^{-iE_et/\hbar}). \tag{A.66}$$

To further reduce the equation, a trick can be used to isolate $\dot{c}_g$ – Note that this is the ultimate goal, since this would give information on how the states evolve over time. To do this, the inner product with Ψ_g is taken on both sides. Exploiting the orthogonality between the states Ψ_g and Ψ_e gives

$$c_g H'_{aa}e^{-iE_gt/\hbar} + c_e H'_{ab}e^{-iE_et/\hbar} = i\hbar\dot{c}_g e^{-iE_gt/\hbar}, \tag{A.67}$$

where H'_{ij} is shorthand notation for $\langle\Psi_i| H' |\Psi_j\rangle$. Rewriting the equation above for $\dot{c}_g$ yields:

$$\dot{c}_g = -\frac{i}{\hbar}[c_g H'_{aa} + c_e H'_{ab}e^{-i(E_e-E_g)t/\hbar}], \tag{A.68}$$

and similarly for $\dot{c}_e$:

$$\dot{c}_e = \frac{i}{\hbar}[c_e H'_{bb} + c_g H'_{ba}e^{i(E_e-E_g)t/\hbar}]. \tag{A.69}$$

Or more conveniently, when $H'_{aa} = H'_{bb} = 0$, and the transition frequency is introduced, $\omega_0 = \frac{E_e - E_g}{\hbar}$, the rate equations for the wave function coefficients with a perturbed Hamiltonian become[21]

$$\dot{c}_g = -\frac{i}{\hbar} c_e H'_{ab} e^{-i\omega_0 t} \quad \text{and} \quad \dot{c}_e = -\frac{i}{\hbar} c_g H'_{ba} e^{-i\omega_0 t}. \tag{A.70}$$

These off diagonal matrix elements H'_{ab} and H'_{ba} can then be rewritten upon introducing the Rabi frequency Ω as

$$\hbar\Omega = eE_o \langle \Psi_e | x | \Psi_e \rangle. \tag{A.71}$$

On top of this, one can assume a sinusoidal time dependence

$$\hat{H}'(r,t) = V(r)\cos(\omega t), \tag{A.72}$$

which is perfectly reasonable, since the laser light also has a sinusoidal electric field component. Using this Rabi frequency and the sinusoidal perturbation, the rate equations for the coefficients can be rewritten as

$$i\dot{c}_g = \Omega \cos(\omega t) e^{-i\omega_0 t} c_e \tag{A.73}$$

$$i\dot{c}_e = \Omega \cos(\omega t) e^{+i\omega_0 t} c_g \tag{A.74}$$

To further simplify this, one can make use of the Euler formulas in order to rewrite the $\cos(\omega t)$ as

$$i\dot{c}_g = \frac{\Omega}{2} \left(e^{i(\omega - \omega_0)t} + e^{i(\omega + \omega_0)t} \right) c_e \tag{A.75}$$

$$i\dot{c}_e = \frac{\Omega}{2} \left(e^{-i(\omega - \omega_0)t} + e^{i(\omega + \omega_0)t} \right) c_g \tag{A.76}$$

Now, two oscillatory terms can be seen in both formulas: one which oscillates with a frequency $(\omega - \omega_0)$ and one which oscillates with a frequency $(\omega + \omega_0)$. To put things into perspective, one can assume that

$$|\omega - \omega_0| = |\delta| \ll \omega + \omega_0 \tag{A.77}$$

Since the Rabi oscillations oscillate at long time scales compared to $|\omega - \omega_0|^{-1}$, over which the fast oscillation $e^{i(\omega + \omega_0)t}$ simply cancels out, these terms can be neglected, leaving the rate equations as

$$i\dot{c}_g = \frac{\Omega}{2} e^{i\delta t} c_e \quad \text{and} \quad i\dot{c}_e = \frac{\Omega}{2} e^{-i\delta t} c_g \tag{A.78}$$

This last approximation is called the rotating wave approximation[24] and is frequently used in the Rabi oscillation framework.

In the computer model, one can simulate the rate equations for the coefficients $c_1(t)$ and $c_2(t)$ from equation (A.78) explicitly and is also done in both the simulation outline as in the result part of this thesis. This last equation is the most useful as these are rate equations, which can be iterated per time step.

A.8.2 Off-resonance solutions to the Rabi equations

In the previous subsection we talked about how the rate equations for the state coefficients can be used to iterate the solutions over the time steps. However, to be confident about the solutions and to get a better insight into the solutions it is better calculate them analytically and to explore different limits. To find the solutions, it is assumed to be off-resonance, since by filling in $\delta = 0$ automatically the on-resonance case is obtained. The set of first order equations in equation (A.78) can be combined in a second order differential equation for c_1 as

$$\frac{d^2 c_g}{dt^2} - i\delta \frac{dc_g}{dt} + \frac{\Omega^2}{4} c_g = 0$$

$$\left(\frac{d}{dt} - \frac{i\delta}{2} + \frac{i\sqrt{\Omega^2 + \delta^2}}{2} \right) \left(\frac{d}{dt} - \frac{i\delta}{2} - \frac{i\sqrt{\Omega^2 + \delta^2}}{2} \right) c_g = 0,$$

which has the solutions

$$c_g(t) = e^{i\delta t/2} \left[A \cos \left(\frac{\sqrt{\Omega^2 + \delta^2}}{2} t \right) + B \sin \left(\frac{\sqrt{\Omega^2 + \delta^2}}{2} t \right) \right]. \tag{A.79}$$

Let assume, without loss of generality, that the atoms start in the ground state $|\Psi_g\rangle$ at $t = 0$. This implies that $A = 0$. To determine B, equation (A.78) will be used with the constraint that $c_e(t = 0) = 0$. This gives $B = -\frac{i\delta}{\sqrt{\Omega^2 + \delta^2}}$ and the solution for c_g reads

$$c_g = e^{i\delta t/2} \left[\cos \left(\frac{\sqrt{\Omega^2 + \delta^2}}{2} t \right) - \frac{i\delta}{\sqrt{\Omega^2 + \delta^2}} \sin \left(\frac{\sqrt{\Omega^2 + \delta^2}}{2} t \right) \right] \tag{A.80}$$

and for c_e,

$$c_e = -i e^{-i\delta t/2} \frac{\Omega}{\sqrt{\Omega^2 + \delta^2}} \sin \left(\frac{\sqrt{\Omega^2 + \delta^2}}{2} t \right). \tag{A.81}$$

Since the transition probability of exciting an atom to the excited state is equal to $|c_e(t)|^2$, this can then be calculated to be

$$P_e(t) = |c_e(t)|^2 = \frac{\Omega^2}{\Omega^2 + \delta^2} \sin^2 \left(\frac{\sqrt{\Omega^2 + \delta^2}}{2} t \right) \tag{A.82}$$

Where it is interesting to see how the frequency of the population cycles increases as soon as $\delta \neq 0$. This new frequency $\sqrt{\Omega^2 + \delta^2}$ is called the generalised Rabi frequency Ω'. Also, the amplitude of the oscillation will not reach 1 as soon as $\delta \neq 0$ but will be equal to $\frac{\Omega^2}{\Omega^2 + \delta^2}$. For lower electric fields, the detuning is much higher than the Rabi frequency, $\delta \gg \Omega$, and the probability P_e becomes

$$P_e(t) \approx \frac{\Omega^2}{\delta^2} \sin^2 \left(\frac{\delta t}{2} \right). \tag{A.83}$$

If the laser is resonant, of course, the detuning can be set to 0 and an easier formula for P_2 can be obtained,

$$P_e(t) = \sin^2 \left(\frac{\Omega}{2} t \right), \tag{A.84}$$

where the population simply oscillates between the ground state and the excited state[25].

A.8.3 Optical Bloch equations

The Rabi oscillations are a useful tool for calculating the absorption and stimulated emission effects, which in itself tell a lot about the atomic properties and the electronic dynamics between the atomic states. However, in the framework of the rate equation derived by Einstein, spontaneous emission has to take place, as is discussed in appendix A.9. This formalism, however, has its limitations as it does not include superposition states, whereas the Rabi oscillation formalism cannot explain spontaneous emission, since it is not caused by the coupling to the light field. Rather, spontaneous emission should, and can only be fully explained by the coupling to the vacuum fluctuation. Wigner and Weisskopf showed, later than Einstein did, that an atom in the excited state decays exponentially as a result of the fluctuations of the quantized vacuum field[26]. This principle has been applied to the same formalism as for the Rabi oscillations using the rate equations (A.68) and (A.69) and an energy density of

$$\vec{E}_\omega = \sqrt{\frac{\hbar \omega}{2\epsilon_0 V}} \hat{\varepsilon}. \tag{A.85}$$

The mathematical derivation will not be done again, but the final result can be summarized with the differential equation for the coefficient for the excited state as

$$\frac{\mathrm{d}c_e(t)}{\mathrm{d}t} = -\frac{\gamma}{2} c_e(t), \tag{A.86}$$

where

$$\gamma = \frac{\omega^3 \mu^2}{3\pi\epsilon_0 \hbar c^3}, \tag{A.87}$$

and where γ looks, as expected, almost familiar to the Einstein coefficient A, except for the term $|\langle\psi_1|\mathbf{x}|\psi_2\rangle|^2$ as can be seen in the appendix A.9.

The differential equation does indeed give the expected exponential decay when solving for $c_e(t)$. Nevertheless, it is far more interesting to know the rate equations and to implement this into the Rabi oscillation rate equations. To do this, first the density matrix formalism has to be introduced. The density matrix of any wave function can be expressed as

$$\rho = |\Psi\rangle\langle\Psi|, \tag{A.88}$$

where ρ in matrix formulation for a pure state looks like

$$\rho = \begin{pmatrix} \rho_{ee} & \rho_{eg} \\ \rho_{ge} & \rho_{gg} \end{pmatrix} = \begin{pmatrix} c_e c_e^* & c_e c_g^* \\ c_g c_e^* & c_g c_g^* \end{pmatrix}. \tag{A.89}$$

In order to get any insights into the dynamics of the density matrix, it can be substituted into the time dependent Schrodinger's equation, leading to

$$i\hbar \frac{\mathrm{d}\rho}{\mathrm{d}t} = [H, \rho] \tag{A.90}$$

Where H is the Hamiltonian of the system and the square brackets of the right hand side of the equation represent the commutator. Working out the dynamics for all four components of the density matrix using the Rabi Hamiltonian and including the spontaneous emission term, equation (A.86), the following rate equations can be obtained:

$$\begin{aligned}
\frac{\mathrm{d}\rho_{gg}}{\mathrm{d}t} &= +\gamma\rho_{ee} + \frac{i}{2}\left(\Omega^*\tilde{\rho}_{eg} - \Omega\tilde{\rho}_{ge}\right) \\
\frac{\mathrm{d}\rho_{ee}}{\mathrm{d}t} &= -\gamma\rho_{ee} + \frac{i}{2}\left(\Omega\tilde{\rho}_{ge} - \Omega^*\tilde{\rho}_{eg}\right) \\
\frac{\mathrm{d}\tilde{\rho}_{ge}}{\mathrm{d}t} &= -\left(\frac{\gamma}{2} + i\delta\right)\tilde{\rho}_{ge} + \frac{i}{2}\Omega^*\left(\rho_{ee} - \rho_{gg}\right) \\
\frac{\mathrm{d}\tilde{\rho}_{eg}}{\mathrm{d}t} &= -\left(\frac{\gamma}{2} - i\delta\right)\tilde{\rho}_{eg} + \frac{i}{2}\Omega\left(\rho_{gg} - \rho_{ee}\right),
\end{aligned} \tag{A.91}$$

where $\tilde{\rho}_{ge} \equiv \rho_{ge}e^{-i\delta t}$ and also $\mathrm{d}\rho_{ee}/\mathrm{d}t = -\mathrm{d}\rho_{gg}/\mathrm{d}t$, which is required in order to conserve the total population number, stated as $\rho_{gg} + \rho_{ee} = 1$. Also, γ is here defined as $1/\tau$, where τ is the lifetime of the excited state[26].

A.8.4 Solutions to the optical Bloch equations

In order to get some insights into the Optical Bloch Equations (OBEs) lets look at the steady-state solutions by setting all time derivatives to zero. Using the conservation of population, $\rho_{gg} + \rho_{ee} = 1$, and optical coherence, $\rho_{eg} = \rho_{ge}^*$, one can solve the OBE by defining the population difference as $w \equiv \rho_{gg} - \rho_{ee}$. This gives

$$\frac{\mathrm{d}\rho_{eg}}{\mathrm{d}t} = -\left(\frac{\gamma}{2} - i\delta\right)\rho_{eg} + \frac{iw\Omega}{2} = 0, \tag{A.92}$$

and

$$\frac{\mathrm{d}w}{\mathrm{d}t} = -\gamma w - i\left(\Omega\rho_{eg}^* - \Omega^*\rho_{eg}\right) + \gamma = 0. \tag{A.93}$$

These equation can then be solved for w and ρ_{eg} as

$$w = \frac{1}{1+s} \tag{A.94}$$

and

$$\rho_{eg} = \frac{i\Omega}{2(\gamma/2 - i\delta)(1+s)}. \tag{A.95}$$

Here, the saturation parameter is given by

$$s \equiv \frac{|\Omega|^2}{2|(\gamma/2 - i\delta)|^2} = \frac{|\Omega|^2/2}{\delta^2 + \gamma^2/4} \equiv \frac{s_0}{1 + (2\delta/\gamma)^2}, \tag{A.96}$$

where s_0 is the on resonance saturation parameter, δ is again the laser detuning and γ is the decay rate. s_0 is given by

$$s_0 \equiv 2|\Omega|^2/\gamma^2 = I/I_s, \tag{A.97}$$

with the saturation intensity I_s given by

$$I_s \equiv \frac{\pi hc}{3\lambda^3\tau}. \tag{A.98}$$

Here, two distinctions can be made to intuitively understand the saturation parameter. One where $s \ll 1$, causing $w \to 1$ (equation (A.94)) meaning the population is mostly in the ground state. The other regime is for high saturation, where $w \to 0$, meaning that the population is equally distributed between the ground and excited state. The excited state population can be calculated as a function of the saturation as

$$\rho_{ee} = \frac{1}{2}(1-w) = \frac{s}{2(1+s)} = \frac{s_0/2}{1 + s_0 + (2\delta/\gamma)^2}. \tag{A.99}$$

In the limit of this high saturation regime, the excited state population reaches $1/2$ meaning that the decay rate γ from the excited state to the ground state is equal to the excitation rate from the ground state to the excited state. This excitation rate can also be called the scattering rate γ_p, as it represents the effective scattering of the light from the laser field into the atom and is given by

$$\gamma_p = \gamma\rho_{ee} = \frac{s_0\gamma/2}{1 + s_0 + (2\delta/\gamma)^2}. \tag{A.100}$$

Again, taking the limit for high laser intensities, γ_p saturates to $\gamma/2$. This equation can be rewritten as

$$\gamma_p = \left(\frac{s_0}{1+s_0}\right)\left(\frac{\gamma/2}{1 + (2\delta/\gamma')^2}\right), \tag{A.101}$$

where

$$\gamma' = \gamma\sqrt{1+s_0} \tag{A.102}$$

is the power-broadened linewidth of the transition. In figure 2.3, the effects of power broadening can be seen as the on-resonance saturation parameter s_0 increases. The higher the intensity of the laser, the larger the range of detunings, which will effectively scatter the atom expressed in the scattering rate γ_p. For very high intensities, for example $s_0 = 100$, the scattering rate becomes $\gamma/2$ following equation (A.101)[26].

A.8.5 Dressed state model

Another important effect which has an influence on the spacing of the atom levels is the light shift, since it describes the differential Stark shift due to the trapping laser. From equation (A.70) one can replace the state coefficients c_g and c_e by

$$\begin{aligned} c'_g(t) &\equiv c_g(t) \\ c'_e(t) &\equiv c_e(t)e^{-i\delta t}, \end{aligned} \tag{A.103}$$

where an extra factor $e^{-i\delta t}$ is introduced, which can be done as it does not influence the probabilities of finding an atom in its ground or excited state. Adding this extra factor is called the rotating frame transformation which is exact and is a different approach than the rotating wave approximation done earlier. Filling equation (A.103) into equation (A.70) yields

$$
\begin{aligned}
i\hbar\frac{\mathrm{d}c'_g(t)}{\mathrm{d}t} &= c'_e(t)\frac{\hbar\Omega}{2} \\
i\hbar\frac{\mathrm{d}c'_e(t)}{\mathrm{d}t} &= c'_g(t)\frac{\hbar\Omega}{2} - c'_e(t)\hbar\delta.
\end{aligned}
\tag{A.104}
$$

These equations can then be put into the matrix formulation of the time dependent Schrodinger's equation, yielding the Hamiltonian matrix

$$
\mathcal{H} = \frac{\hbar}{2}\begin{bmatrix} -2\delta & \Omega \\ \Omega & 0 \end{bmatrix},
\tag{A.105}
$$

from which the eigenstates can be calculated. These eigenstates are the energy levels of the system given as

$$
E_{e,g} = \frac{\hbar}{2}\left(-\delta \mp \Omega'\right)
\tag{A.106}
$$

caused by the detuning. An important thing to note here is that the new energy spacing between the two dressed state levels are now simply Ω', which was the generalized Rabi frequency mentioned in section A.8.2[26]. This change in eigenstates will be important when calculating the resonance condition for the simulation as will be done in chapter 4.

A.8.6 Polarizability

Another effect which changes the states within the atom is the effect of the polarizability. For a full description of the polarizability, a quantum picture is needed, which relates the dynamic polarizability to the dipole matrix element $|\langle\phi_k|D|\phi_i\rangle|^2$, where i is the state for which the polarizability α_i is calculated and k are all the excited states the interaction has to be summed over. Doing this for a laser field frequency ω_L the equation is given as[47]

$$
\alpha_i\left(\omega_L\right) = 2e^2\sum_k\frac{\hbar\omega_{ik}\left|\langle\phi_k|D|\phi_i\rangle\right|^2}{\hbar^2\left(\omega_{ik}^2 - \omega_L^2\right)},
\tag{A.107}
$$

where ω_{ik} is the difference between the i and k states and e is the electronic charge constant. In order to not calculate the dipole matrix elements of all the interaction states, one can relate the transition rates A_{ik} to the dipole elements, written as

$$
A_{ik} = \frac{e^2}{4\pi\epsilon_0}\frac{4\omega_{ik}^3}{3\hbar c^3}\left|\langle\phi_k|D|\phi_i\rangle\right|^2
\tag{A.108}
$$

This formula can now be used to fill in for the dipole elements in equation (A.107), which yields

$$
\alpha_i\left(\omega_L\right) = 6\pi\epsilon_0 c^3\sum_k\frac{A_{ik}}{\omega_{ik}^2\left(\omega_{ik}^2 - \omega_L^2\right)}.
\tag{A.109}
$$

In literature, the transition rate is however not been calculated, but rather the excited state lifetime $1/A_T$ together with the branching ratio. For an excited state with quantum number S, L_k, J_k going to a lower energy state i with quantum numbers S, L_i, J_i, the branching ratio is given by

$$
\frac{\widetilde{A}_{ik}}{A_T} = \frac{(2J_i+1)\left\{\begin{matrix} J_i & J_k & 1 \\ L_k & L_i & S \end{matrix}\right\}^2}{\sum_{J=|L_i-S|}^{|L_i+S|}(2J+1)\left\{\begin{matrix} J & J_k \\ L_k & L_i \end{matrix}\right\}^2}\sum_{m_k=-J_k}^{J_k}(2J_k+1)\left(\begin{matrix} J_i & 1 & J_k \\ m_i & p & -m_k \end{matrix}\right)^2.
\tag{A.110}
$$

Here, the first term gives the coupling strength between the excited state and the lower state. For this, Racah 6-j symbols are used. The second term differentiates between the magnetic sublevels m_i of the ground state. This has to be done since different circular polarizations p of the light can be used. Summing over all the magnetic sublevels m_j of the excited state also uses the Wigner 3-j symbols, as can be seen in the formula[27].

One can now calculate the polarizability of the electronic level structure using the geometric scaling factors A_{ik}/A_T and the total transition rate A_T. And with this polarizability, the Stark shift ν can be calculated, as it scales with the polarizability as

$$h\Delta\nu = -\frac{1}{2}\alpha_i|\mathbf{E}|^2. \tag{A.111}$$

A.9 Rate equations

Here, the atoms will be treated as an ensemble of N atoms. These N atoms may either be in the ground state N_1 or in the excited state N_2. Since the total atom number stays constant, the equation $N_1 + N_2 = N$ must hold at all times.

When no laser light is on the excited state, atoms will spontaneous decay to the ground state with a decay rate of A_{21}. Since this decay rate is proportional to the amount of atoms in the excited state one can model the rate equation as[21]

$$\frac{dN_2}{dt} = -A_{21}N_2. \tag{A.112}$$

Solving this solution gives the exponential decay as a function of time given as

$$N_2(t) = N_2(0)e^{A_{21}t} = N_2(0)e^{-t/\tau} \quad \text{with} \quad \tau = \frac{1}{A_{21}}. \tag{A.113}$$

Now, the model needs to introduce a light field with an intensity density of $\rho(\omega)$. Since, by approximation, the laser light only excites atoms with a transition frequency ω_0, one can rewrite the intensity density as $\rho(\omega_0)$. The rate equation of the total system then becomes

$$\frac{dN_2}{dt} = \rho(\omega_0)(B_{12}N_1 - B_{21}N_2) - A_{21}N_2, \tag{A.114}$$

where the first term represents the light interaction and the second term the old spontaneous emission. Within the light interaction term two different terms arises, one which increases the excited state atoms N_2, which is called excitation, and one term which decreases the amount of atoms in the excited state N_2, which is called stimulated emission. Both these effects are proportional to B_{12} and B_{21} respectively. Suppose the atoms are in thermal equilibrium with the ambient field, this would imply that the rate equation is equal to zero and would give an expression for the density of the light $\rho(\omega_0)$ as

$$\rho(\omega_0) = \frac{A_{21}N_2}{B_{12}N_1 - B_{21}N_2} = \frac{A_{21}}{B_{12}\frac{N_1}{N_2} - B_{21}}. \tag{A.115}$$

Now, from thermodynamics, it is known that the number of particles in thermal equilibrium at temperature T, is proportional to the Boltzmann factor $(\exp(-E/k_BT))$ where E is energy of the particles. Using this fact, an expression for the ratio of the atoms numbers can be derived as

$$\frac{N_2}{N_1} = \frac{e^{-E_2/k_BT}}{e^{-E_1/k_BT}} = e^{-\hbar\omega_0/k_BT}. \tag{A.116}$$

Filling this back into equation (A.115) and comparing it to famous Planck's black-body formula gives the equality

$$\rho(\omega_0) = \frac{A_{21}}{B_{12}(g_1/g_2)e^{\hbar\omega_0/k_BT} - B_{21}} = \frac{\hbar}{\pi^2c^3}\frac{\omega_0^3}{e^{\hbar\omega_0/k_BT} - 1}. \tag{A.117}$$

From which one can conclude that

$$B_{12} = B_{21} \tag{A.118}$$

and that

$$A_{21} = \frac{\omega_0^3 \hbar}{\pi^2 c^3} B_{21}. \tag{A.119}$$

Since the B_{12} and B_{21} factors are equal, equation (A.118), this paper will from now on only use B to indicate one of them and A_{21} will be replaced with A. These A and B factors are called the Einstein coefficients.

When trying to calculate the Einstein coefficients, the equation for the excitation probability A.83 is needed in terms of the angular frequency as

$$P_2(t) = \frac{\Omega^2}{(\omega - \omega_0)^2} \sin^2 \left(\frac{(\omega - \omega_0) t}{2} \right). \tag{A.120}$$

For this derivation an electric field in the z direction as $\mathbf{E}_0 = (0, 0, \mathcal{E})$ is taken. The Rabi frequency from equation (A.83) is given by

$$\Omega^2 = \frac{e^2 \mathcal{E}^2}{\hbar^2} |\langle \psi_1 | z | \psi_2 \rangle|^2. \tag{A.121}$$

Filling in the Rabi frequency in equation (A.120) and recalling that the energy density $\rho(\omega)$ is stored in the electric field as $\epsilon_0 \mathcal{E}^2 / 2$ gives an integral over the frequencies as

$$P_2(t) = \frac{2e^2}{\epsilon_0 \hbar^2} |\langle \psi_1 | z | \psi_2 \rangle|^2 \int d\omega \frac{\rho(\omega)}{(\omega - \omega_0)^2} \sin^2 \left(\frac{(\omega - \omega_0) t}{2} \right). \tag{A.122}$$

Since the integral is highest near $\omega = \omega_0$, it is reasonable to replace the energy density $\rho(\omega)$ coming from the black-body formula with $\rho(\omega_0)$ and to take it outside the integral, which would lead to

$$P_2(t) \approx \frac{2e^2}{\epsilon_0 \hbar^2} \rho(\omega_0) |\langle \psi_1 | z | \psi_2 \rangle|^2 \int d\omega \frac{1}{(\omega - \omega_0)^2} \sin^2 \left(\frac{(\omega - \omega_0) t}{2} \right). \tag{A.123}$$

Now, it is simply a matter of mathematical precision to calculate the integral by introducing a variable $x = (\omega - \omega_0) t / 2$, extending the limits to $x = \pm \infty$ which would lead to

$$\begin{aligned} P_2(t) &\approx \frac{2e^2}{\epsilon_0 \hbar^2} \rho(\omega_0) |\langle \psi_1 | z | \psi_2 \rangle|^2 \frac{t}{2} \int_{-\infty}^{+\infty} dx \frac{\sin^2 x}{x^2} \\ &= \frac{e^2 \pi}{\epsilon_0 \hbar^2} \rho(\omega_0) |\langle \psi_1 | z | \psi_2 \rangle|^2 t. \end{aligned} \tag{A.124}$$

This equation grows linearly over time, which is wrong but is caused, by the approximations above. Nevertheless, it does give the right (constant) rate coefficient when calculating the rate $\dot{P}_2(t)$ by differentiating equation (A.124) over time. This gives

$$\text{Rate of Absorption} = \dot{P}_2(t) = \frac{e^2 \pi}{\epsilon_0 \hbar^2} \rho(\omega_0) |\langle \psi_1 | z | \psi_2 \rangle|^2 = B\rho(\omega_0), \tag{A.125}$$

which would give an Einstein coefficient B of

$$B = \frac{e^2 \pi}{\epsilon_0 \hbar^2} |\langle \psi_1 | z | \psi_2 \rangle|^2. \tag{A.126}$$

Since for this derivation only an electric field in the z-direction has been used, the coefficient is not rotationally invariant. To do this, one should introduce a normal vector $\hat{n}$ and integrate this

over the spherical circle, introducing a factor of $1/3$ in the Einstein coefficients. The final results would then be

$$B = \frac{e^2\pi}{3\epsilon_0\hbar^2}\left|\langle\psi_1|\mathbf{x}|\psi_2\rangle\right|^2.$$ (A.127)

For the Einstein coefficient A this would, according to equation (A.119), lead to [21]

$$A = \frac{e^2\omega_0^3}{3\pi\epsilon_0\hbar c^3}\left|\langle\psi_1|\mathbf{x}|\psi_2\rangle\right|^2.$$ (A.128)

Appendix B

Code

B.1 Rydberg calculator

```python
1  import arc
2  from arc import *                        #Import ARC (Alkali Rydberg Calculator)
3
4  #Laser Parameters
5  waist = 50.e-6 # 50 mu m
6  P = 20.e-6 # 2 mW
7
8  q=+1; #Light Polarisation (sigma+)
9  atom=Strontium88()
10 #print("%.2e s" % (atom.getStateLifetime(5,1,-1)) )
11 rabiFreq = atom.getRabiFrequency(5, 0, 0, 0, 5, 1, 1, q, P, waist, s = 0)
12 print("rabi Frequency = 2 pi x %.2f MHz" %(rabiFreq/(2*pi)*1e-6))
```

Listing B.1: Rydberg calculator for the Rabi strength between the S and P m_j

B.2 Rabi oscillations

```matlab
1  %——————————————————————————————————————————%
2  %—————————— Rabi flopping for a two level atom—————————————%
3  %——————————————————————————————————————————%
4
5  clc;
6  clear all;
7  close all;
8
9  %——————————————————————————————————————————%
10
11 N=1000000; % no of time grid points
12 t=linspace(0,22e-8,N); % time array in micro seconds
13 dt=t(2)-t(1); % step size in time
14
15 %——— initial conditions—————————
16 phi=0.3*pi %[0 2pi]
17 theta=0.9*pi; %[0 pi]
18 cg(1:N)=cos(theta/2); % initial ground state
19 ce(1:N)=exp(1i.*phi).*sin(theta./2); % initial excited state
20
21 Omega_rabi=54e6*2*pi; % Rabi frequency 2pi*54 Mhz
22
23 delta=[0 Omega_rabi 10*Omega_rabi]; % different detuning frequencies
24
25 for j=1:3 % loop for different detuning frequencies
26
27
28 for k=1:N-1 % finite difference loop for advancing in time
29
```

```
30      cg(k+1)=−(1i∗ce(k)∗Omega_rabi∗dt∗(exp(1i∗delta(j)∗t(k))/2))+cg(k);
31      ce(k+1)=−(1i∗cg(k)∗Omega_rabi∗dt∗(exp(−1i∗delta(j)∗t(k))/2))+ce(k);
32
33  end
34
35  Cg(j,:)=cg;
36  Ce(j,:)=ce;
37
38
39  end
40
41  % plotting the probabilities in ground and excited states
42
43  figure(1)
44
45  subplot(3,1,1)
46  plot(t,abs(Cg(1,:).∗Cg(1,:)),'linewidth',2)
47  hold on
48  plot(t,abs(Ce(1,:).∗Ce(1,:)),'r','linewidth',2)
49  axis([0 t(N) 0 1.1])
50  h=gca;
51  get(h,'FontSize')
52  set(h,'FontSize',14)
53  axis([0 t(N) 0 1.1])
54  fh = figure(1);
55  set(fh, 'color', 'white');
56
57  subplot(3,1,2)
58  plot(t,abs(Cg(2,:).∗Cg(2,:)),'linewidth',2)
59  hold on
60  plot(t,abs(Ce(2,:).∗Ce(2,:)),'r','linewidth',2)
61  ylabel('|cg^2| and |ce^2| probabilities','fontSize',14);
62  axis([0 t(N) 0 1.1])
63
64  subplot(3,1,3)
65  plot(t,abs(Cg(3,:).∗Cg(3,:)),'linewidth',2)
66  hold on
67  plot(t,abs(Ce(3,:).∗Ce(3,:)),'r','linewidth',2)
68  hold on
69  axis([0 t(N) 0 1.1])
70  xlabel('time','fontSize',14);
```

Listing B.2: Finite difference method applied for Rabi oscillations for Matlab.

B.3 Optical Bloch equations

```
1   %——————————————————————————————————————————%
2   %————Optical Bloch Equation for a two level atom——————————%
3   %——————————————————————————————————————————%
4
5   clc;
6   clear all;
7   close all;
8
9   %——————————————————————————————————————%
10
11  N=10000; % no of time grid points
12  t=linspace(0,22e−6,N); % time array in micro seconds
13  dt=t(2)−t(1); % step size in time
14
15  %——— initial conditions———————————
16
17  rho11(1:N)=0;
18  rho22(1:N)=1;
19  rho12(1:N)=0;
20  rho21(1:N)=0;
21
22  Omega_rabi=1e6∗2∗pi; % Rabi frequency 2pi∗10 Mhz
23
```

```matlab
24    delta=Omega_rabi; % Detuning frequency
25
26    gamma=1/(22e-6); % linewidth
27
28    %----Runge Kutta 4th order ----------------------------------------%
29
30    for i=2:N
31
32        k1 = drho22(t(i-1),rho12(i-1),rho21(i-1),rho22(i-1),gamma,Omega_rabi,delta)*dt;
33        l1 = drho11(t(i-1),rho12(i-1),rho21(i-1),rho22(i-1),gamma,Omega_rabi,delta)*dt;
34        m1 = drho12(t(i-1),rho11(i-1),rho12(i-1),rho22(i-1),gamma,Omega_rabi,delta)*dt;
35        n1 = drho21(t(i-1),rho11(i-1),rho12(i-1),rho22(i-1),gamma,Omega_rabi,delta)*dt;
36
37        k2 = drho22(t(i-1)+0.5*dt,rho12(i-1)+0.5*m1,rho21(i-1)+0.5*n1,rho22(i-1)+0.5*k1,gamma
            ,Omega_rabi,delta)*dt;
38        l2 = drho11(t(i-1)+0.5*dt,rho12(i-1)+0.5*m1,rho21(i-1)+0.5*n1,rho22(i-1)+0.5*k1,gamma
            ,Omega_rabi,delta)*dt;
39        m2 = drho12(t(i-1)+0.5*dt,rho11(i-1)+0.5*l1,rho12(i-1)+0.5*m1,rho22(i-1)+0.5*k1,gamma
            ,Omega_rabi,delta)*dt;
40        n2 = drho21(t(i-1)+0.5*dt,rho11(i-1)+0.5*l1,rho12(i-1)+0.5*m1,rho22(i-1)+0.5*k1,gamma
            ,Omega_rabi,delta)*dt;
41
42
43        k3 = drho22(t(i-1)+0.5*dt,rho12(i-1)+0.5*m2,rho21(i-1)+0.5*n2,rho22(i-1)+0.5*k2,gamma
            ,Omega_rabi,delta)*dt;
44        l3 = drho11(t(i-1)+0.5*dt,rho12(i-1)+0.5*m2,rho21(i-1)+0.5*n2,rho22(i-1)+0.5*k2,gamma
            ,Omega_rabi,delta)*dt;
45        m3 = drho12(t(i-1)+0.5*dt,rho11(i-1)+0.5*l2,rho12(i-1)+0.5*m2,rho22(i-1)+0.5*k2,gamma
            ,Omega_rabi,delta)*dt;
46        n3 = drho21(t(i-1)+0.5*dt,rho11(i-1)+0.5*l2,rho12(i-1)+0.5*m2,rho22(i-1)+0.5*k2,gamma
            ,Omega_rabi,delta)*dt;
47
48        k4 = drho22(t(i-1)+dt,rho12(i-1)+m3,rho21(i-1)+n3,rho22(i-1)+k3,gamma,Omega_rabi,
            delta)*dt;
49        l4 = drho11(t(i-1)+dt,rho12(i-1)+m3,rho21(i-1)+n3,rho22(i-1)+k3,gamma,Omega_rabi,
            delta)*dt;
50        m4 = drho12(t(i-1)+dt,rho11(i-1)+l3,rho12(i-1)+m3,rho22(i-1)+k3,gamma,Omega_rabi,
            delta)*dt;
51        n4 = drho21(t(i-1)+dt,rho11(i-1)+l3,rho12(i-1)+m3,rho22(i-1)+k3,gamma,Omega_rabi,
            delta)*dt;
52
53
54        rho22(i) = rho22(i-1)+((k1+2*(k2+k3)+k4)/6);
55        rho11(i) = rho11(i-1)+((l1+2*(l2+l3)+l4)/6);
56        rho12(i) = rho12(i-1)+((m1+2*(m2+m3)+m4)/6);
57        rho21(i) = rho21(i-1)+((n1+2*(n2+n3)+n4)/6);
58
59
60    end
61
62    %----------plotting solutions------------------------------------
63
64    figure(1)
65
66    plot(t,rho22,'linewidth',2)
67    hold on
68    plot(t,rho11,'k','linewidth',2)
69    % plot(t,abs(rho12),'r','linewidth',2)
70    % plot(t,abs(rho21),'g','linewidth',2)
71    xlabel('time','fontSize',14);
72    ylabel('density matrix elements','fontsize',14)
73    axis([0 t(N) 0 1.1])
74    h=gca;
75    get(h,'FontSize')
76    set(h,'FontSize',14)
77    axis([0 t(N) 0 1.1])
78    fh = figure(1);
79    set(fh, 'color', 'white');
80
81    %--------------------------end----------------------------------%
```

Listing B.3: Runge-Kutta method applied to solve the optical Bloch equations for Matlab.

B.4   Rejection Boltzmann method

```matlab
1   clc;
2   clear all;
3   close all;
4
5   SAVE_VELOCITIES = 1;
6
7   % Constants
8   m88sr = 1.46127*10^(-25);
9   kb = 1.38065*10^(-23);
10  T = 1*10^(-6);
11
12  % Probability Distribution
13  f = @(v) 4*pi*(m88sr/(2*pi*kb*T))^(3/2).*v.^2.*exp(-m88sr.*v.^2./(2.*kb.*T));
14
15  % Probability Distribution Range (random velocity between a and b)
16  a = 0;
17  b = 0.05;
18
19  % ymax is maximum value of f(v) between a and b
20  ymax = max(f(linspace(a,b,1e6)));
21
22  % save accepted v values
23  vsaved=[];
24  n = 0;
25  N = 10000; % amount of values before termination
26
27  while n < N
28
29      v=rand()*(b-a) + a;       % random velocity between a and b
30      y=rand()*ymax;            % random y coordinate between 0 and ymax
31
32      % if y is below f(v), then accept
33      if y <= f(v)
34          vsaved = [vsaved; v];
35          n = n+1;
36
37          if mod(n, round(N*0.1)) == 0
38              disp([num2str(round(n/N*100)) '%']);
39          end
40      end
41
42  end
43
44  % Normalization constant for probability density function
45  f_area = integral(f, 0, inf);
46
47  figure;
48  hold on;
49  histogram(vsaved, 100, 'Normalization', 'pdf');
50  xax = linspace(a, b, 1000);
51  plot(xax, f(xax)/f_area, 'k', 'LineWidth', 2);
52
53  if SAVE_VELOCITIES == 1
54      save('random_velocities.dat', 'vsaved', '-ascii');
55  end
```

Listing B.4: Rejection method applied on the Maxwell-Boltzmann velocity distribution function for Matlab.

B.5   Matlab2016 simulation

```matlab
1   clc;
2   clear;
3   close all;
4
5   Delta=0*10^6;                    % Hz
```

```matlab
6   rabi=10e3;
7
8   %% Nature constants
9   m88sr=1.46127*10^(-25);          % kg
10  rm88sr=m88sr^2/(2*m88sr);        % kg
11  molarm88sr=0.08790561225;        % kg/mol
12  hPlank=6.62607*10^(-34);         % J/Hz
13  hbar=1.05457*10^(-34);           % J*s
14  mp=1.67262*10^(-27);             % kg
15  me=9.10938*10^(-31);             % kg
16  a0=5.29177*10^(-11);             % m
17  EHa=4.35974*10^(-18);            % J
18  cspeed=3*10^8;                   % m/s
19  kb=1.38065*10^(-23);             % J/K
20
21  %% Constants
22  T=1*10^(-6);                                      % K
23  BroglieWavelength=(2*pi*hbar/(m88sr*kb*T))^(1/2); % m
24  N=1;
25
26  lambda0=689*10^-9;                               % m
27  omega0=2*pi*cspeed/lambda0;                      % Hz
28
29  lifetime=21.5*10^(-6);                           % s
30  Gamma=1/lifetime;                                % Hz
31  rayleigh=pi*omega0^2/lambda0;                    % m
32
33  linewidth = 7.6e3;                               % Hz
34
35
36
37  s02 = 2*rabi^2/linewidth^2;
38  Isat = pi*hPlank*cspeed/(3*lambda0^3*lifetime);
39  Intensity = Isat*2*rabi^2/linewidth^2;
40  s0 = Intensity/Isat;
41
42  rabi = s0*Gamma/2/(1+s0+(2*Delta/Gamma)^2);
43  rabi2 = sqrt(s0*Gamma^2/2);
44  %% Simulation Constants
45  h=1e-11;
46  %tEnd=0.00003;
47  tEnd=22*10^(-6)*1000; %0.000022
48  dt=0.25*1e-7;
49  softening=0;
50  t=0;
51  rng(1);
52  poscheck=ones(N,1);
53  plotRealTime = 1;
54  Nt=ceil(tEnd/dt);
55
56  %% FORT/dipole
57  r = @(x,y) sqrt(x.^2 + y.^2);            % m
58  w = @(z) omega0 * sqrt(1+z/rayleigh);
59  I = @(r,z) 2*power./(pi*w(z)).*exp(-2*r.^2./w(z).^2);
60  %U = @(r,z) -3*pi*c^2/(2*omega0.^3)*(Gamma/Delta).*I(r,z);
61
62  w0 = 0.86e-6;
63  power = 49/36*1.7*1e-3;
64  eta = 376.7;
65  conversion = 1.64878e-41;
66  g = 9.81;
67  amu = 1.66e-27;
68  lam_light=813e-9;               % m
69  evolution = @(z) 1+((lam_light.*z)./(pi*w0^2)).^2;
70  I_gaussian= @(r) 2*power/(pi*w0^2)*exp((-2.*r.^2)./(w0.^2));
71
72  pol_1S0 = 286;                  % 813nm
73  pol_3P1_mj1 = 353.9;            % 813nm
74
75
```

```matlab
76   pot_r_1S0 = @(r)  -0.5.*I_gaussian(r).*eta.*conversion.*pol_1S0; %J
77   pot_r_3P1 = @(r)  -0.5.*I_gaussian(r).*eta.*conversion.*pol_3P1_mj1;
78
79   pot_z_1S0 = @(z)  -0.5.*eta.*conversion.*pol_1S0.*(2.*power)./(pi.*evolution(z).*w0^2);
80   pot_z_3P1 = @(z)  -0.5.*eta.*conversion.*pol_3P1_mj1.*(2.*power)./(pi.*evolution(z).*w0
         ^2);%J
81
82   U1S0= @(r,z)  pot_r_1S0(r)+pot_z_1S0(z);
83   U3P1= @(r,z)  pot_r_3P1(r)+pot_z_3P1(z);
84
85   yr1=pot_r_1S0(linspace(0,1e-6,1000));
86   yz1=pot_z_1S0(linspace(0,10e-6,1000));
87
88   yr3=pot_r_3P1(linspace(0,1e-6,1000));
89   yz3=pot_z_3P1(linspace(0,10e-6,1000));
90
91   %plot(linspace(0,1e-6,1000), yr1/hbar*1e-6)
92   %plot(linspace(0,10e-6,1000),yz3/hbar*1e-6)
93
94   %Make velocities
95   v_random = load('random_velocities.dat');
96   phi=rand(N,1)*2*pi;
97   theta=rand(N,1)*pi;
98   vel=makevel(phi, theta, v_random, N);
99
100  %Define positions
101  pos = normrnd(0, .1e-6, N, 3);
102  x=pos(:,1);
103  y=pos(:,2);
104  z=pos(:,3);
105  r = sqrt(x.^2 + y.^2);
106
107  %Make state vector on Bloch sphere
108  i=2;
109  ce=zeros(N,Nt+1);
110  cg=zeros(N,Nt+1);
111  Pidecay=ones(N,Nt+1);
112  Number=N;
113
114  DP=0;
115  phi=rand(N,1)*2*pi;
          % [0 2pi]
116  theta=rand(N,1)*0.001;
             % [0 pi]
117  ce(:,1)=exp(1i.*phi).*sin(theta./2);
118  cg(:,1)=cos(theta/2);
119  [KE, PE, IE, T, Epar, ACstarkshift] = getEnergy(pos, vel, hPlank, m88sr, kb, Number,
         molarm88sr, EHa, a0, cg, ce, i, U1S0, U3P1);
120
121  %Calculate detuning
122  A=1/lifetime;
123
124  RelativeDelta=0;
125
126  timer=zeros(N,Nt+1);
127  timercheck=zeros(N,1);
128  statecheck=zeros(N,1);
129  timertime=zeros(N,1);
130  %Create color matrix for state vector
131  c=zeros(size(cg));
132  for i=1:size(cg,1)
133      c(i,:)=i;
134  end
135  i=2;
136
137  %Deleting particles out of screen
138  [acc, velokick, Pidecay, ce, cg] = getAcc(pos, softening, Number, a0, h, m88sr, EHa, cg,
         ce, i, U1S0, U3P1, Pidecay, DP);
139  particlenumber=ones(N,1);
140  for j=1:N
```

```matlab
141                if (sum(pos(j,:).^2,2))^(1/2)>1e-6
142                    particlenumber(j,:)=0;
143                end
144    end
145        pos(particlenumber==0,:)=[];
146        vel(particlenumber==0,:)=[];
147        acc(particlenumber==0,:)=[];
148        cg(particlenumber==0,:)=[];
149        ce(particlenumber==0,:)=[];
150        c(particlenumber==0,:)=[];
151        Pidecay(particlenumber==0,:)=[];
152        Number(1)=sum(particlenumber,1);
153        timer(particlenumber==0,:)=[];
154        timercheck(particlenumber==0)=[];
155        statecheck(particlenumber==0)=[];
156        timertime(particlenumber==0)=[];
157    %% save energies, particle orbits for plotting trails
158    pos_save = zeros(size(pos,1),3,Nt+1);
159    pos_save(:,:,1) = pos;
160    KE_save = zeros(Nt+1,1);
161    KE_save(1) = KE;
162    PE_save = zeros(Nt+1,1);
163    PE_save(1) = PE;
164    PE_plot = zeros(Nt+1,1);
165    PE_plot(1) = min(PE_save);
166    IE_save = zeros(Nt+1,1);
167    IE_save(1) = IE;
168    T_save=zeros(Nt+1,1);
169    T_save(1)=T;
170    Number_save=zeros(Nt+1,1);
171    Number_save(1)=Number;
172    t_all = (0:Nt)*dt;
173    Epar=0;
174    relative_delta=zeros(Nt+1,1);
175    relative_delta(1)=RelativeDelta;
176
177    ce_save=zeros(N,Nt+1,1);
178    ce_save(:,1)=ce(:,1);
179    %% Time integration sceme
180    for i=2:Nt
181        vel = vel+acc*dt/2;
182        pos = pos+vel*dt;
183        [acc velokick, Pidecay, ce, cg] = getAcc(pos, softening, Number, a0, h, m88sr, EHa,
           cg, ce, i, U1S0, U3P1, Pidecay, DP);
184        velocitykick = makevelokick(velokick, hbar, omega0, m88sr, cspeed);
185        vel = vel+acc*dt/2+velocitykick;
186        t = t+dt;
187
188
189        if mod(i,1000)==0
190            disp(['time: ' num2str(t)])
191            disp(['progress: ' num2str(i/Nt*100) '%'])
192        end
193        %Remove particles outside of screen
194        %z>10e-6m
195        %r>1e-6m
196        particlenumber=ones(size(pos,1),1);
197        for j=1:size(pos,1)
198            if (pos(j,1)^2+pos(j,2)^2)^(1/2)>1e-6
199                particlenumber(j,:)=0;
200            elseif pos(j,3)>10e-6
201                particlenumber(j,:)=0;
202            end
203        end
204        pos(particlenumber==0,:)=[];
205        vel(particlenumber==0,:)=[];
206        acc(particlenumber==0,:)=[];
207        cg(particlenumber==0,:)=[];
208        ce(particlenumber==0,:)=[];
209        c(particlenumber==0,:)=[];
```

```matlab
210        Pidecay(particlenumber==0,:)=[];
211        Number=sum(particlenumber,1);
212        timer(particlenumber==0,:)=[];
213        statecheck(particlenumber==0,:)=[];
214
215        velokick(particlenumber==0,:)=[];
216        Number_save(i)=Number;
217     % get energy of system
218        [KE, PE, IE, T, Epar, ACstarkshift] = getEnergy( pos, vel, hPlank, m88sr, kb, Number
            , molarm88sr, EHa, a0, cg, ce, i, U1S0, U3P1);
219
220     %Update the state of the particles
221        substeps=1e4;
222        cg(:,i)=cg(:,i-1);
223        ce(:,i)=ce(:,i-1);
224
225
226        RelativeDelta=Delta-Epar/hPlank+ACstarkshift;          % Interaction energy,
            StarkShift
227
228      for j=1:substeps
229        cg_temp = cg(:,i);
230        ce_temp = ce(:,i);
231        cg(:,i)=(-1i.*rabi./2.*exp(1i.*RelativeDelta.*t).*ce_temp.*dt/substeps+cg_temp);
232        t=t+dt/substeps;
233        ce(:,i)=((-1i.*rabi./2.*exp(-1i.*RelativeDelta.*t).*cg(:,i).*dt/substeps+ce_temp));
234      end
235
236        statecheck(statecheck==1)=0;
237        statecheck(real(Pidecay(:,i-1))<0.1)=1;
238        timer(:,i)=statecheck;
239        lasttimer=timer(:,max(i-100,1):i);
240        timecheck=all(lasttimer,2);
241        Pidecay(timecheck==1,max(i-2,1):i)=1;
242        velokick(timecheck==1)=1;
243        timer(timecheck==1,i)=0;
244
245        phi=rand()*2*pi;
            % [0 2pi]
246        theta=rand()*0.001;
            % [0 pi]
247        ce(timecheck==1,i-1)=exp(1i.*phi).*sin(theta./2);
248        cg(timecheck==1,i-1)=cos(theta/2);
249
250
251        Pidecay(:,i)=Pidecay(:,i-1)./(1+A.*dt.*conj(ce(:,i)).*ce(:,i));          %
            Updating the decay rate
252     DP=real(Pidecay(:,i-1)-Pidecay(:,i));                                       %
            Calculating the probability of decay in dt
253
254
255
256     % save energies, positions for plotting trail
257      if isempty(RelativeDelta)
258          relative_delta(i)=0;
259      else
260          relative_delta(i)=min(RelativeDelta);
261      end
262        pos_save(:,:,i) = pos;
263        KE_save(i) = KE;
264        PE_save(i) = PE;
265        PE_plot(1:i)=(PE_save(1:i)-min(PE_save(1:i)));
266        IE_save(i) = IE;
267        T_save(i) = T;
268
269 end
270
271 save(['100vTrapLossSimulation_rabi_' num2str(rabi*100/(10^6)) 'Hz_delta_' num2str(Delta
        /(10^6)) 'Hz_N_' num2str(N)]);
272
273 %% Acceleration Calculations
```

```matlab
274  function [a, velokick, Pidecay, ce, cg] = getAcc(pos, softening, Number, a0, h,m88sr,
         EHa, cg, ce,i, U1S0, U3P1, Pidecay, DP)
275  S=cg(:,i-1).*conj(cg(:,i-1));
276  P=ce(:,i-1).*conj(ce(:,i-1));
277  %Calculating interaction strength
278  SS=cg(:,i-1).*conj(cg(:,i-1))*(cg(:,i-1)'.*conj(cg(:,i-1))')-diag(diag(cg(:,i-1).*conj(
         cg(:,i-1))*(cg(:,i-1)'.*conj(cg(:,i-1))')));
279  SP1=cg(:,i-1).*conj(cg(:,i-1))*(ce(:,i-1)'.*conj(ce(:,i-1))')-diag(diag(cg(:,i-1).*conj(
         cg(:,i-1))*(ce(:,i-1)'.*conj(ce(:,i-1))')));
280  PS1=ce(:,i-1).*conj(ce(:,i-1))*(cg(:,i-1)'.*conj(cg(:,i-1))')-diag(diag(ce(:,i-1).*conj(
         ce(:,i-1))*(cg(:,i-1)'.*conj(cg(:,i-1))')));
281  SP=SP1+PS1;
282  PP=ce(:,i-1).*conj(ce(:,i-1))*(ce(:,i-1)'.*conj(ce(:,i-1))')-diag(diag(ce(:,i-1).*conj(
         ce(:,i-1))*(ce(:,i-1)'.*conj(ce(:,i-1))')));
283      x=pos(:,1);
284      y=pos(:,2);
285      z=pos(:,3);
286      r = @(x,y) sqrt(x.^2+y.^2);
287
288      dx=repmat(x',Number,1)-repmat(x,1,Number);
289      dy=repmat(y',Number,1)-repmat(y,1,Number);
290      dz=repmat(z',Number,1)-repmat(z,1,Number);
291
292      dr = sqrt(dx.^2+dy.^2+dz.^2+softening.^2);
293
294      %% Interaction
295
296  %    U0u= @(dr) -3513*EHa*a0^6./dr.^6-0.015*EHa*a0^3./dr.^3;
297  %    U1u= @(dr) -3773*EHa*a0^6./dr.^6+0.0075*EHa*a0^3./dr.^3;
298
299      U0u=-0.015*EHa*a0^3./dr.^3; %red/atrractive
300      U1u=0.0075*EHa*a0^3./dr.^3; %blue/repulsive
301
302      force_strength=-0.0225*EHa*a0^3;
303
304      inv_r5 = dr.^-5;
305      inv_r5(inv_r5 == Inf) = 0;
306      inv_r5(inv_r5<1)=0;
307
308      Fx_U1u=force_strength*(dx.*inv_r5).*SP;
309      Fy_U1u=force_strength*(dy.*inv_r5).*SP;
310      Fz_U1u=force_strength*(dz.*inv_r5).*SP;
311
312
313      Fr_1S0 = -(U1S0(r(x,y)+h,z) - U1S0(r(x,y),z)) / h;
314      Fz_1S0 = -(U1S0(r(x,y),z+h) - U1S0(r(x,y),z)) / h;
315
316      Fr_3P1 = -(U3P1(r(x,y)+h,z) - U3P1(r(x,y),z)) / h;
317      Fz_3P1 = -(U3P1(r(x,y),z+h) - U3P1(r(x,y),z)) / h;
318
319      Fr=Fr_1S0.*S+Fr_3P1.*P;
320      Fz=Fz_1S0.*S+Fz_3P1.*P;
321
322      a = [Fr.*x./r(x,y)+sum(Fx_U1u,2), Fr.*y./r(x,y)+sum(Fy_U1u,2), Fz+sum(Fz_U1u,2)] /
         m88sr;
323
324      velokick=zeros(size(cg,1),1);              % 0 velokick
325      random=rand(size(velokick,1),1);           % Random for rejection method
326      decay_check=random<DP;                     % Reject/accept decay chance
327      velokick(decay_check==1)=1;                % If accepted, raise velokick
328      Pidecay(decay_check==1, i-1)=1;            % Reset the decay rate to zero
329
330      phi=rand()*2*pi;
         % [0 2pi]
331      theta=rand()*0.001;
         % [0 pi]
332      ce(decay_check==1,i-1)=exp(1i.*phi).*sin(theta./2);
333      cg(decay_check==1,i-1)=cos(theta/2);
334
335  end
336
```

```matlab
337  %% Calculate Energy
338  function [KE, PE, IE, T, Epar, ACstarkshift] = getEnergy(pos, vel, hPlank, m88sr, kb,
         Number, molarm88sr, EHa, a0, cg, ce, i, U1S0, U3P1)
339
340  S=cg(:,i-1).*conj(cg(:,i-1));
341  P=ce(:,i-1).*conj(ce(:,i-1));
342
343  %Calculating interaction strength
344  SP1=cg(:,i-1).*conj(cg(:,i-1))*(ce(:,i-1)'.*conj(ce(:,i-1))')-diag(diag(cg(:,i-1).*conj(
         cg(:,i-1))*(ce(:,i-1)'.*conj(ce(:,i-1))')));
345  PS1=ce(:,i-1).*conj(ce(:,i-1))*(cg(:,i-1)'.*conj(cg(:,i-1))')-diag(diag(ce(:,i-1).*conj(
         ce(:,i-1))*(cg(:,i-1)'.*conj(cg(:,i-1))')));
346  SP=SP1+PS1;
347
348  % Kinetic Energy:
349  KE = 0.5 * m88sr .* sum(sum((vel).^2 )) / kb; % [K]
350
351  %Temperature
352  R=8.3144598;
353  T=(sqrt(sum(sum(vel.^2,2))/Number)^2)*molarm88sr/(3*R);
354
355  % positions r = [x,y,z] for all particles
356  x = pos(:,1);
357  y = pos(:,2);
358  z = pos(:,3);
359
360  % matrix that stores all pairwise particle separations: r_j - r_i
361  dx=repmat(x',Number,1)-repmat(x,1,Number);
362  dy=repmat(y',Number,1)-repmat(y,1,Number);
363  dz=repmat(z',Number,1)-repmat(z,1,Number);
364
365  drr = (dx.^2+dy.^2+dz.^2).^(1/2);
366  drr(drr==0)=inf;
367  drr(drr>1)=inf;
368  % U0u= -3513*EHa*a0^6./drr.^6-0.015*EHa*a0^3./drr.^3;
369  % U1u= -3773*EHa*a0^6./drr.^6+0.0075*EHa*a0^3./drr.^3;
370
371  U0u= -0.015*EHa*a0^3./drr.^3;
372  U1u= 0.0075*EHa*a0^3./drr.^3.*SP;
373  % matrix that stores r for all particle pairwise particle separations
374  r = sqrt(x.^2 + y.^2);
375
376
377  PE=sum(U1S0(r,z))/kb+sum(sum(U1u))/(2*kb);   %[K]
378  IE = sum(sum(U1u.*SP))/(2*kb);   %[K]
379
380  %Being in the Pstate-Being in the Sstate
381  ACstarkshift = (U1S0(r,z)-U3P1(r,z))/hPlank;          %rad/s
382
383  Epar= sum(U1u,2);
384  end
385
386  function vel=makevel(phi, theta, v_random, N)
387  strength=v_random(round(rand(N,1).*size(v_random,1)));
388      vel=[strength.*sin(theta).*cos(phi), strength.*sin(theta).*sin(phi), strength.*cos(
         theta)];
389  end
390
391  function velocitykick = makevelokick(velokick, hbar, omega0, m88sr, cspeed)
392  phi=rand()*2*pi;
393  theta=rand()*pi;
394  random=rand(length(velokick),1);                        % Make a random vector of length
         velokick
395  energyconservation=zeros(length(velokick),1);           % Make a vector checking if it
         should release energy
396  energyconservation(random<velokick)=1;                  % Check the chance of releasing
         energy, if 1, then energy should be released
397  velokick(energyconservation==1)=1;                      % Make the energy gain equal to
         hbar*omega0
398  velokick(energyconservation==0)=0;                      % Create no velokick while still
         emitting a photon
```

```
399  strength=hbar.*omega0./cspeed.*velokick./m88sr;
400  velocitykick = [strength.*sin(theta).*cos(phi), strength.*sin(theta).*sin(phi), strength
        .*cos(theta)]; %v=2/m*sqrt(Egain)
401  end
```

Listing B.5: Light assisted collisions in FORT simulation for Matlab.

B.6 Plotting of the Matlab2016 simulation

```
1   corrE=0.000000000001;
2   particleloss=ones(Nt+1,1)*10;
3   corrE_save=zeros(Nt+1,1);
4   corrE_save(1)=corrE;
5   for i=2:Nt
6       if Number_save(i)-Number_save(i-1)<0
7           particleloss(i,1)=min(1e3*PE_plot);
8           corrE=corrE-(PE_save(i)-PE_save(i-1));
9
10      end
11      corrE_save(i) = corrE;
12  end
13
14  figure
15
16
17  subplot(3,1,1)
18
19  plot(t_all,1e3*KE_save,'LineWidth',1,'Color','blue')
20  hold on
21  plot(t_all,1e3*(PE_save-min(PE_save)+corrE_save),'LineWidth',1,'Color','green')
22  plot(t_all,1e3*(KE_save+PE_plot+corrE_save),'LineWidth',1,'Color','black')
23  plot(t_all,particleloss,'LineWidth',1,'Color','red')
24  legend('Kinetic energy','Potential energy','Total energy','Particle loss')
25  title('Energies')
26  xlim([0, tEnd]);
27  ylim([min(1e3*PE_plot) max(1e3*(KE_save+PE_plot+corrE_save))]);
28  xlabel('Time [s]');
29  ylabel('Energy [mK]');
30  drawnow
31
32  %        subplot(5,1,4)                                                      %
           Temperatur
33  %        plot(t_all,T_save,'r.')
34  %        xlim([0, tEnd]);
35  %        %ylim([1e-6, 10e-6]);
36  %        xlabel('Time');
37  %        ylabel('Temperatuur [K]');
38  %        drawnow
39
40           subplot(3,1,2)
41           hold on
42           t_all_ = repmat(t_all,size(ce,1),1);
43           t_all_ = t_all_(:);
44           ce_data = ce(:).*conj(ce(:));
45           scatter(t_all_,ce_data,1,c(:),'.')
46           title('Internal state')
47           xlim([0, tEnd]);
48           xlabel('Time[s]');
49           ylabel('ce');
50           hold off
51           drawnow
52
53           subplot(3,1,3)
54           hold on
55           t_all__ = repmat(t_all,size(Pidecay,1),1);
56           t_all__ = t_all_(:);
57           Pidecay_data = Pidecay(:).*conj(Pidecay(:));
58           scatter(t_all__,Pidecay_data,1,c(:),'.');
59           title('Decay curve')
```

```matlab
60                  xlim([0, tEnd]);
61                  hold on
62                  xlabel('Time[s]');
63                  ylabel('Pdecay');
64                  hold off
65
66  %               subplot(4,1,4)
67  %               plot(t_all,relative_delta/(10^6),'g.')
68  %               hold on
69  %               plot(t_all,rabi*ones(Nt+1,1)/(10^6),'b.')
70  %               plot(t_all,Delta*ones(Nt+1,1)/(10^6),'r.')
71  %               title('Relative delta')
72  %               legend('Relative delta','rabi','delta')
73  %               xlim([0, tEnd]);
74  %               ylim([0 max(relative_delta)/(10^6)]);
75  %               xlabel('Time [s]');
76  %               ylabel('detuing [MHz]');
77  %               drawnow
78  filename=['Plot_rabi' num2str(rabi*1000/(10^6)) 'kHz_delta' num2str(Delta/(10^6)) 'MHz_N
        ' num2str(N) '.png'];
79  sgtitle(['Rabi= ' num2str(rabi/(10^6)) 'MHz Delta= ' num2str(Delta/(10^6)) 'MHz N='
        num2str(N)])
80  set(gcf, 'Units', 'Normalized', 'OuterPosition', [0 0 1 1]);
81  saveas(gcf,filename);
82
83
84  % figure
85  %
86  % for i=2:Nt
87  %     if mod(i,100)==0
88  %         xx = pos_save(:,1,max(i-50,1):i);
89  %         yy = pos_save(:,2,max(i-50,1):i);
90  %         zz = pos_save(:,3,max(i-50,1):i);
91  %         scatter3(xx(:),yy(:),zz(:),5,[.7 .7 1],'.');
92  %         hold on
93  %         scatter3( xx(:,1), yy(:,2), zz(:,3), 150, [abs(ce(:,i).^2), zeros(size(pos,1)
        ,1), zeros(size(pos,1),1)], '.')
94  %         %ce=0 represents black
95  %         title(['progress: ' num2str(i/Nt*100) '%'])
96  %         hold off
97  %         axis square
98  %         axis([-1e-6 1e-6 -1e-6 1e-6 -10e-6 10e-6])
99  %         xlabel('x [m]')
100 %         ylabel('y [m]')
101 %         zlabel('z [m]')
102 %         drawnow
103 %     end
104 % end
105
106 %         subplot(4,1,3)
107 %         plot(t_all,1e3*KE_save,'b.')
108 %         hold on
109 %         plot(t_all,1e3*(PE_save+abs(min(PE_save))),'g.')
110 %         plot(t_all,1e3*(KE_save+PE_save+abs(min(PE_save))),'k.')
111 %         hold off
112 %         xlim([0, tEnd]);
113 %         ylim([0 max(1e3*(KE_save+PE_save+PE_plot))]);
114 %         xlabel('Time');
115 %         ylabel('Energy [mK]');
116 %         drawnow
117 %
118
119 %         subplot(5,1,5)
120 %         hold on
121 %         plot(t_all,relative_delta)
122 %         xlim([0, tEnd]);
123 %         xlabel('Time');
124 %         ylabel('min relative delta (expected ');
125 %         hold off
126 %         drawnow
```

```matlab
127  %          subplot(6,1,6);
128  %          scatter(t_all,Number,1);
129  %          xlabel('Time');
130  %          ylabel('Particle Count');
131  %          hold off
132  disp(['begin energy:' num2str(1e3*(KE_save(2)+PE_plot(2)+corrE_save(2))) 'mK'])
133  disp(['average energy:' num2str(1e3*sum(KE_save+PE_plot+corrE_save)./length(KE_save)) '
         mK']);
134  disp(['maximum energy:' num2str(1e3*max((KE_save+PE_plot+corrE_save))) 'mK']);
135  disp(['deviation:' num2str(1e6*(KE_save(2)+PE_plot(2)+corrE_save(2))-1e6*max((KE_save+
         PE_plot+corrE_save))) 'microK'])
136  clear
```

Listing B.6: Plotting of the light assisted collisions in FORT simulation for Matlab.

B.7 Quantum calculation on Mathematica

```mathematica
1   ClearAll["Global'*"]
2   Q = Quantity; UC = UnitConvert; QM = QuantityMagnitude;
3   cstValues =
4     N[QM[UC[Q[#]]]] & /@ {"PlanckConstant", "ReducedPlanckConstant",
5       "ProtonMass", "ElectronMass", "BohrRadius", "HartreeEnergy",
6       "BoltzmannConstant"};
7   cstSymbols = {hPlanck, \[HBar], mp, me, a0, EHa, kB};
8   cst = MapThread[Rule, {cstSymbols, cstValues}]
9   parms = {\[Lambda] -> 689. 10^-9, \[Tau] -> 21.5 10^-6, \[Mu]Sr88au ->
10      1.46127*10^-25}
11  (*T=1-5*10^-3K*)
12  tau = 21.35*10^-6
13  hbar = 1.0545718*10^-34;
14  c = 8*10^8;
15  \[Lambda] = 689*10^-9
16  C30au = -0.01524*EHa*a0^3;
17  C31au = 0.00753*EHa*a0^3;
18  C60au = 3513*EHa*a0^6;
19  C61au = 3774*EHa*a0^6;
20  V0u[R_] := -C60au/R^6 + C30au/R^3;
21  V1u[R_] := -C61au/(R)^6 + C31au/(R)^3;
22  DV0u[R_] = D[V0u[R], R];
23  DV1u[R_] = D[V1u[R], R];
24  V0u[R]/hPlanck*10^-6 /. cst
25  Plot[{V0u[R]/hPlanck*10^-6 /. R -> x*a0 /. cst,
26    V1u[R]/hPlanck*10^-6 /. R -> x*a0 /. cst}, {x, 0, 600},
27   PlotRange -> {-30, 30},
28   PlotLabel ->
29    "\!\(\*SubscriptBox[\(0\), \(u\)]\) and \!\(\*SubscriptBox[\(1\), \
30  \(u\)]\) potentials for S+P", AxesLabel -> {"R [a0]", "V [MHz]"},
31   PlotLegends -> {"0u potential", "1u potential"},
32   PlotStyle -> {Thickness[0.01]}]
33  Rc = R /. Solve[V1u[R]/hPlanck*10^-6 == 2, R, Reals][[2]] /. cst
34  Rc = Rc/a0 /. cst
35  Dc = D[V1u[R], R] /. cst /. R -> Rc
36  Series[Sqrt[1 + x^2], {x, 0, 3}]
37  ------------------------------------------------
38  ClearAll["Global'*"]
39  Q = Quantity; UC = UnitConvert; QM = QuantityMagnitude;
40  cstValues =
41    N[QM[UC[Q[#]]]] & /@ {"PlanckConstant", "ReducedPlanckConstant",
42      "ProtonMass", "ElectronMass", "BohrRadius", "HartreeEnergy",
43      "BoltzmannConstant"};
44  cstSymbols = {hPlanck, \[HBar], mp, me, a0, EHa, kB};
45  cst = MapThread[Rule, {cstSymbols, cstValues}];
46  parms = {\[Lambda] -> 689. 10^-9, \[Tau] -> 21.5 10^-6, \[Mu]Sr88au ->
47      1.46127*10^-25};
48  (*T=1-5*10^-3K*)
49  tau = 21.35*10^-6;
50  hbar = 1.0545718*10^-34;
51  c = 8*10^8;
52  \[Lambda] = 689*10^-9;
```

```
53
54  a = -2;
55  m = \[Mu]Sr88au/me/2 /. cst /.
56      parms; (*\[Mu]Sr88au=weight in kg of single atom*)
57  T = 1*10^-6; (*fixed temperature*)
58  Tlist = Table[i - 0.9, {i, 5}]*10^-6
59  r0 = 2000;
60  a0 = 5.29177*10^-11;
61
62  Elist = Tlist*kB/EHa /. cst /.
63      parms (*Energy spacing to recreate bose-Einstein distribution*)
64  Eg = First[Elist]; (*energy used for infite box width*)
65  spacing = Elist[[2]] - Elist[[1]];
66  Vground[r_] := -3103/r^6; (*Ground state potential*)
67  kground[r_, Eground_] := Sqrt[2 m*(Eground - Vground[r])]
68  \[Delta][Eground_] :=
69   ArcTan[-a*
70      kground[r0, Eground]] (*Phase shift as function of the energy*)
71
72  widthtrap = 1*^-6/a0/2 /. cst;
73  quantumnumber[Eground_] :=
74   Round[(kground[r0, Eground]*widthtrap + \[Delta][Eground])/Pi]
75  infiniteboxwidth[
76      Eground_] := (quantumnumber[Eground]*Pi - \[Delta][Eground])/
77   kground[r0, Eground]
78
79  uout[r_, Eground_] := Sin[kground[r0, Eground]*r + \[Delta][Eground]];
80  uin[r_, Eground_] :=
81    B*Sin[kground[r, Eground]*r] + A*Cos[kground[r, Eground]*r];
82
83  DUin[r_, Eground_] = D[uin[r, Eground], r];
84  DUout[r_, Eground_] = D[uout[r, Eground], r];
85  Uout[r_, Eground_] = uout[r, Eground];
86  Uin[r_, Eground_] = uin[r, Eground];
87
88  Bvalue[r_, Eground_] :=
89    B /. Solve[
90         DUin[r, Evar]/Uin[r, Evar] == DUout[r, Evar]/Uout[r, Evar], B][[
91        1]] /. Evar -> Eground;
92  Bvalue[r0, Elist];
93
94  uuin[r_, Eground_] := uin[r, Eground] /. B -> Bvalue[r0, Eground];
95  Uuin[r_, Eground_] = uuin[r, Eground];
96  Uuin[r0, Elist];
97
98  Avalue[r_, Eground_] :=
99    A /. Solve[Uuin[r, Evar] == Uout[r, Evar], A][[1]] /.
100      Evar -> Eground;
101  Avalue[r0, Elist];
102
103  uuuin[r_, Eground_] :=
104   uuin[r, Eground] /. A -> Avalue[r0, Eground] /.
105    B -> Bvalue[r0, Eground]
106  Uuuin[r_, Eground_] = uuuin[r, Eground];
107
108  Plot[{Uuuin[r, Elist], uout[r, Elist]}, {r, 0, infiniteboxwidth[Eg]},
109   PlotLegends -> {"Uin", "Uout"}]
110
111  SurfaceGround[Eground_] :=
112   Re[NIntegrate[Uuuin[r, Eground]^2, {r, 0, infiniteboxwidth[Eg]}]]
113
114  surface = Table[Re[SurfaceGround[Elist[[i]]]], {i, Length[Elist]}];
115
116
117  Table[NIntegrate[(1/
118       Sqrt[SurfaceGround[Elist[[i]]]] Uuuin[r, Elist[[i]]])^2, {r, 0,
119    infiniteboxwidth[Eg]}, {i,
120   Length[Elist]}] (*CHECK whether integral of normalized u^2 is equal \
121  to 1*)
122  PsiGround[r_, Eground_] :=
```

```mathematica
123   1/Sqrt[surface]*Uuuin[r, Eground]/(r*kground[r, Eground])
124   Plot[PsiGround[r, Elist], {r, 0, infiniteboxwidth[Eg]}]
125   ------------------------------------------------------------
126   matrix = {};
127   detuning = 10 (*till 2*(N-1) in MHz*)
128   For[i = 1, i < detuning, i++, AppendTo[matrix,
129       Vexited[r_] := 0.0075/r^3;
130       EExited[Eground_] := 2*i*10^6*hPlanck/EHa + Eground /. cst;
131       kexited[r_, Eground_] := Sqrt[2 m*(EExited[Eground] - Vexited[r])];
132       kExited = kexited[r, Elist];
133       Eexitedlist = EExited[Elist];
134       table =
135        Table[NDSolve[{y''[r] == -2*m*(Eexitedlist[[i]] - Vexited[r])*
136               y[r], y[1] == 0, y'[1] == 1/10^30},
137           y, {r, 0, infiniteboxwidth[Eg]}][[1]][[1]], {i,
138           Length[Elist]}];
139       Psiexited = Table[y[r] /. table[[i]], {i, Length[Elist]}];
140       SurfaceExited =
141        Table[NIntegrate[
142           Psiexited[[i]]^2, {r, 0, infiniteboxwidth[Eg]}], {i,
143           Length[Elist]}];
144       Table[NIntegrate[(1/Sqrt[SurfaceExited[[i]]] Psiexited[[i]])^2, {r,
145            0, infiniteboxwidth[Eg]}], {i, Length[Elist]}] ;(*check*)
146
147       PsiExited =
148        Table[(1/Sqrt[SurfaceExited[[i]]] Psiexited[[i]])/(r*
149             kExited[[i]]), {i, Length[Elist]}];
150       overlap =
151        Table[Conjugate[PsiGround[r, Eg + spacing*(i - 1)][[i]]]*
152           PsiExited[[i]], {i, Length[Elist]}];
153       FrankCondon =
154        Abs[Re[NIntegrate[overlap, {r, 0, infiniteboxwidth[Eg]}]]] // N
155       ]];
156   matrix
157   ------------------------------------------------------------
158   distribution[E_, \[Mu]_, T_] :=
159    1/(Exp[1/(kB*T) (E - \[Mu])] - 1) /. cst
160
161   xdata = Table[Eg + spacing*(i - 1), {i, Length[Elist]}];
162   particlenumber = 2;
163   groundstatematrix = {};
164   For[i = 1, i < detuning, i++, AppendTo[groundstatematrix,
165      distributionground =
166       distribution[Elist, Elist/particlenumber /. cst, T/EHa /. cst]
167      ]]
168   groundstatematrix;
169
170   traplossprofile = {};
171   For[i = 1, i < detuning, i++, AppendTo[traplossprofile,
172      1/(15)^3 (2*i - 15)^3 + 1
173      ]]
174   groundstatematrix*matrix;
175   traplossprofile;
176
177   traplossprofilesimulation = {0.004, 0.043, 0.029, 0.010,
178      0.012} ;(*energy gain as function of the detuning from 0 to 18MHz*)
179   \
180
181   xdatasimulation = {0, 5, 10, 15, 20};
182   datasimulation =
183     Partition[Riffle[xdatasimulation, traplossprofilesimulation], 2];
184   traplossprofilesimulationcurve = Interpolation[datasimulation];
185   deltavalues = Table[2*i, {i, detuning - 1}];
186   traplossprofilesimulationgood =
187     traplossprofilesimulationcurve[deltavalues];
188
189
190   Integralpieces =
191    groundstatematrix*matrix*
192     traplossprofile; (*replace "traplossprofilesimulationgood" for \
```

```
193  "traplossprofile" to get analytic plot *)
194
195  listspacing = Eg;
196  traploss = {};
197  For[i = 1, i < detuning, i++, AppendTo[traploss,
198    xdata = Table[Eg + spacing*(i - 1), {i, Length[Elist]}];
199    data = Partition[Riffle[xdata, Integralpieces[[i]]], 2];
200    xbegin = xdata[[1]];
201    xend = Last[xdata];
202    TrapLoss = Integrate[Interpolation[data][x], {x, xbegin, xend}]
203    ]]
204  traploss;
205  \[CapitalDelta] = Table[2*i, {i, detuning - 1}];
206  plot = Interpolation[Partition[Riffle[\[CapitalDelta], traploss], 2]];
207  maxtraploss = FindMaximum[plot[x], {x, 2, 18}]
208  line1 = 3
209  Plot[plot[x], {x, 0, 20},
210   PlotLabel -> "TrapLoss as function of the laser detuning",
211   AxesLabel -> {"\[CapitalDelta] [MHz]", "TrapLoss"},
212   PlotLegends -> {"Trap Loss Curve"} ]
```

Listing B.7: Quantum wavefunction